T.R.

GEBZE TECHNICAL UNIVERSITY

GRADUATE SCHOOL OF NATURAL AND APPLIED SCIENCES

SYNTHESIS OF NEW DYES AND THEIR METAL COMPLEXES

NURAY ESRA AKSAKAL

A THESIS SUBMITTED FOR THE DEGREE OF

DOCTOR OF PHILOSOPHY

DEPARTMENT OF CHEMISTRY

GEBZE

2020

T.R.

GEBZE TECHNICAL UNIVERSITY

GRADUATE SCHOOL OF NATURAL AND APPLIED SCIENCES

SYNTHESIS OF NEW DYES AND THEIR METAL COMPLEXES

NURAY ESRA AKSAKAL

A THESIS SUBMITTED FOR THE DEGREE OF

DOCTOR OF PHILOSOPHY

DEPARTMENT OF CHEMISTRY

THESIS SUPERVISOR

PROF. DR. FATMA YÜKSEL

GEBZE

2020

T.C.
GEBZE TEKNİK ÜNİVERSİTESİ
FEN BİLİMLERİ ENSTİTÜSÜ

YENİ BOYAR MADDELERİN VE METAL KOMPLEKSLERİNİN SENTEZİ

NURAY ESRA AKSAKAL

DOKTORA TEZİ
KİMYA ANABİLİM DALI

DANIŞMANI
PROF. DR. FATMA YÜKSEL

GEBZE
2020

GEBZE TEKNİK ÜNİVERSİTESİ	**DOKTORA JÜRİ ONAY FORMU**

GTÜ Fen Bilimleri Enstitüsü Yönetim Kurulu'nun 19/12/2019 tarih ve 2019/55 sayılı kararıyla oluşturulan jüri tarafından 07/01/2020 tarihinde tez savunma sınavı yapılan Nuray Esra AKSAKAL'ın tez çalışması Kimya Anabilim Dalında DOKTORA tezi olarak kabul edilmiştir.

JÜRİ

ÜYE (TEZ DANIŞMANI)	: Prof. Dr. Fatma YÜKSEL
ÜYE	: Prof. Dr. Devrim ATİLLA
ÜYE	: Prof. Dr. M. Kasım ŞENER
ÜYE	: Prof. Dr. Gönül YENİLMEZ ÇİFTÇİ
ÜYE	: Doç. Dr. Esra TANRIVERDİ EÇİK

ONAY

Gebze Teknik Üniversitesi Fen Bilimleri Enstitüsü Yönetim Kurulu'nun

……/……./…… tarih ve ……/……. sayılı kararı.

SUMMARY

Perylene and BODIPY dyes are popular molecules because of their excellent properties such as high photochemical stability, fluorescence quantum yields and tunable optical properties. In this thesis, the synthesis and discovery of ruthenium and iridium complexes of perylene and BODIPY units have been presented.

This thesis can be divided into three parts. In the first part of the study, a new perylene diimide derivative was combined with novel ruthenium(II) and iridium(III) phenanthroline complexes in order to investigate the photophysical and photochemical features for potential applications. During this step, new ruthenium and iridium metal complexes with 4,7-substitution that can be presented as the first example of phenanthroline ruthenium metal complex with bis(perylenediimide) in the literature were synthesized. After chemical characterizations with MALDI-TOF, FT-IR, ^{1}H and ^{13}C-NMR, UV-vis spectroscopies, photophysical and photochemical studies were performed. The photosensitiser behaviour of ruthenium(II) perylene *in vitro* was investigated with human chronic myeloid cells, K562.

In the second part, a new distryl BODIPY core was attached to the ruthenium(II) and iridium(III) compounds. These unique photosensitiser candidates have two BODIPY units in the structure which increases the singlet oxygen generation of the molecules twice. After the UV-vis absorption study in the red region, the ability of singlet oxygen generation of these complexes was calculated. *In vitro* PDT efficacy of the complexes with K562 and cervical cancer cell lines, HeLa, were studied under red light irradiation in the cell death process. These new ruthenium photosensitisers having perylene and BODIPY units are notable candidates to apply *in vitro* PDT.

In the last part, synthesis of a benzimidazole-fused perylene ruthenium(II) complex was accomplished. The molecule possesses enlarged π-conjugation over the molecule that makes it a promising candidate for studying in optoelectronic purposes.

Key Words: perylene, ruthenium(II), iridium(III), BODIPY, singlet oxygen, photodynamic therapy.

ÖZET

Perilen ve BODIPY boyaları, yüksek fotokimyasal kararlılık, floresans kuantum verimleri ve ayarlanabilir optik özellikleri gibi mükemmel özellikleri sayesinde popüler moleküllerdir. Bu tezde, perilen ve BODIPY bileşiklerinin rutenyum ve iridyum komplekslerinin sentezi sunulmuştur.

Bu tez üç bölümde incelenebilir. Çalışmanın birinci bölümünde, yeni rutenyum(II) ve iridyum(III) fenantrolin metal kompleksleri ile yeni bir perilen diimit türevi birleştirildi. Bu basamakta, literatürdeki ilk bis(perilendiimid) fenantrolin rutenyum metal kompleksi örneği olan 4,7-sübstitüe yeni rutenyum ve iridyum metal kompleksleri sentezlendi. Kimyasal yapı çözümlemeleri MALDI-TOF, FT-IR, ^{1}H ve ^{13}C-NMR ile yapıldıktan sonra fotofiziksel ve fotokimyasal çalışmaları gerçekleştirildi. Rutenyum(II) perilen bileşiğinin potansiyel fotosensitizer özellikleri insan kronik miyeloid hücreleri (K562) ile *in vitro* olarak incelendi.

İkinci bölümde, rutenyum(II) ve iridyum(III) bileşiklerine yeni bir distril BODIPY molekülü eklenmiştir. Bu değerli ışığa duyarlı molekül adayları, yapılarında moleküllerin singlet oksijen üretimini iki kez artıran iki BODIPY ünitesine sahiptir. Kırmızı bölgedeki UV-Vis absorpsiyon çalışmasından sonra, bu komplekslerin singlet oksijen üretme kapasiteleri hesaplandı. Komplekslerin kronik K562 ve rahim ağzı kanseri hücre hatları (HeLa) ile *in vitro* PDT çalışmaları yapıldı. Perilen ve BODIPY ünitelerine sahip olan bu yeni ışığa duyarlı rutenyum molekülleri karanlıkta, istenilen uzun doku penetrasyonu ve kısa inkübasyon süresi gibi özellikleri nedeni ile *in vivo* PDT'yi uygulamak için önemli adaylardır.

Tezin son bölümünde, benzimidazol ile kaynaşık yeni bir perilen Rutenyum (II) kompleksinin sentezi gerçekleştirildi. Molekül, sahip olduğu geniş π-konjugasyonu sayesinde optoelektronik temelli uygulama alanları için adaydır.

Anahtar Kelimeler: perilen, rutenyum(II), iridyum(III), BODIPY, singlet oksijen, fotodinamik terapi.

ACKNOWLEDGEMENTS

I would like to express my sincere thanks to Prof. Dr. Fatma Yüksel for her endless guidance and support throughout my thesis study. Her suggestions and encouragement gave me the drive and will to complete this work. Also, her efforts in my career will never be forgotten.

I would also like to thank all Fatma Yuksel's research group members, Ercan Duygulu, Semih Akbay, Sevde Demir and Meltem Bayar for their help and support during my doctoral study. Moreover, I should also thank to Zeynep Münteha Şahin, Burcu T. Aksoy and Semiha Y. Sarıkaya for their friendship and endless help that I always felt during my chemistry life in Gebze Technical University.

I would like to express my sincere thanks to Dr. Esra Tanrıverdi Eçik for his collaboration to this research. Her guidance and helpful behavior made this thesis valuable.

I also should express my thanks to my beloved husband Emrah Aksakal for his limitless love and support. I also want to thank my little boy, Ozan Emre, for his existence that brightened our life. I would also like to thank my family for their endless love, tolerance and support.

I would like to thank to Hasan Hüseyin Kazan for *in vitro* PDT studies that enriches the study.

Finally, I would like to thank GTU BAP-2017-A102-15 for financial support during my PhD study at GTU.

TABLE of CONTENTS

LIST of ABBREVIATIONS and ACRONYMS

Abbreviation and Acronyms		**Explanations**
$^1O_2$	:	Singlet Oxygen
$^1O_2$ QY	:	Singlet Oxygen Quantum Yield
$^3O_2$	:	Molecular Oxygen
BODIPY	:	Borondipyrromethane
DMF	:	Dimethyl Formamide
DMSO	:	Dimethyl Suphoxide
DPBF	:	1,3-diphenyl isobenzofurane
ETM	:	Electron Transport Material
EtOH	:	Ethanol
FTIR	:	Fourier Transform Infrared Spectroscopy
FTIR	:	Fourier Transform Infrared Spectroscopy
g/mL	:	gram/ mililiter
H_2SO_4	:	Sulfuric Acid
HClO	:	Hypochlorous Acid
HNO_3	:	Nitric Acid
ISC	:	Intersystem Crossing
K_2CO_3	:	Potassium Carbonate
KOH	:	Potassium Hydroxide
LEC	:	Light-emitting Electrochemical Cell
LiCl	:	Lithum Chloride
MALDI	:	Matrix Assisted Laser Desorption Ionization
MB	:	Methylene Blue
MeCN	:	Acetonitrile
MLCT	:	Metal Ligand Charge Transfer
NaOH	:	Sodium Hydroxide
NIR	:	Near Infrared
NMP	:	N-methyl Pyrrolidone
NMR	:	Nuclear Magnetic Resonance Spectroscopy
OFET	:	Organic Field-effect Transistors

OLED	:	Organic Light-emitting Diode
OPV	:	Organic Photovoltaic Cell
PDI	:	Perylenediimide
PDT	:	Photodynamic Therapy
PS	:	Photosensitiser
PSC	:	Perovskit Solar Cell
ROS	:	Reactive Oxygen Species
TCSPC	:	Time Correlated Single Photon Counting
$Zn(OAc)_2$	:	Zinc Acetate
ZnSe	:	Zinc Selenide
λ_{ex}	:	Excitation Wavelength
$\Phi\Delta$	:	Singlet Oxgen Quantum Yield

LIST of FIGURES

LIST of TABLES

1. INTRODUCTION

Over the last decades organic dyes and their metal complex derivatives gained respectable attention due to their excellent photophysical and photochemical profile in order to use in various applications. One of the application is photodynamic therapy (PDT) which is a popular therapeutic procedure to fight against cancer cells. Designing a photosensitiser for PDT purposes requires a good singlet oxygen quantum yield and tunable photophysical and photochemical property. There exists very few examples of ruthenium/iridium perylene and BODIPY metal complex examples as a photosensitiser in the literature.

In this thesis, we focused on the combination of ruthenium and iridium metal complexes with organic dyes such as perylene and BODIPY in order to search their photophysical properties and photochemical behaviour for future PDT studies. During the study, we worked with human cancer cell lines like Hela and K562 to investigate *in vitro* PDT efficiency of the target molecules.

2. GENERAL INFORMATION

2.1. Organic Dyes

Organic dyes are conjugated coloured molecules that have been widely used for decades. These compounds are attractive due to their wide application area such as ink-jet printing, imaging and electronical uses [1]. These dyes, especially the ones having NIR absorbance gained attention for the application in the nanomedicine area. Many NIR dyes like cyanines, tetrapyrroles, squaraine derivatives and borondipyrromethane (BODIPY) dyes are used as therapeutic agents owing to their chemical and photostability, unique fluorescent properties and desirable molar extinction coefficient. Beside these properties, they also exhibit great ability to target tumor cells in the biology and good water solubility. To sum up, these dyes are encouraging photosensitisers in the cancer treatment processes [2]. Some of these organic dyes are shown in Figure 2.1.

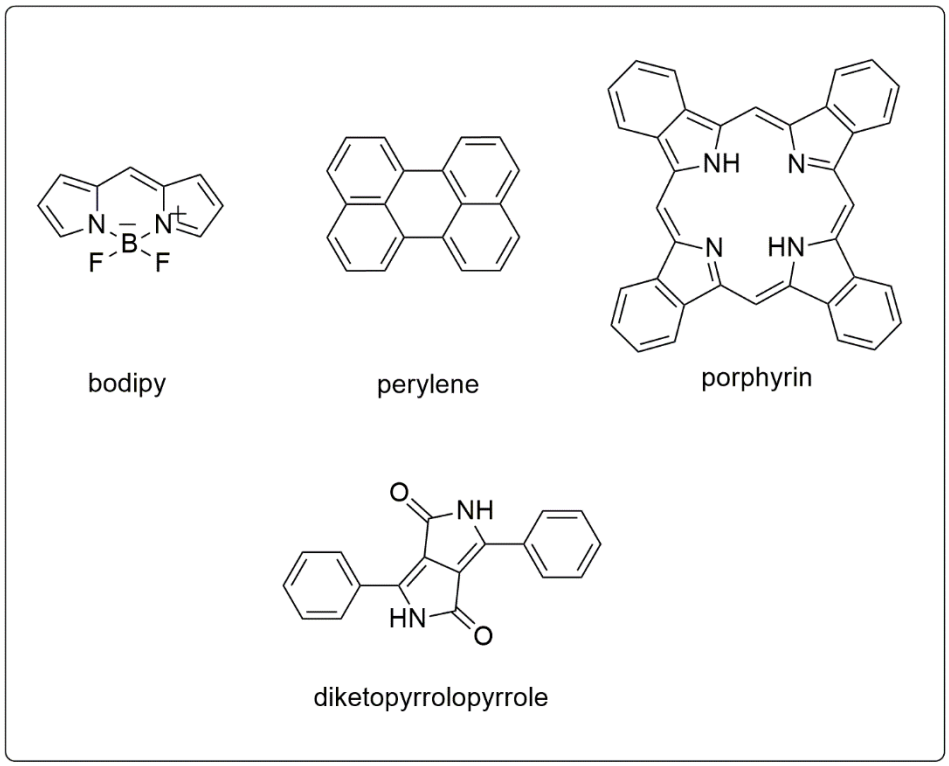

Figure 2.1: Structures of some dyes.

2.2. Perylenes

Perylene constitutes a widespread example of the organic dyes. Perylene dyes have gained great attention of scientists for 100 years after the Kardos's discovery. This unique compound belongs to a class of rylene dyes. Perylenes are one of the significant dyes that belong to the n-type semiconductor class. This valuable core has twelve possible positions, namely, peri- (3,4,9,10-), ortho- (2,5,8,11-) and bay- (1,6,7,12-) positions (Figure 2.2) [3].

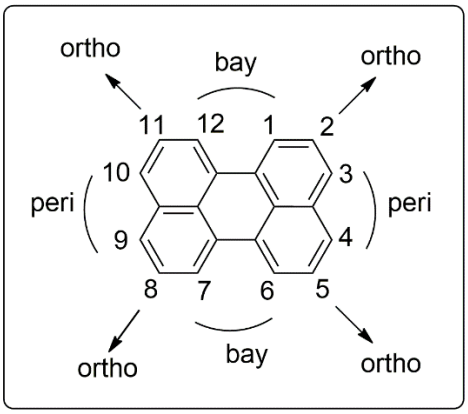

Figure 2.2: Functionalization positions of perylene core.

Many reactions can be applied to perylenediimides such as nucleophilic substitution, imidization and cyclodehydrogenation [3]. Functionalization of perylene core can change many properties such as electronic and optical properties, aggregation and solubility behaviour [4]. Especially, the substitution from bay-positions of these molecules provides great pathway to vary the electronic and optical features of perylenediimides (PDIs) [3]. Due to the derivatization opportunity, perylenes are used in organic field-effect transistors (OFETs) [5], [6], electrophotographic devices [7], dye lasers [8], [9] and organic photovoltaic cells (OPVs) [10], [11]. Due to the fact that perylene complexes have notable absorption coefficient in the visible region of the spectrum these complexes are also valuable in photochemical processes initiated by light including singlet oxygen formation and photodynamic therapy processes [12]. Additionally, a large number of PDIs, exhibited good results in the generation of reactive oxygen species [13], [14].

Owing to the facile and reversible reduction of perylenediimides, wide optical absorption scale in the visible to near-infrared region scientists designed many PDI derivatives recently [15].

2.3. Functionalization of Perylene Diimides

Derivatization of perylene-3,4,9,10-perylene tetracarboxylic acid diimides can be performed by introducing aryl or alkyl substituents to bay positions or N-positions of the unit in order to have soluble PDIs with improved optical and electronic properties [16]. There exist many PDI derivatization studies in the literature. In 1981, Nagao and his co-worker carried out one of the perylene imide derivatizations [17]. In this procedure, they used 3,4,9,10-perylene tetracarboxylic anhydride and alkylamines in order to get PDI derivatives (Figure 2.3). As one of the first examples of imide formation reactions, the yields were between 75-80 %.

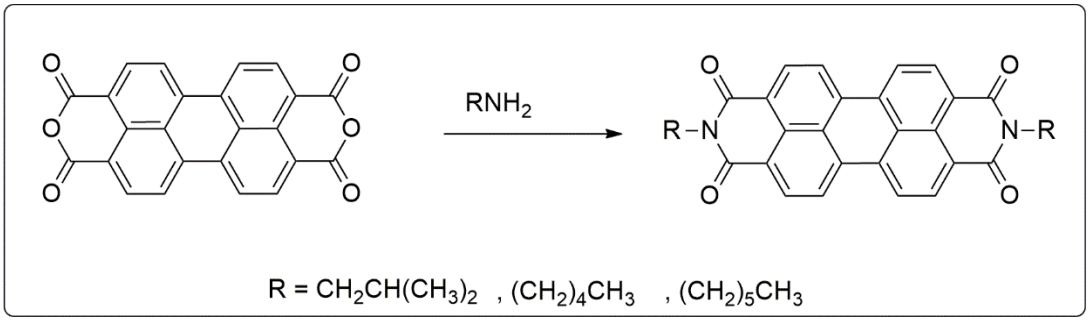

Figure 2.3: Synthesis of PDI derivatives.

Another work was conducted by Dubey and co-workers were about bay-substitution of perylene units (Figure 2.4) [18]. As in this study, aromatic alcohols with alkyl chains are generally used for increasing solubility of the molecule. Here *tert*-butyl phenoxy group was used to substitute chlorines.

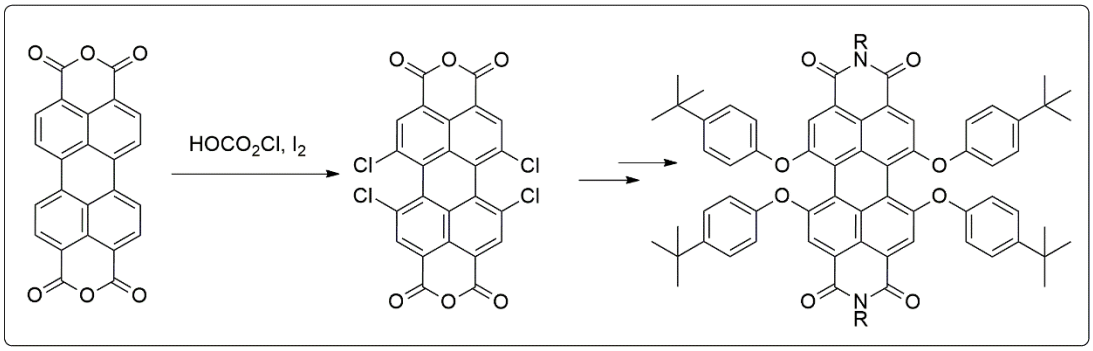

Figure 2.4: Bay- substitution of perylenes.

In the *ortho*-substitution of perylenes the study published by Wu and his team is a valuable example to discuss [19]. Here, ortho-halogenation of perylenes is produced with a rhodium catalyst. They performed tetra iodination of perylene precursor successfully (Figure 2.5).

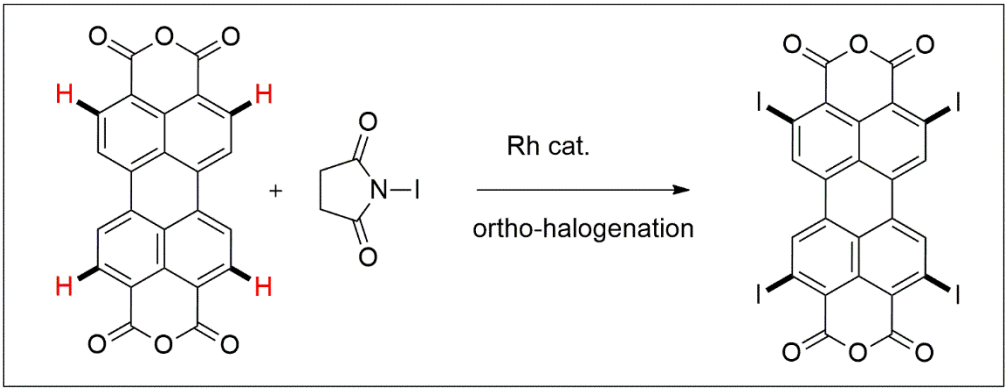

Figure 2.5: Ortho- substitution of perylenes.

Another study that is related with bay-substituted perylenes for PDT applications is given in Figure 2.6 [20]. In this study, singlet oxygen quantum yields of different perylenes having pyrene, phenyl or indole units were investigated as PDT agent. Also the DNA studies of these molecules were demonstrated in this paper.

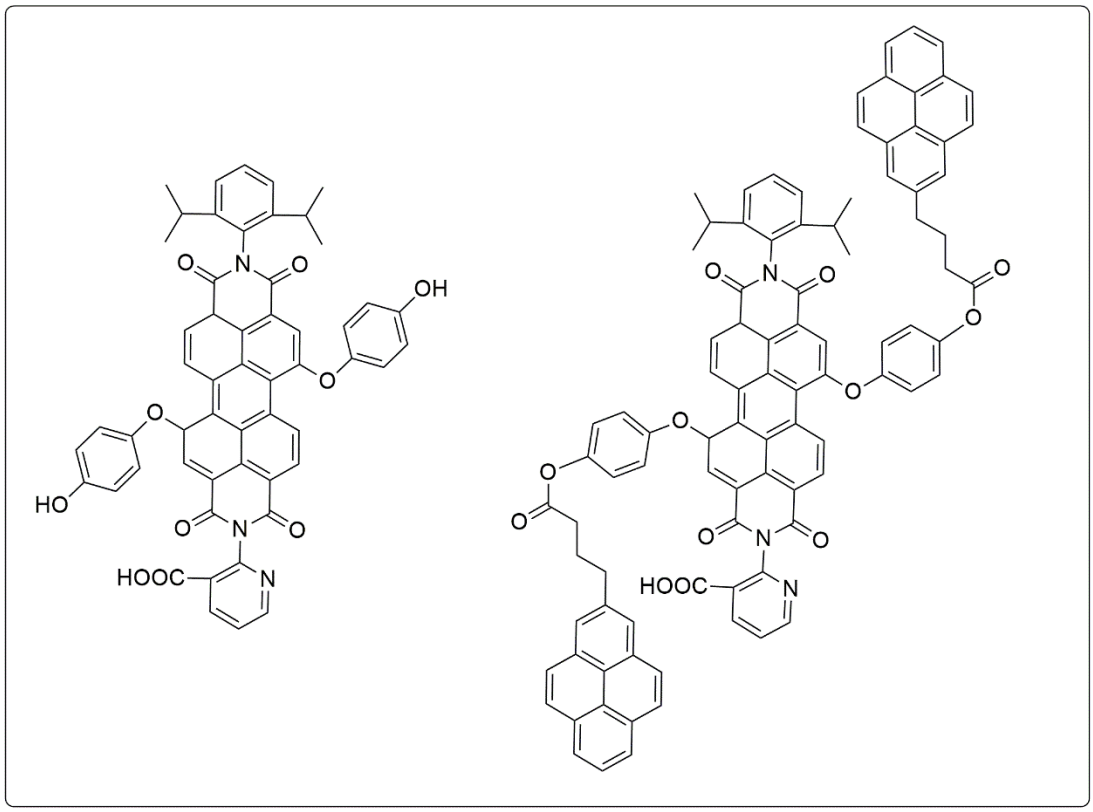

Figure 2.6: Bay-substituted perylene diimides.

In the communication published in Angewandte Chemie in 2019, a novel perylene-fullerene hybrid molecule was designed as an electron transport material (ETM) for perovskite solar cell (PSC) applications [21]. The device having perylene-fullerene interlayer showed great efficiency for PSCs (Figure 2.7).

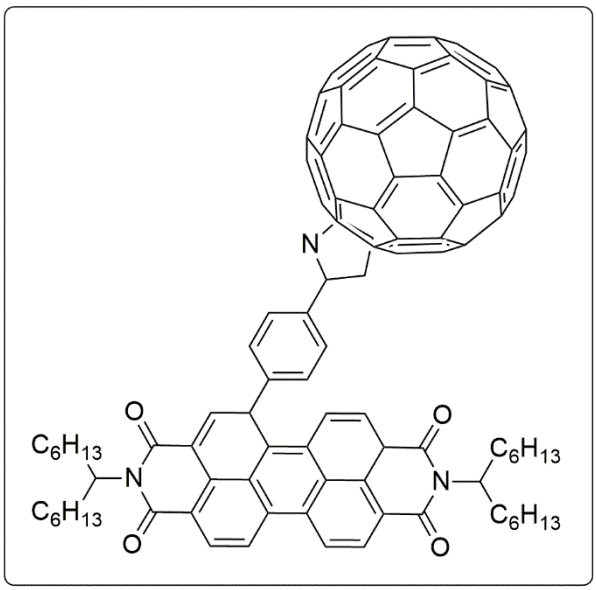

Figure 2.7: A perylene-fullerene hybrid molecule.

According to the literature library of perylenes, we can say that, they are encouraging candidates for many applications due to their functionalization properties. With this knowledge, perylene played key role in this thesis study.

2.4. BODIPYs

Over the last three decades, Boron-dipyrromethene (4,4-difluoro-4-bora-3a,4a-diaza-sindacene, BDP or BODIPY) dyes have been the centre of respectable attention (Figure 2.8). After the discovery of BODIPYs by Treibs and co-workers in 1968 [22], they have been used for many purposes like chromogenic probes [23], biomolecular labels [24], drug delivery agents [25], light-harvesters [26], laser dyes [27], and solar cell sensitizers [28]. The most important features of BODIPYs can be noted as low excited triplet state generation, great fluorescence emission and absorption profile in the visible region, good photochemical stability, chemical strength and fine solubility in organic solvents [22], [29]. Also, large conjugation and the rigid structure of these dye, makes it a good nominee in order to test in deep tissues [30]. The basic structure of BODIPY is given in Figure 2.8.

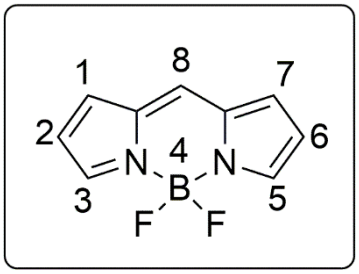

Figure 2.8: Molecular structure of BODIPY core.

Due to the unique properties BODIPY have, it received great interest as fluorophores in bioimaging, biological labelling and fluorescence assays. By modifying the structure of these molecules, the desired spectroscopic and photo-physical characteristics can be provided [31]. Therefore, BODIPY derivatives have been changed for reducing fluorescence and improve intersystem crossing (ISC) as photosensitisers (PS) for biological applications [32]. Moreover, adding heavy atoms directly to the s-indacene ring of the BODIPY, these fluorophores can be easily used in PDT [33]. Especially in the last years, BODIPY molecules have been accepted as a powerful PS in order to kill microbial cells [34]. Some of the potential photosensitiser BODIPY examples are given in Figure 2.9.

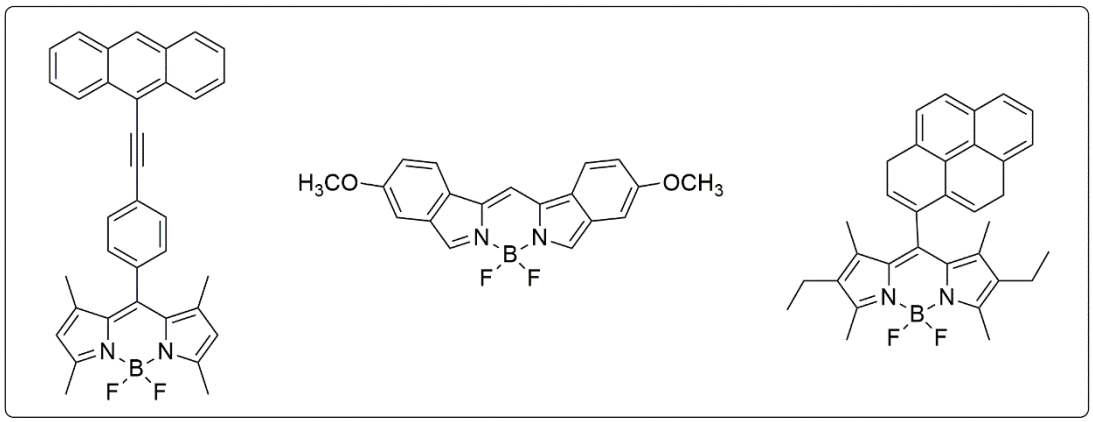

Figure 2.9: Some of the BODIPY examples.

2.5. BODIPYs in the Literature

BODIPY derivatives have been proposed for many applications due to the unique and modifiable absorption and fluorescence properties they have. In the work

published by Jin and his co-workers, water-soluble BODIPY-based probes were investigated for hypochlorous acid (HClO) in living cells [35]. In this work, pyridinium salt increased the water solubility of the main structure that used as fluorescent probe (Figure 2.10). The probe exhibited remarkable response for the finding of HClO in living cells.

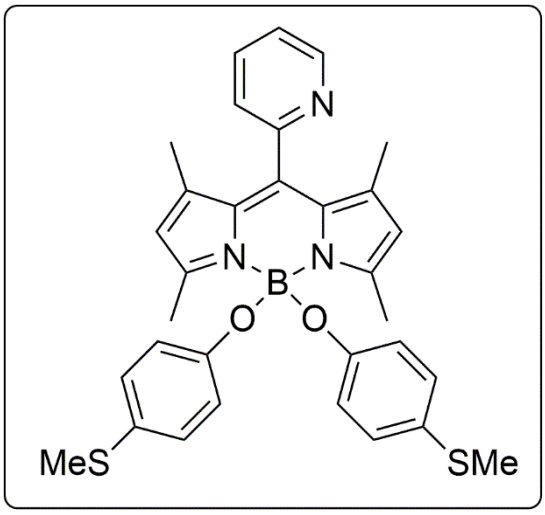

Figure 2.10: A water-soluble BODIPY.

In another study published in Journal of Luminescence in 2019, β-β directly linked BODIPY oligomers were synthesized and studied according to their photophysical and photochemical characteristics (Figure 2.11) [36]. As a result, cell imaging and singlet oxygen generation studies showed that these oligomers are promising candidates for fluorescence imaging and PDT.

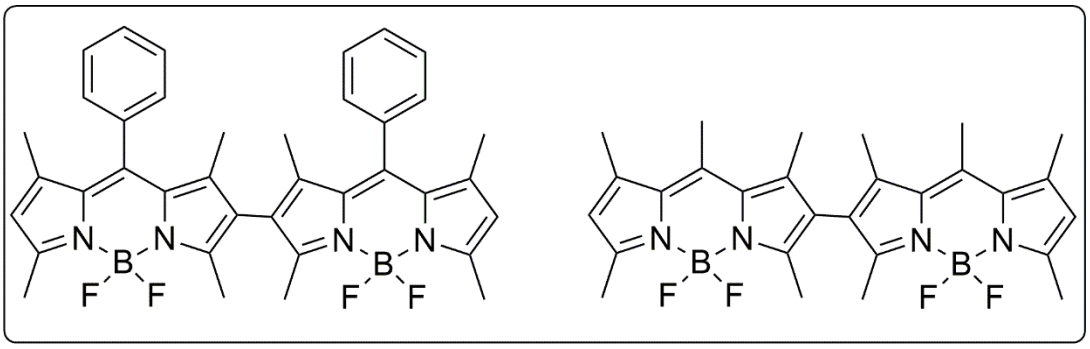

Figure 2.11: BODIPY oligomers.

Other example of BODIPY study was published in Journal of Inorganic Biochemistry in 2018 [37]. In the study which is conducted by Gupta and co-workers, binuclear ruthenium(II) BODIPY organometallic compounds were prepared (Figure 2.12). The antiproliferative properties of these molecules were studied *in vitro* in various human cancer cell lines.

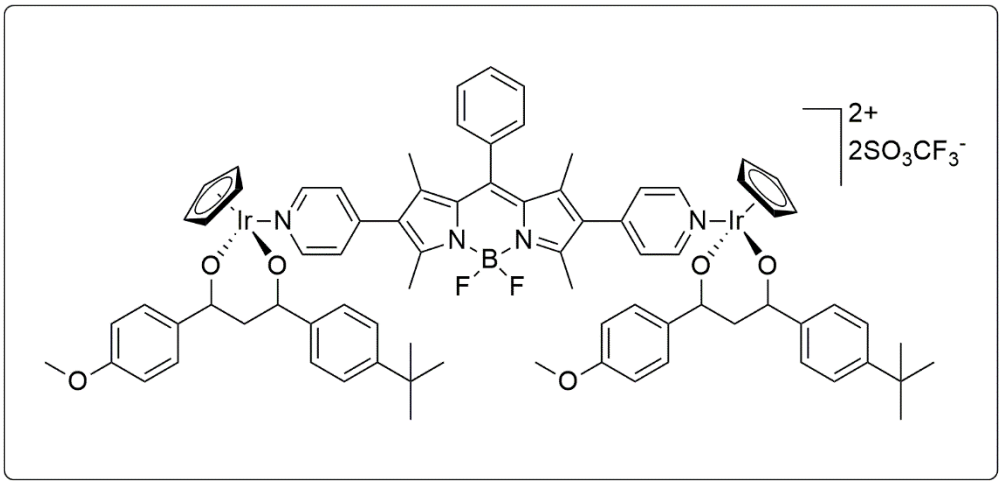

Figure 2.12: Ruthenium(II) dinuclear BODIPY organometallic molecules.

In the study published by Ecik and her group in Journal of Luminescence meso-piperidine linked BODIPY compounds were synthesized [38]. In their work, photophysical studies of the compound were investigated, also the cell imaging and cytotoxicity studies of the targeted molecules were conducted successfully (Figure 2.13).

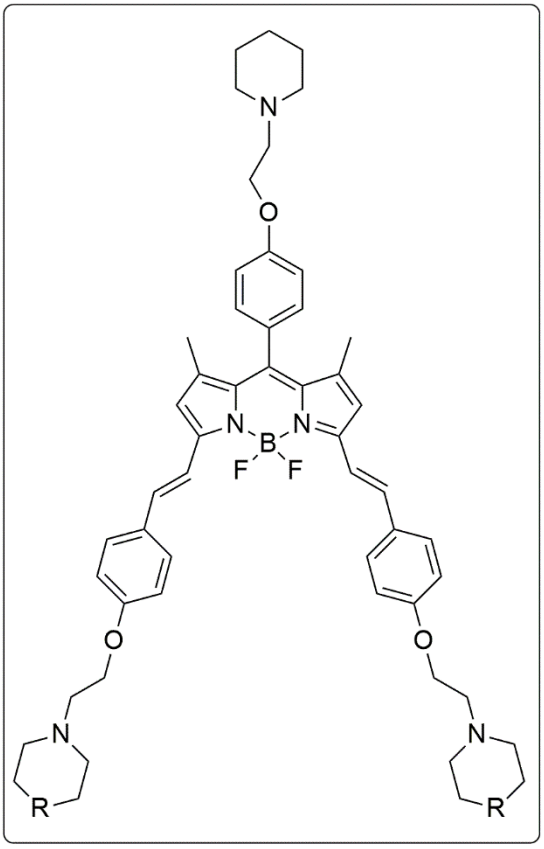

Figure 2.13: Piperidine linked BODIPY.

2.6. Ruthenium and Iridium Metal Complexes

Transition metal complexes form a large family of medicinal agents, photosensitisers and also they play important roles in organic field effect transistor systems [39]. Among these, heavy metals like iridium and ruthenium gained great interest of chemists in optoelectronic, biosensing and bioimaging fields during the last years [40]. Iridium metal is usually highly active in electroluminescence applications like light-emitting electrochemical cells (LECs) and organic light-emitting diodes (OLEDs). The emission maxima of iridium can exhibit changes from blue (452 nm) to red (687 nm) region of the spectrum which makes it suitable for OLEDs [41]. As well as iridium, ruthenium complexes are also applicable in OLEDs and LECs. However, iridium is much more useful because of its colour tunability, higher stable complexes and higher quantum yields when compared [42]. Although there isn't plenty of iridium metal application in photodynamic therapy (PDT), many papers reported the

cyclometallated Ir metal examples as unique photosensitisers in singlet oxygen production studies and cellular imaging agents [43]. Moreover, they are getting more popular because of their wide emission wavelength range, sensitive excited states and efficient cell permeability during biological studies. Iridium(III) complexes can be used applied as photosensitizing agents in order to harm cancer cells upon irradiation because they have triplet excited state and cause singlet oxygen production [40].

Ruthenium(II/III) complexes are commonly known as their anticancer and antimetastatic properties [44]. They are widely used in biological fields since they are readily absorbed by tumour tissues and they are discharged *in vivo* easily [45]. These complexes are highly demanded because of their various oxidation states, reduces toxicity behaviour in *vivo* and ligand substitution kinetics [46]. Ruthenium compounds possess a unusual modular system when compared to small molecule bearing drug [45]. The potential biological activity behaviour of these complexes comes from the 3D arrangement of ligands that dramatically affects the modifications of solubility, cellular uptake level, targeting ability and ROS (reactive oxygen species) yield, *etc* [47]. There exists many examples of iridium and ruthenium metal complexes in the literature. One example of ruthenium(II) and iridium(III) metal complex having perylene unit is published in Angewandte communications in 2015 (Figure 2.14) [48].

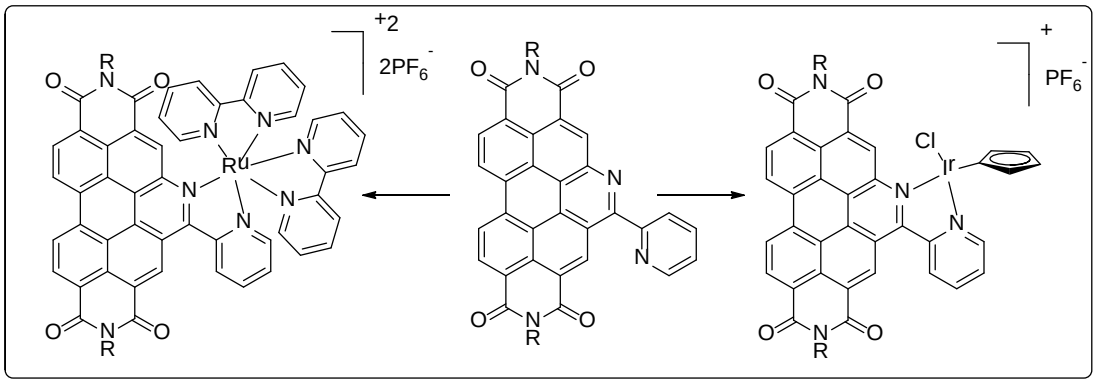

Figure 2.14: Ruthenium(II) and iridium(III) metal complexes with perylene unit literature examples.

In their study, perylene was substituted from the bay position with ruthenium and iridium starting compounds and phosphorescence emission properties were investigated.

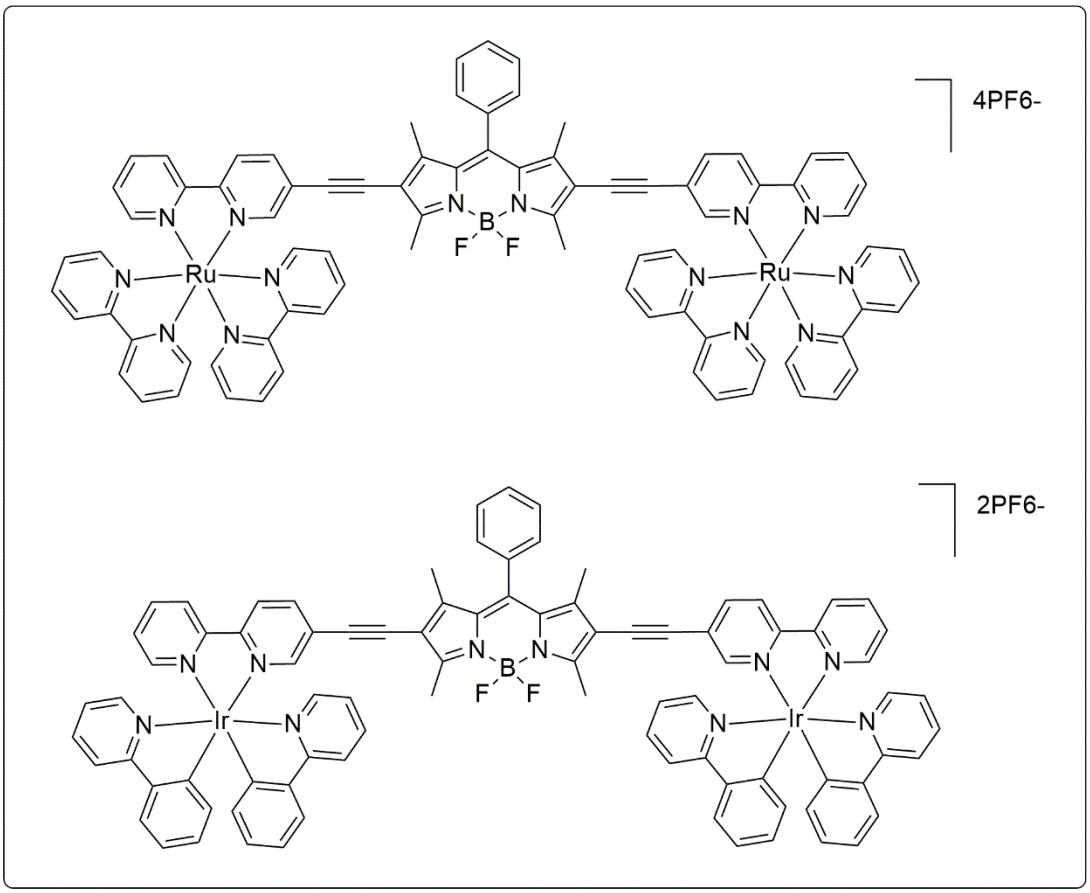

Figure 2.15: Ruthenium(II) and iridium(III) BODIPY complex examples.

In another study conducted by Wang and co-workers, ruthenium and iridium BODIPY complexes synthesized and their activity in photodynamic therapy was investigated successfully (Figure 2.15) [49].

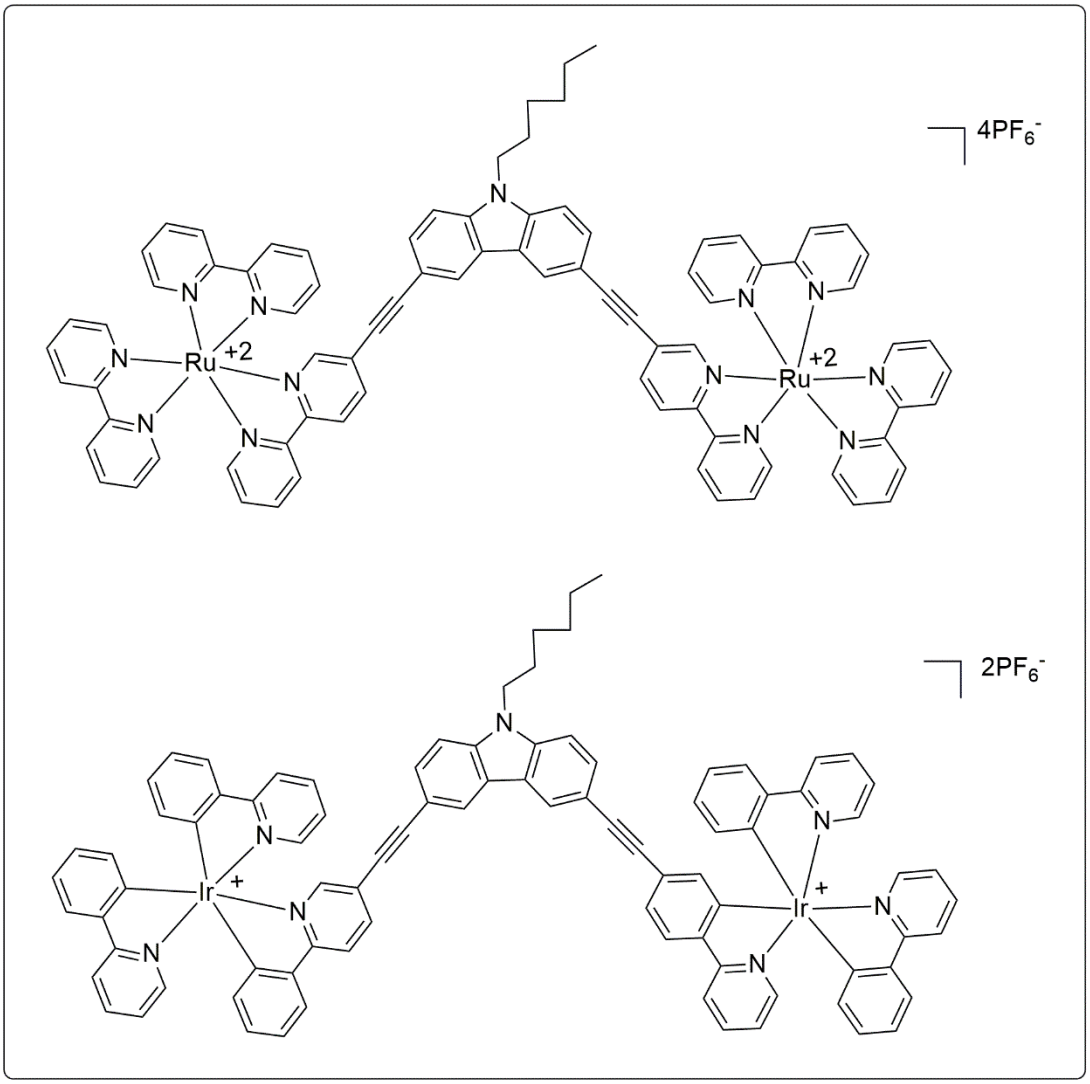

Figure 2.16: Ruthenium(II) and iridium(III) photosensitisers.

In 2018, there published examples of iridium and ruthenium compounds in Chemical Communications (Figure 2.16) [50]. According to the study, N-substituted carbazoles having ruthenium and iridium complexes increase the absorption in the visible region and they can be accepted as good triplet photosensitisers.

Another research was conducted by Stringer et al. was demonstrated design and in vitro investigations of ruthenium(II) and iridium(III) quinoline metal complexes (Figure 2.17) [51]. These compounds were studied in vitro for antiplasmodial activities against of the malaria parasite. According to the results observed, they were found to show good activities and low toxicity towards the malaria parasite.

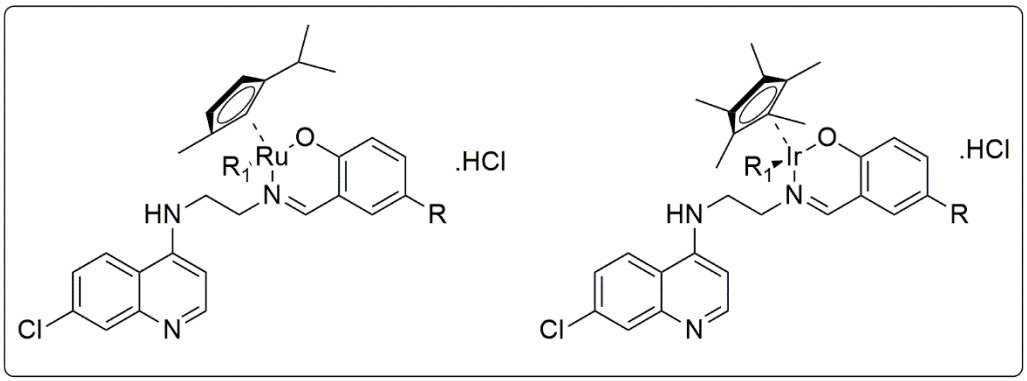

Figure 2.17: Ruthenium(II) and iridium(III) metal complexes.

In Figure 2.18, another valuable study was demonstrated that is published in JACS in 2012 [52]. In this work, different kind of Ru(II) complexes were synthesized and their biological effects in terms of DNA binding, cytotoxicity, protein binding and mitochondrial staining studies were investigated.

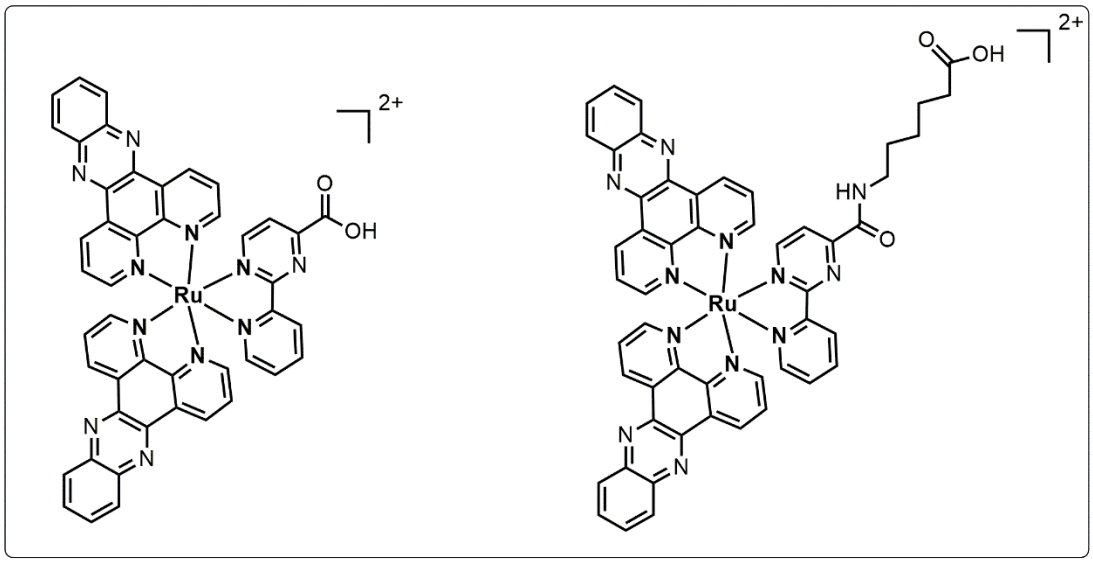

Figure 2.18: Ruthenium(II) complexes.

In another paper published by Mckenzie and co-workers, iridium(III) metal complexes were designed and investigated spectroscopically (Figure 2.19) [53]. They demonstrated long-lived and photo-stable iridium compounds having low-molecular weight and high TP-absorption aiming to penetrate lysosomal and mitochondria structure cells. Final products showed good efficiency with cell death in diverse cancer cell tissues.

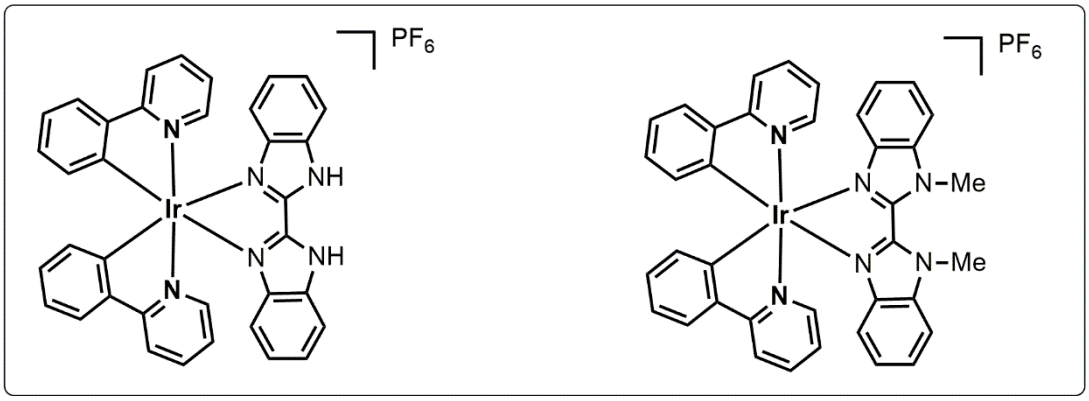

Figure 2.19: Iridium(III) metal complexes.

Although there are many application possibility of these ruthenium(II) and iridium(III) metal complexes, most of them possess biological and opto-electronic purposes in the literature.

2.7. Photodynamic Therapy

Photodynamic therapy is a therapeutic procedure which is applied in clinics in order to fight cancer cells [54]. PDT is a unique technique because of its sensitivity towards healthy cells and tissues [55]. In PDT, a photosensitising agent is intravenously injected to a tumour cell then it decomposes with the light irradiation. During this procedure, there produced toxic components that destroy only the cancerous cells but not the normal tissue. PDT studies can be applied on many cancer types like lung cancer, cancer of urinary bladder, breast cancer and gastrointestinal tumours [56].

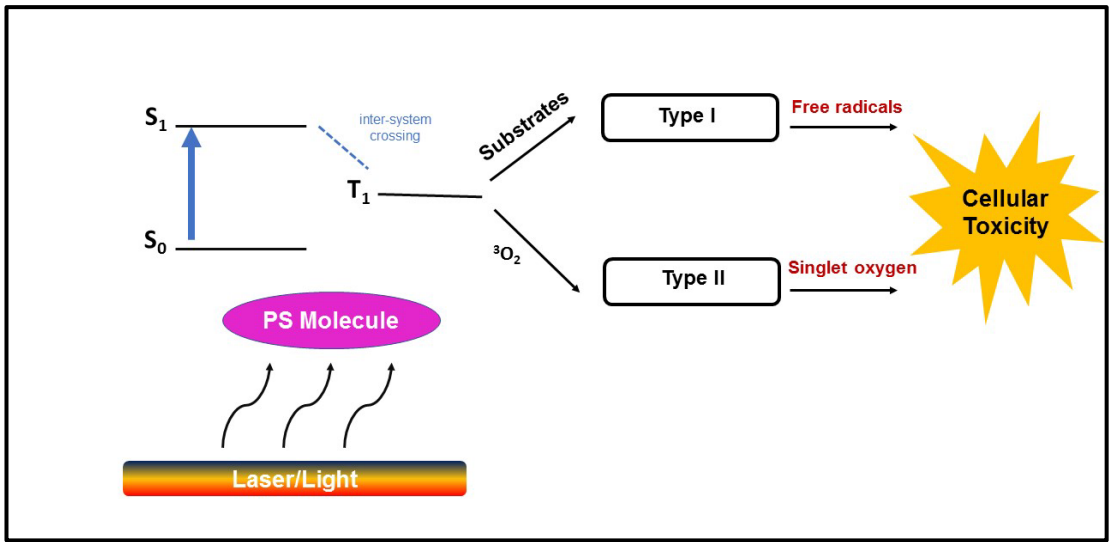

Figure 2.20: Working principle of PDT.

In PDT process, there exist two steps (Figure 2.20). First one is fluorescence emission that formed after the turning of the excited photosensitiser to its ground state (Figure 2.20). In the second process, toxic singlet oxygen is formed and kills the cells. The photosensitisers should be a molecule with an absorption maximum correlated with that incident light. The excited photosensitiser can turn back to the ground state with fluorescence after adsorption step. If the lifetime of the excited state is short, the excess energy could be used to begin other chemical reactions. With oxygen molecule there may exists two types of chemical reactions, Type I and Type II (Figure 2.20) [57].

In the Type I mechanism, active PS leads to form a radical that give their excess energy to molecular oxygen ($^3O_2$) for producing singlet oxygen ($^1O_2$) and other reactive species. In Type II process, the PS directly transfers its energy to $^3O_2$ that then turns into $^1O_2$ [57]. In most of the PDT studies, Type II is preferred as in our case. In this mechanism, production of singlet oxygen which is toxic for tumours is used against microorganisms.

PDT provides many advantages when compared to other tumour treatment techniques. One advantage is that PDT is non-invasive over other methods like surgery. Other benefit is selectivity ability of targeting cancer cells. Another essential advantage of PDT can be stated as without limitations, repetitive treatments can be applied such as radiotherapy. Lastly, because the lifetime of singlet oxygen generated by PDT is very limited, it only harms the cell in which it is produced [57].

3. RESEARCH OBJECTIVES

Ruthenium and iridium metal complexes are famous transition metals because of their superior biocompatibility, variable photophysical and chemical and excited-state characteristics, large Stoke's Shift, fine photostability and high quantum yield [58], [59].

Recently, ruthenium complexes have made a splash as photosensitiser in PDT and related biological investigations, owing to their intriguing singlet oxygen quantum yields and tuneable photochemical and photophysical properties. Like ruthenium, one group of the potential PS candidates are iridium complexes which possess hopeful anticancer behaviour because of their great quantum yield and good photostability [60]. Although these metal complexes bear unique features for PDT purposes, they have weak absorbance in the NIR (near infrared) and red region, short-lived triplet excited states and absorption wave-length [60]. In order to overcome this problem strong NIR or far-red chromophores like perylene or BODIPY are connected with transition metals [61].

In this thesis we have chosen perylene and BODIPY organic dyes in order to form original ruthenium and iridium metal complexes. Due to the large π-conjugation system perylene have, MLCT absorption band bearing a red-shift and an improved molar extinction coefficient were obtained [62]. In order to eliminate the low solubility and aggregation difficulty of perylene, the main core has been derived from the bay positions in the present study. In addition to perylene dyes, we have chosen BODIPY as other potential organic fluorophore in this thesis. It belongs to the fluorophore family bearing supreme thermal and photochemical stability, narrow emission and good absorption features around near-IR and visible regions [63]. Developing a photosensitiser that is excited efficiently at wavelengths exceeding 658 nm is crucial in PDT studies, for this purpose a novel distryl BODIPY was used in the present work [64]. Moreover, complex formation of heavier halogen addition or can upgrade the ISC ability of the BODIPY and also bioavailability can be improved by attaching a metal ion.

In this thesis, we combined perylene and BODIPY organic dyes with ruthenium and iridium heavy metals in a novel way for biological purposes.

The first part of our study includes novel ruthenium(II) and iridium(III) perylene complexes. For the formation of this complexes we used two main points, one is substitution from 4,7-position of phenanthroline ligand (Figure 3.1). In general, substitution of ruthenium complexes having phenanthroline units are built from 5- or 5,6- positions with some chromophores and there exists only a few perylene bearing examples substituted from 5-position of phenanthroline [65]. Therefore, this research can be represented as the first example of a phenanthroline-based metal complex having two perylenediimide dye substituted from 4,7-positions [66], [67]. Moreover, planning a metal complex having two PDI and Ru(II) polypyridyl parts is also unique in the literature.

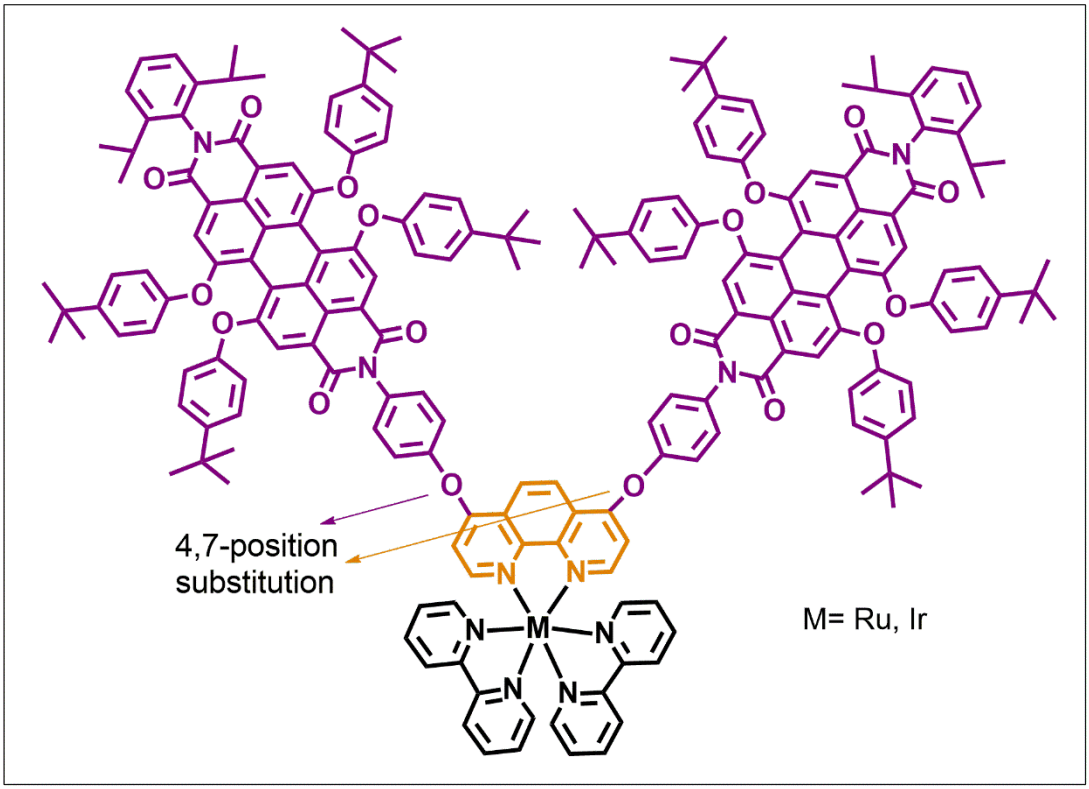

Figure 3.1: Structure of 4,7-substituted metal complexes.

In the second part of the study, the final aim was the set-up of two novel iridium and ruthenium metal complexes bearing two distryl BODIPY compounds for investigating photosensitizer capability and photodynamic therapy efficiency (Figure 3.2). This unique pattern involves a phenanthroline unit with 4,7-substitution and two novel BODIPY moiety which can be presented as a novel example of BODIPY iridium and ruthenium metal complexes.

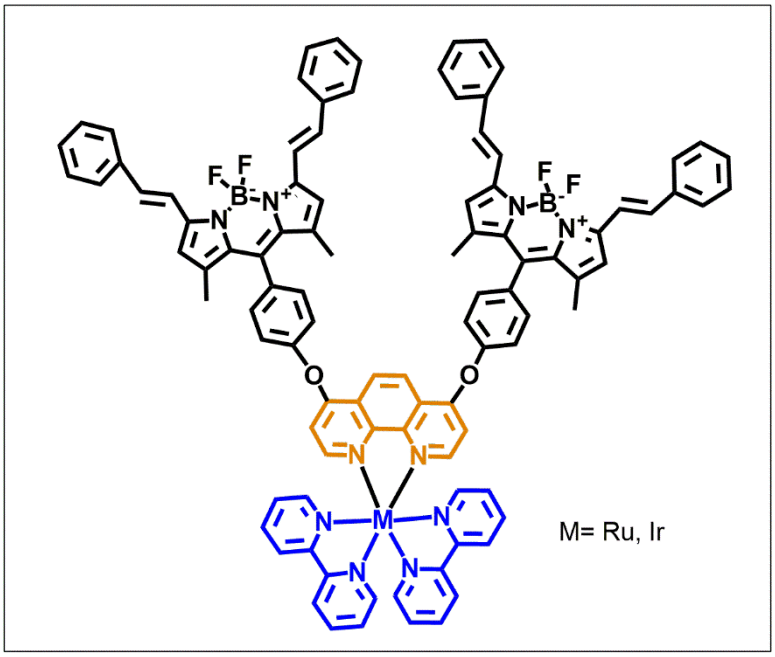

Figure 3.2: Structures of BODIPY metal complexes.

The synthesized molecules were fully characterized and the photophysical properties were studied with florescence and UV-Vis spectroscopy. Photochemical studies of the three complexes were conducted by studying singlet oxygen generation abilities. Moreover, the potentials of the target compounds photosensitizing agents for PDT were applied on cancerous cells such as leukemia and human cervical cancer cells.

In addition to this work, we also aimed to synthesize benzimidazole-fused perylene ruthenium(II) metal complex. This can be also accepted as the first example of imidazole bearing perylene ruthenium connection (Figure 3.3). In this study, due to enhanced π-conjugation through the molecule, we aimed to improve photophysical properties of the molecule for further applications.

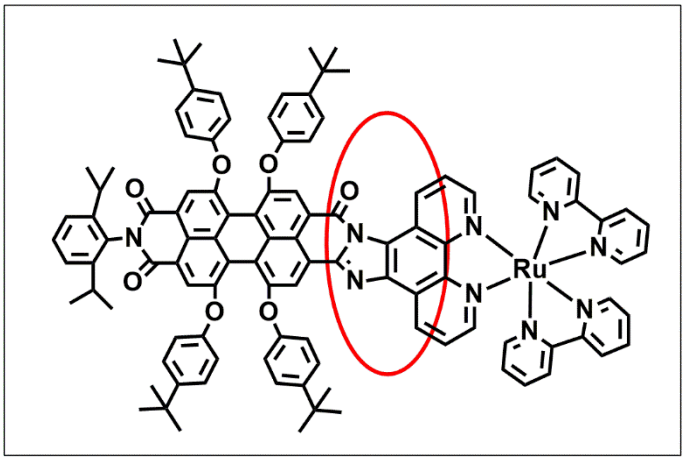

Figure 3.3: Structure of benzimidazole bearing ruthenium perylene metal complex.

All of the synthesized compounds are summarized in the table 3.1.

Table 3.1: List of new molecules in the thesis.

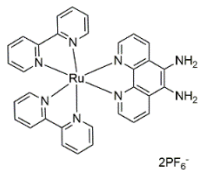	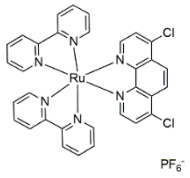
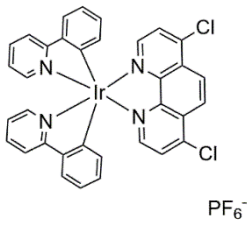	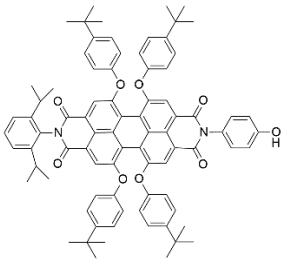
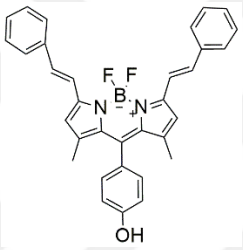	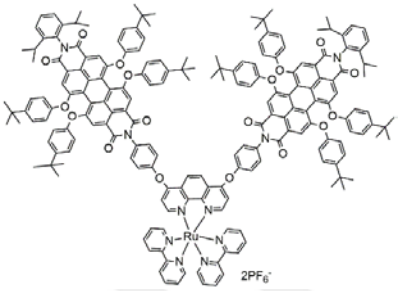
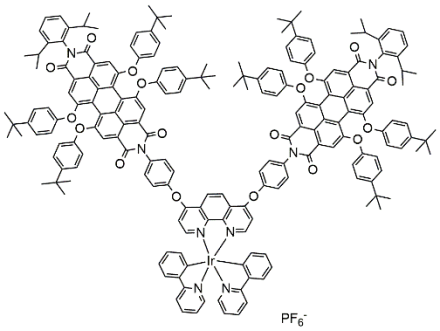	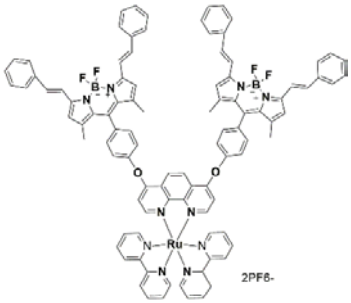
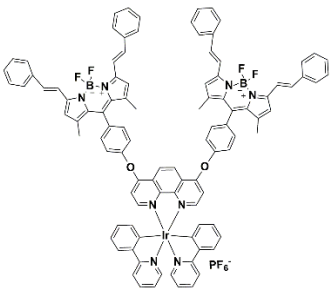	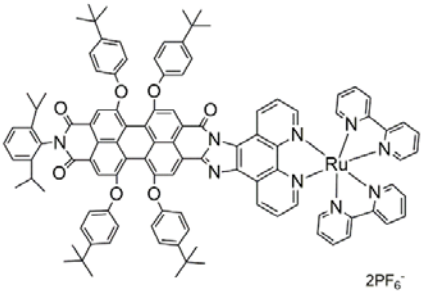

4. EXPERIMENTAL

4.1. Materials

All reagents and solvents were of reagent-grade quality, obtained from commercial suppliers. Infrared spectra were recorded between 4000 and 650 cm^{-1} by using a Perkin Elmer Spectrum100 FT-IR spectrometer with an attenuated total reflection (ATR) accessory featuring a zinc selenide (ZnSe) crystal. The mass spectra were recorded on a MALDI (Matrix Assisted Laser Desorption Ionization) BRUKER Microflex LT using 1,8,9-anthrasenetriol (dithranol) as a matrix. The NMR spectra were recorded on a Varian INOVA 500 MHz spectrometer. Electronic absorption spectra were recorded with a Shimadzu 2101 UV spectrophotometer and the fluorescence excitation and emission spectra were recorded on a Varian Eclipse spectrofluorometer using 1 cm pathlength cuvettes at room temperature. Fluorescence lifetimes were measured by a time correlated single photon counting (TCSPC) method using FLUOROLOG-3 spectrofluorometer (Horiba JobinYvon, Edison, NJ) equipped with a NanoLED and a standard air cooled R928 PMT detector.

Table 4.1: Chemicals Used in the Experiments.

Name	Company	Catalog/Cas Number	Type
DMF	Merck	1.03053	Solvent
DMSO	Merck	8.02912	Solvent
SilicaGel 60, 0.063-0.200 mm	Merck	1.07734	For Column Chromatography
o-phenylenediamine	Merck	95-54-5	For Synthesis
Perylene-3,4,9,12-tetracarboylic dianydride	Aldrich	128-69-8	For Synthesis
1,10-phenanthroline	Aldrich	66-71-7	For Synthesis
NH_4PF_6	Acros Organics	16941-11-0	For Synthesis
4-aminophenol	Aldrich	123-30-8	For Synthesis
4-hydroxybenzaldehyde	Sigma-Aldrich	123-08-0	For Synthesis
$IrCl_3.H_2O$	Aldrich	14996-61-3	For Synthesis
$RuCl_3.H_2O$	Aldrich	14898-67-0	For Synthesis
2,6-diisopropylaniline	Aldrich	24544-04-5	For Synthesis
2,2'-bipyridine	Sigma-Aldrich	366-18-7	For Synthesis
p-tertbutyl phenol	Acros Organics	98-54-4	For Synthesis
Bromine	Sigma-Aldrich	7726-95-6	For Synthesis
Propionic acid	Merck	79-09-4	For Synthesis
NMP	Merck	872-50-4	For Synthesis
K_2CO_3	VWR	584-08-7	For Synthesis
KOH	Merck	1310-58-3	For Synthesis
t-BuOH	Merck	75-65-0	For Synthesis
Quinoline	Fluka	91-22-5	For Synthesis
$POCl_3$	Acros Organics	10025-87-8	For Synthesis
$Zn(OAc)_2$	Sigma-Aldrich	557-34-6	For Synthesis
LiCl	Sigma-Aldrich	7447-41-8	For Synthesis
Ethylene glycol	Merck	107-21-1	For Synthesis
MeCN	Sigma-Aldrich	75-05-8	For Synthesis
HNO_3	Merck	7697-37-2	For Synthesis
2,4-dimethylpyrrole	Sigma-Aldrich	625-82-1	For Synthesis
Trifloroacetic acid (TFA)	Sigma-Aldrich	76-05-1	For Synthesis
Triethylamine (Et_3N)	Sigma-Aldrich	121-44-8	For Synthesis
TLC Plate	Merck	-	Purification

Table 4.1: Continued.

Etanol	Sigma	64-17-5	For Synthesis
Diethyl Ether	Sigma	60-29-7	For Synthesis
Acetone-d_6	Merck	666-52-4	For NMR
$CDCl_3$	Merck	845-49-6	For NMR
NH_4OH	Merck	1336-21-6	For Synthesis
HCI	Sigma	7647-01-0	For Synthesis
CH_2Cl_2	Sigma	75-09-2	Solvent
$NaSO_4$	Alfa Aesar	1313-84-4	For Synthesis
H_2SO_4	Merck	7664-93-9	For Synthesis
Acetone	Honeywall	200-662-2	Solvent
THF	Merck	109-99-9	Solvent
4-Hydroxybenzaldehyde	Sigma	123-08-0	For Synthesis
p-Chloroaniline	Sigma	106-47-8	For Synthesis
Benzene	Merck	71-43-2	Solvent

Table 4.2: Instruments Used in the Thesis Study.

Name	Type	Location
FT-IR Spectrometer	Perkin Elmer 100	Gebze Technical University
NMR Spectrometer	Varian Inova 500 MHz	Gebze Technical University
Mass Spectroscopy	Bruker Microflex LT MALDI-TOF MS	Gebze Technical University
Electronic absorption spectra	Shimadzu 2101 UV spectrophotometer	Gebze Technical University
Florouscence emission and excitation specta	Varian Eclipse spectrofluorometer	Gebze Technical University
Flouroscence Lifetime Measurement	FLUOROLOG-3 spectrofluorometer Horiba JobinYvon	Gebze Technical University
X-Ray Diffraction	Bruker	Gebze Technical University
Oven	Thermo scientific	Gebze Technical University
Vacuum Oven	MMM Group Vacucell	Gebze Technical University
Microplate spectrophotometer	Multiskan GO, Thermo Fisher Scientific	Middle East Technical University
Ultrasonic Bath	Bandelin Sonorex	Gebze Technical University

4.2. Synthesis

4.2.1. Synthesis of phenanthrolines

4.2.1.1.Synthesis of 5-nitro-1,10-phenanthroline (2)

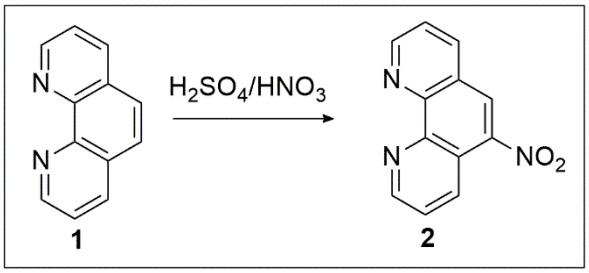

Figure 4.1: Synthesis of 2.

A solution of 1,10-phenanthroline (1 g, 5.5 mmol) and 2 mL H_2SO_4 and fuming 2 mL HNO_3 was stirred at 100 °C for 2 h. After neutralization with NaOH solution, compound **2** was obtained as a brown solid (0.8 g, 64% yield). The structural analyses of **2** have been achieved by using mass spectrometry and FT-IR spectroscopy [68].

Mass Spectrum: MALDI-TOF (m/z) Calc. 225.20, Found: 225 $[M]^+$.

FT-IR ν_{max} (cm^{-1}): 3424, 3083, 2862, 1639, 1590, 1517, 1505 (N=O), 1488, 1447, 1421, 1385, 1354 (N=O), 1311, 1287, 1715, 1146, 1107, 1045, 832, 806.

4.2.1.2.Synthesis of 5-nitro-6-amino-1,10-phenanthroline (3)

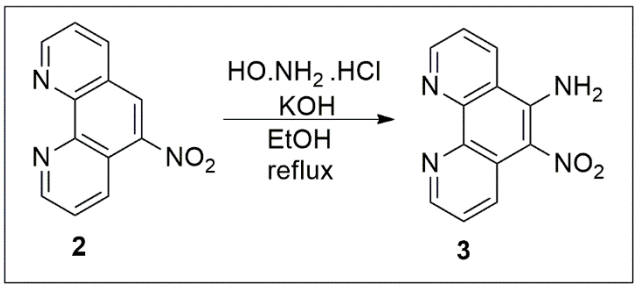

Figure 4.2: Synthesis of 3.

A mixture of **2** (1 g, 4.4 mmol) and hydroxylamine hydrochloride (2.04 g, 29.4 mmol) were refluxed in 50 mL EtOH solution. Then, 2.2 g (39.3 mmol) of KOH in 50 mL EtOH added dropwise to the solution over 45 min. The solution was refluxed for

additional 30 min, cooled, and then poured into 300 mL ice-water. After filtration, and washing with EtOH, water and chloroform, compound **3** was isolated (0.3 g, 36% yield). The structural analyses of **3** have been achieved by using mass spectrometry and FT-IR and MALDI-TOF spectroscopy [68].

Mass Spectrum: MALDI-TOF (m/z) Calc. 240, Found: 240 $[M]^+$.

FT-IR ν_{max} (cm^{-1}): 3400, 3266 (N-H), 3142, 1628, 1596, 1262, 1235, 1173, 1057, 807, 797, 735.

4.2.1.3.Synthesis of 1,10-Phenanthroline-5,6-diamine (4)

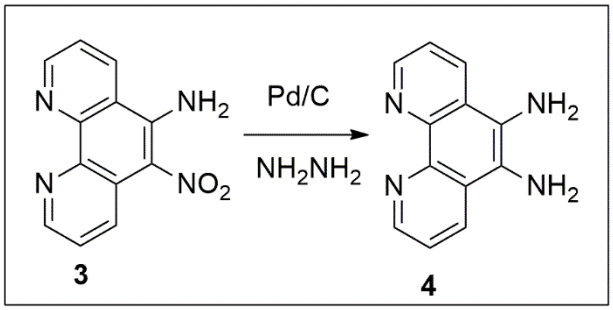

Figure 4.3: Synthesis of 4.

For the synthesis of **4**, 0.2 g (0.83 mmol) of **3** and 0.1 g of 10 % palladium on activated charcoal was refluxed in 200 mL EtOH. Then, 1.0 mL hydrazine hydrate (55%) was added slowly to the mixture over 15 min. The reaction was refluxed for 45 min, filtered. After concentration with vacuum, the precipitate was observed by adding petroleum ether to the concentrated reaction mixture (0.06 g, 67% yield). The structural analyses of **4** have been achieved by using mass spectrometry and FT-IR spectroscopy [68].

Mass Spectrum: MALDI-TOF (m/z) Calc. 210, Found: 210 $[M]^+$.

FT-IR ν_{max} (cm^{-1}): 3346 (N-H), 3228, 1609, 1563, 1486, 1435, 1308, 1111, 797, 731.

4.2.1.4.Synthesis of 1,2-Bis-[(2,2-dimethyl-4,6-dioxo-1,3-dioxan-5-ylidenemethyl)amino]benzene (7).

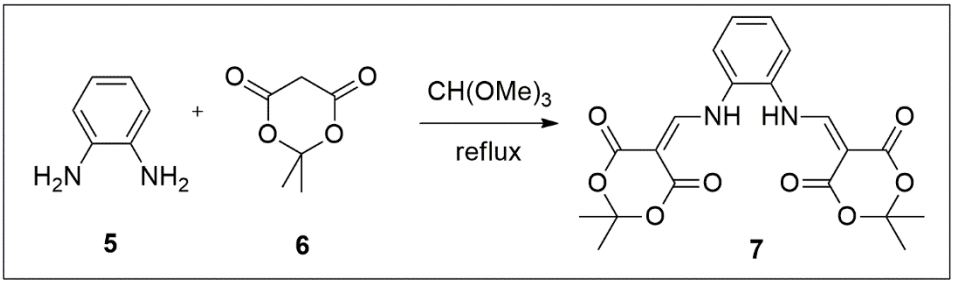

Figure 4.4: Synthesis of 7.

First a mixture of Meldrum's acid (**6**) (5.05 g, 35 mmol) in trimethyl orthoformate (50 mL) was stirred over 2 h under argon gas. Then, *o*-phenylenediamine (**5**) (1.62 g, 15 mmol) was added to the solution and the reaction mixture heated at reflux for an additional hour. After the evaporation of solvent, recrystallisation gave the product **7** (4.25 g, 68% yield). The structural analyses of **7** have been achieved by using mass spectrometry and FT-IR spectroscopy [69].

Mass spectrum: MALDI-TOF (m/z) Calc. 416, Found: 438 $[M+Na]^+$.

FT-IR ν_{max} (cm^{-1}): 3242 (N-H),3011, 2992, 1725 (C=O), 1674, 1611, 1568, 1426, 1388,1374, 1366, 1319, 1263, 1214, 1199, 1138, 1016, 999, 757.

4.2.1.5.Synthesis of 4,7-dione 1,10-phenanthroline (8)

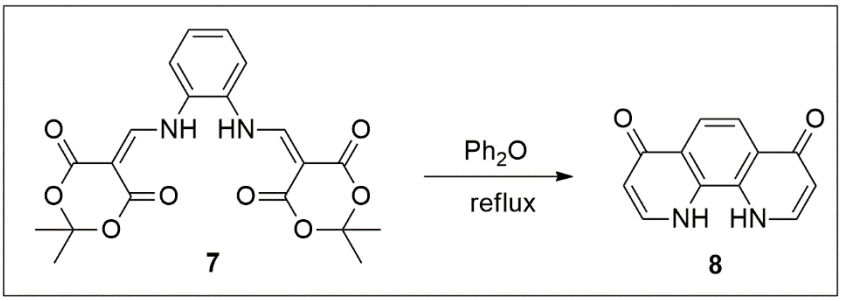

Figure 4.5: Synthesis of 8.

Compound **7** (0.18 mmol) was refluxed in diphenyl ether for 30 minutes in a round bottom flask. Then the reaction is completed, precipitates was filtered and washed with

hexane (0.85 g, 88% yield). The structural analyses of **8** have been achieved by using mass spectrometry and FT-IR spectroscopy [70].

Mass spectrum (MALDI-TOF): MALDI-TOF (m/z) Calc. 212.2, Found: 210 $[M-2H]^+$.

FT-IR ν_{max} (cm^{-1}): 3226, 1726 (C=O, ketone), 1672, 1611, 1568, 1427, 1306, 1261, 1198, 1138, 1016, 998, 932, 857, 803, 787, 757, 740, 722, 644, 603.

4.2.1.6.Synthesis of 4,7-Dichloro-1,10-Phenanthroline (9)

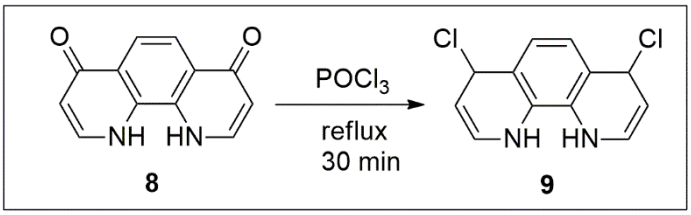

Figure 4.6: Synthesis of 9.

In a flask, compound **8** (0.1 g, 0.47 mmol) was heated 30 minutes in 6 mL $POCl_3$. Next, in the room temperature, the reaction mixture was dropped to the concentrated KOH solution on an ice-bath. After the precipitation of beige solids, we filtrated and washed them with hexane and *p*-dioane (0.02 g, 20% yield). The structural analyses of **9** have been achieved by using mass spectrometry and FT-IR spectroscopy [70].

Mass Spectrum (MALDI-TOF): MALDI-TOF (m/z) Calc. 249, Found: 249 $[M]^+$.

FT-IR ν_{max} (cm^{-1}): 3036, 1609, 1573, 1543, 1487, 1411, 1215.

4.2.2. Synthesis of Ruthenium(II) Complexes

4.2.2.1.Synthesis of bis(2,2'-bipyridine)dichlororuthenium(II) (10)

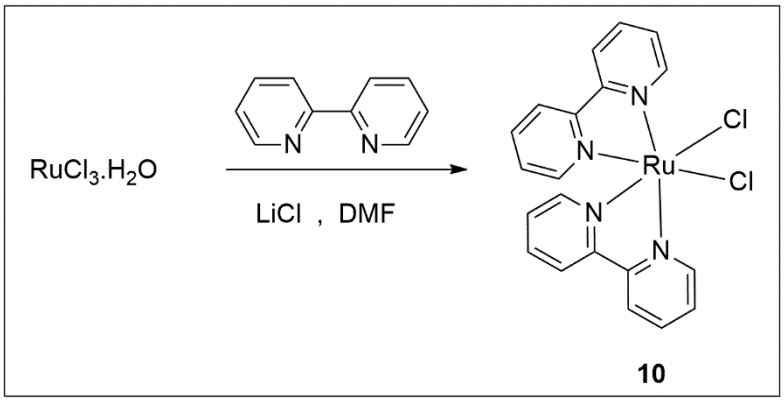

Figure 4.7: Synthesis of 10.

$RuCl_3.H_2O$ (100 mg, 0.48 mmol) and LiCl (123 mg, 2.9 mmol), 2,2'-bipyridine (150 mg, 0.96 mmol) mixture was refluxed in DMF under argon over 12 hours. Dark purple precipitates were obtained after pouring the cold solution into acetone (0.08 g, 40% yield). The structural analyses of **10** have been achieved by using mass spectrometry and FT-IR spectroscopy [71].

Mass spectrum: MALDI-TOF (m/z) Calc. 484.39, Found: 484$[M]^+$.

FT-IR ν_{max} (cm^{-1}): 3041, 1597, 1475, 1457, 1418, 1276, 1260, 1018, 803, 760, 724, 656, 647.

4.2.2.2.Synthesis of 5,6-diamino-phenanthroline ruthenium(II) complex (11)

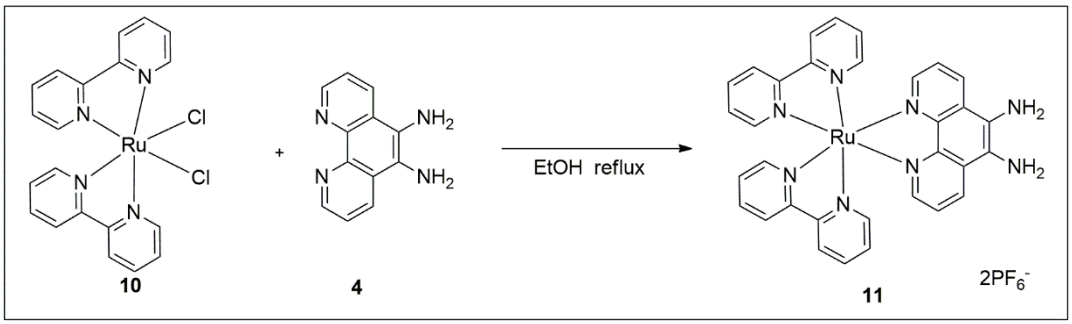

Figure 4.8: Synthesis of 11.

A mixture of bis(2,2'-bipyridine)dichlororuthenium(II) (**10**) (100 mg, 0.21 mmol) and 5,6-diamino phenanthroline (**4**) (44 mg, 0.21 mmol) was refluxed in EtOH-water (2:1, 13,5 mL) under argon gas overnight. Next, the mixture was cooled to the room temperature, half of the ethanol was distilled under vacuum distillation. The filtrate was added solid NH_4PF_6 (660mg, 4.05 mmol). Next, the product was washed with diethyl ether and water (0.1 g, 55% yield). The structural analyses of **11** have been achieved by using mass spectrometry and FT-IR spectroscopy.

Mass spectrum: MALDI-TOF (m/z) Calc. for $C_{32}H_{26}F_{12}N_8P_2Ru^{2-}$: 623.67, Found: 623$[M\text{-}2PF_6]^+$.

FT-IR ν_{max} (cm^{-1}): 3652, 3590, 1702, 1628, 1604, 1562, 1466, 1477, 1425, 1297, 1244, 1162, 877, 829 (P-F), 760, 729, 555.

4.2.2.3.Synthesis of 4,7-dichlorophenanthroline ruthenium(II) complex (12)

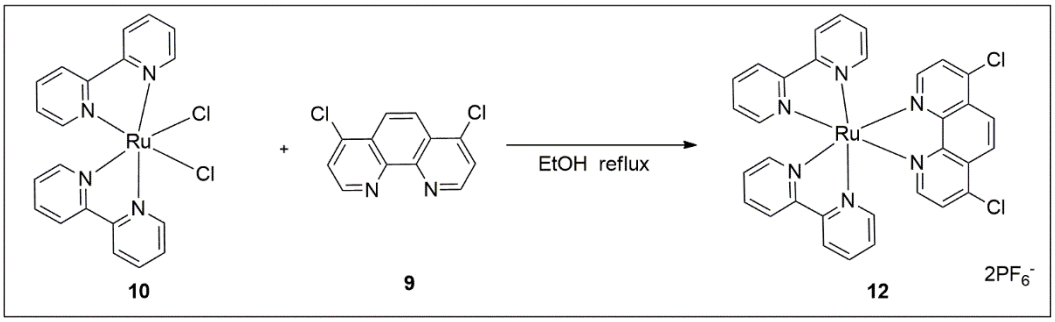

Figure 4.9: Synthesis of 12.

In ethanol/water solvent mixture (15 mL ethanol/7 mL water) 4,7-diclorophenanthroline (**9**) (0.05 g, 0.21 mmol) and ruthenium dichloro complex (**10**) (0.1 g, 0.21 mmol) was refluxed one night. After cooling the reaction, the solvent was removed and PF_6 salt of the complex was obtained with NH_4PF_6 (0.6 g, 3.68 mmol) addition. Then, the resulting solid was washed with diethyl ether after filtration. The final substance was used for further reactions without any purification techniques. The structural analyses of **12** have been achieved by using mass spectrometry and FT-IR spectroscopy.

Mass spectrum: MALDI-TOF (m/z) Calc. for $C_{32}H_{22}C_{l2}F_{12}N_6P_2Ru^{2-}$:952.5, Found: 662 $[M\text{-}2PF_6]^+$, 629 $[M\text{-}2PF_6\text{-}Cl]^+$.

FT-IR ν_{max} (cm^{-1}): 3325, 3123, 1606, 1560, 1469, 1446, 1412, 1395, 1336, 1316, 1245, 1219, 1085, 821 (P-F), 760, 730.

4.2.3. Synthesis of 4,7-dichloro-phenanthroline iridium(III) complex (14)

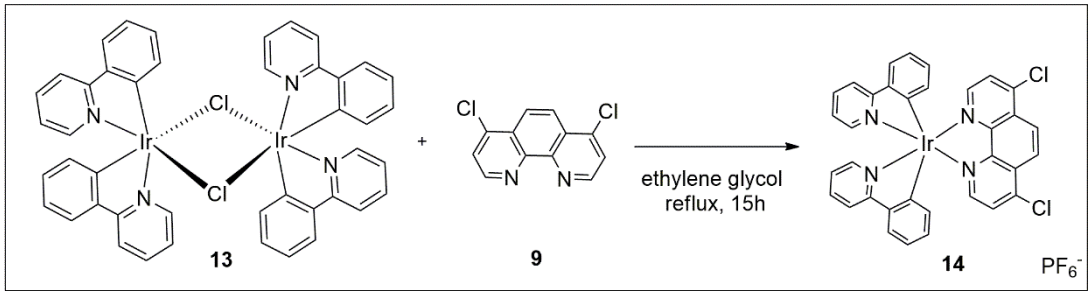

Figure 4.10: Synthesis of 14.

In ethylene glycol, 4,7-Dicloropheanthroline (**9**) (0.02 g, 0.1 mmol) and iridium dimer **13** [72] (0.05 g, 0.047 mmol) was stirred over 15 h. Then, the extraction was performed with water and hexane. Next, the half of the water was removed and PF_6 salt of the compound was isolated with addition of NH_4PF_6 (0.3 g, 1.8 mmol) to the flask. The final precipitate was filtrated and washed with diethyl ether. The structural analyses of **14** have been achieved by using mass spectrometry and FT-IR spectroscopy.

Mass spectrum: MALDI-TOF (m/z) Calc. for $C_{34}H_{22}Cl_2F_6IrN_4P^-$:894.6, Found: 749 $[M\text{-}PF_6]^+$.

FT-IR ν_{max} (cm^{-1}): 2932, 1607, 1583, 1566, 1516, 1478, 1439, 1418, 1395, 1345, 1310, 1269, 1229, 1165, 1130, 1087, 1064, 1032, 831 (P-F), 758, 556**.**

4.2.4. Synthesis of Perylene Derivatives

4.2.4.1. Synthesis of 1,6,7,12-tetrabromo-3,4:9,10-dianhydride (16)

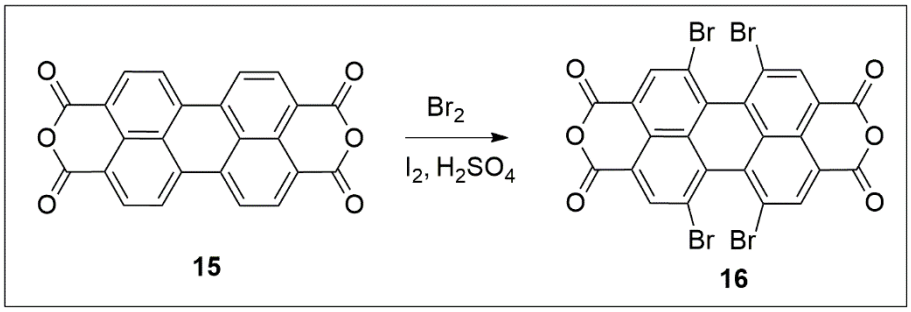

Figure 4.11: Synthesis of 16.

In a 250 mL flask, perylene **16** (5 g, 0.013 mol) was allowed to stir in 70 mL of H_2SO_4 (98 %) [73]. Then, the reaction mixture was heated to 65 ℃ and, 0.13 g (0.51 mmol) of I_2 was added, placing an water condenser, reaction heated to 85 ℃, 3 mL of Br_2 was added dropwise (1 drop every 5 second). The reaction was allowed to stir 19 h under argon atmosphere. Next, an additional 1.2 mL of Br_2 was added after heat was increased to 110 ℃, then, reaction was stirred 5 more days. After cooling to room temperature, argon gas was bubbled in to get rid of excess Br_2 from the reaction medium. Then the reaction mixture poured into 100 mL of ice-water, then after suction filtration, the red precipitates was collected. Since **16** is insoluble in organic solvents, there is no other analysis for the compound.

FT-IR ν_{max} (cm^{-1}): 1775, 1738, 1585, 1489, 1360, 1304, 1272, 1226, 1209, 1151, 1040, 1012, 964, 910, 857, 799, 733, 694, 645.

4.2.4.2.Synthesis of 1,6,7,12-tetrabromo-N,N'-(2,6-diisopropylphenyl)-perylene-3,4,9,10-bis(dicarboximide) (17)

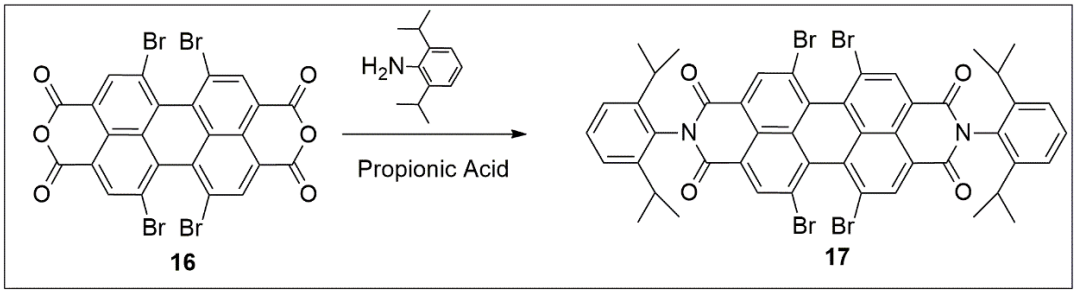

Figure 4.12: Synthesis of 17.

0.1 g (0.14 mmol) of **5** was heated to 140 ℃ in 5 mL propionic acid under argon atmosphere. Then, 0.2 mL 2,6-diisopropyl aniline was added to the reaction medium, and it was stirred overnight. After removing the propionic acid by vacuum, extraction was done with CH_2Cl_2 and 1 M NaOH solution. Purification on silica 4:1 Hexane/CH_2Cl_2 gave product **17** (0.13 g, %85 yield). The structural analyses of **17** have been achieved by using mass spectrometry and FT-IR spectroscopy [74].

Mass spectrum: MALDI-TOF (m/z) Calc. 1006, Found: 1007 $[M+H]^+$.

FT-IR ν_{max} (cm^{-1}): 2964, 2936, 2868, 1710 (C=O, imide), 1673, 1650, 1584, 1518, 1459, 1373, 1365, 1236.

4.2.4.3.Synthesis of 1,6,7,12-tetra(4-tert-butyl-phenoxy)-N,N'-bis-(2,6-diisopropylphenyl)-perylene-3,4:9,10-bis(dicarboximide) (18)

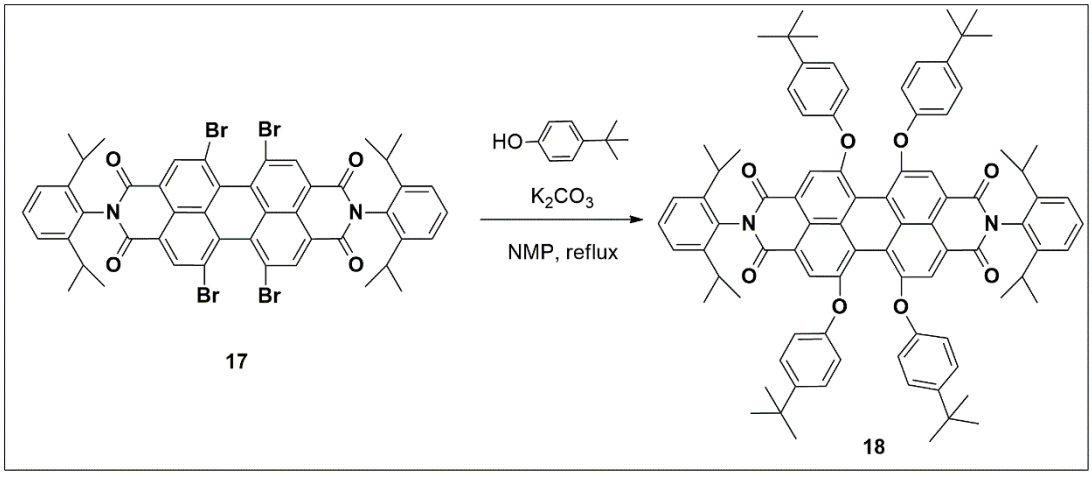

Figure 4.13: Synthesis of 18.

A mixture of **17** (0.13 g, 0.13 mmol), *p*-tert-butylphenol (0.16 g, 1.08 mmol) and 150 mg K_2CO_3 (0.15 g, 1.09 mmol) was stirred at 140 ℃ under argon atmosphere in NMP. After 8 h, it was cooled and poured into 8 % HCl (vol) solution, The precipitate was washed with water and purified on silica (3:1 Hexane/ CH_2Cl_2) (85 g, 50 % yield). The structural analyses of **18** have been achieved by using mass spectrometry, FT-IR spectroscopy, ^{1}H NMR and ^{13}C NMR spectroscopy and single X-ray crystallography [75].

Mass spectrum:) MALDI-TOF (m/z) Calc. 1303.7, Found: 1303 $[M+H]^+$.

FT-IR ν_{max} (cm^{-1}): 2962 (C-H, *t*-butyl), 2870, 1706 (C=O, imide), 1673 (C=O), 1585, 1504, 1406, 1339, 1280, 1206.

^{1}H-NMR (500 MHz, $CDCl_3$): δ 8.30 (s, 4H), 7.43 (t, *J* = 8.0 Hz, 2H), 7.27 (m, 12 H), 6.88 (d, *J* = 8.0 Hz, 8H), 2.72 (S, *J* = 6.5 Hz, 4H), 1.28 (s, 36 H), 1.13 (d, *J* = 6.5 Hz, 24H).

^{13}C NMR (500 MHz, CD_3COCD_3): δ 163.64, 156.20, 153.08, 17.63, 145.90, 133.52, 130.97, 129.68, 129.96, 124.16, 122.92, 121.05, 120.53, 120.46, 119.49, 34.65, 31.73, 29.99, 29.71, 24.70.

4.2.4.4.Synthesis of 1,6,7,12-tetra(4-tert-butyl-phenoxy) carboximide carboxyanhydride (19)

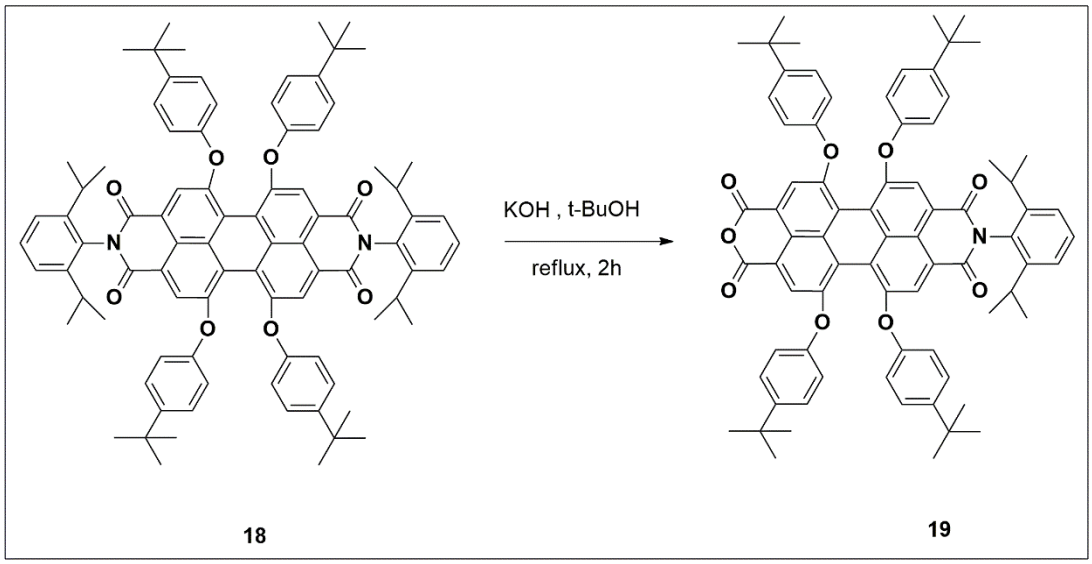

Figure 4.14: Synthesis of 19.

7 (0.16 g, 0.12 mmol) and KOH (0.064 g, 1.14 mmol) was heated to reflux in 40 mL of *t*-BuOH over 2 h. Then the reaction was poured into AcOH and 2 N HCl solution. The resulting product was washed with water after filtration (0.04 g, 30% yield). The structural analyses of **19** have been achieved by using mass spectrometry, FT-IR spectroscopy and ^{1}H NMR, ^{13}C NMR spectroscopy [76].

Mass spectrum:. MALDI-TOF (m/z) Calc. 1144, Found: 1145 $[M+H]^{+}$.

FT-IR ν_{max} (cm^{-1}): 2962, 2928, 2869, 1771 (C=O, anhydride), 1742, 1708, 1673, 1586, 1504, 1463, 1402, 1363, 1338, 1287, 1262, 1211, 1173, 1108, 1095, 1014, 884, 834, 799.

^{1}H-NMR (500 MHz, CD3COCD3): δ ppm 8.27 (s, 2H), 8.22 (s, 2H), 7.41 (t, J = 5.0 Hz, 1H), 7.25 (m, 10 H), 2.63 (S, J = 7.0 Hz, 2H), 1.30 (s, 18H), 1.27 (s, 18H), 1.09 (d, J = 7.0 Hz, 12 H).

^{13}C NMR (500 MHz, CD_3COCD_3): δ 163.45, 160.25, 156.76, 156.09, 152.82, 152.70, 148.02, 147.84, 145.79, 129.71, 127.07, 126.97, 126.92, 126.90, 124.11, 123.41, 122.40, 121.81, 120.19, 120.12, 119.52, 118.30, 115.78, 34.64, 31.65, 29.92, 29.29, 24.23, 14.34.

4.2.4.5.Synthesis of perylenediimide 20

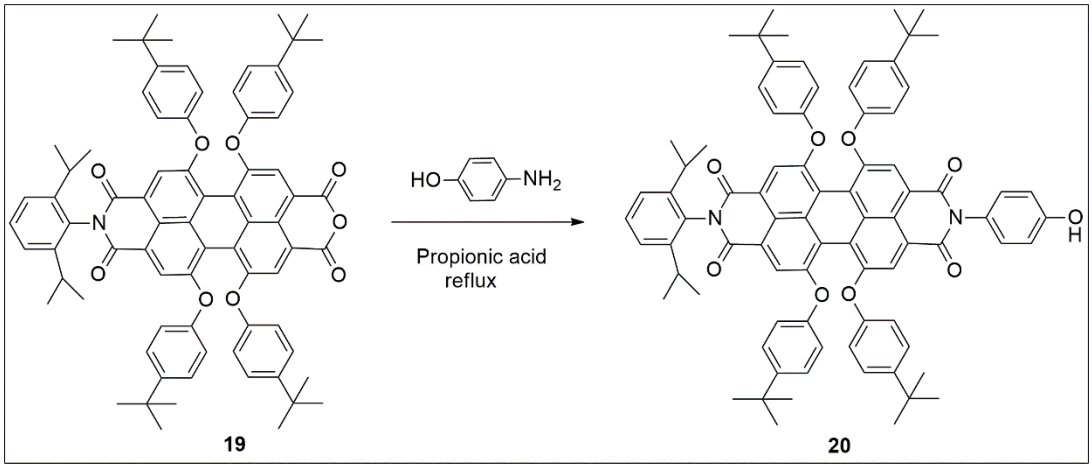

Figure 4.15: Synthesis of 20.

Perylene **20** (0.05 g, 0.05 mmol) and 4-aminophenol (0.01 mg, 0.1 mmol) were refluxed in propionic acid (5 mL) overnight. Next day, the mixture was poured into 1 M NaOH solution to neutralize, then, preparative thin layer chromatography was

applied to isolate compound **20** (0.03 g, 42% yield). The structural analyses of **20** have been achieved by using mass spectrometry, FT-IR spectroscopy and ^{1}H NMR, ^{13}C NMR spectroscopy.

Mass spectrum: MALDI-TOF (m/z) Calc. for $C_{82}H_{78}N_2O_9$: 1235 Found: 1235 $[M]^+$.

FT-IR ν_{max} (cm^{-1}): 3406 (O-H), 2962, 2930, 2869,1705 (C=O, imide), 1672, 1585, 1504, 1407, 1341, 1283, 1220, 1173, 882, 832.

^{1}H-NMR (500 MHz, $CDCl_3$): δ ppm 8.28 (s, 2H), 8.23 (s, 2H), 7.41(t, *J* = 8.0 Hz, 2H), 7.25-7.21 (m, 10H), 7.08 (d, *J* = 8.5 Hz, 2H), 6.88 (t, *J* = 10 Hz, 5H), 6.83 (d, *J* = 8.5 Hz, 4H), 5.13 (s, 1H, OH), 2.70 (S, *J* = 7.0 Hz, 2H), 1.26 (d, *J* = 4.0 Hz, 36 H), 1.11 (d, *J* = 7.0 Hz, 12H).

^{13}C NMR (500 MHz, $CDCl_3$): δ 164.05, 163.58, 156.24, 156.21, 155.92, 153.08, 152.96, 147.64, 147.56, 145.83, 133.39, 130.9, 129.85, 129.61, 127.97, 126.89, 124.09, 122.93, 122.75, 121.08, 120.88, 120.50, 120.36, 120.03, 119.55, 119.41, 116.42, 34.58, 31.64, 29.92, 29.29, 24.23.

4.2.5. Synthesis of 3,5-distryl BODIPY (22)

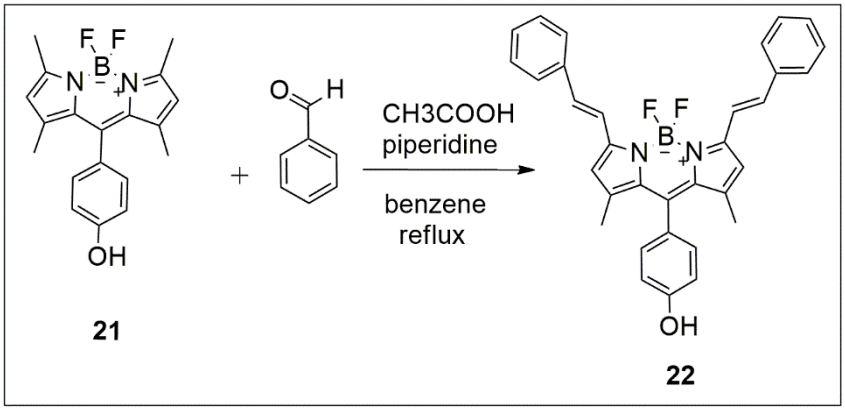

Figure 4.16: Synthesis of 22.

21 [77] (0.13 g, 0.38 mmol) and benzaldehyde (0.11 g, 1.07 mmol) were stirred in benzene (40 mL). Acetic acid (400 µL) and piperidine (400 µL) were added to the flask. The reaction was then refluxed with Dean-Stark apparatus. The final crude product was isolated by extraction with CH_2Cl_2 and water. Na_2SO_4 was used to dry the organic layer. Applying column chromatography, the crude product was obtained

with CH_2Cl_2 mobile phase. Fraction of **22** was collected then the solvent was removed under reduced pressure (0.12 g, 61% yield). The structural analyses of **22** have been achieved by using mass spectrometry, FT-IR spectroscopy and ^{1}H NMR, ^{13}C NMR spectroscopy.

Mass spectrum: MALDI-TOF (m/z) Calc. for $C_{33}H_{27}BF_2N_2O$: 516.22 Found: 516 $[M]^+$.

FT-IR ν_{max} (cm^{-1}): 3463 (O-H), 3061, 3033, 962, 2924, 1622, 1609, 1577, 1531, 1480, 1444, 1417, 1382, 1365, 1301, 1268, 1198, 1158, 1116, 1082, 987, 948, 898, 832, 813, 749, 693.

^{1}H-NMR (CD_3COCD_3): δ ppm 7.75 (d, *J* = 16.41 Hz, trans, 2H), 7.67 (d, *J* = 7.55 Hz, 4H), 7.53 (d, *J* = 16.40 Hz, trans, 2H), 7.47 (t, *J* = 7.52 Hz, 4H), 7.38 (t, *J* = 7.31 Hz, 2H), 7.26 (d, *J* = 8.24 Hz, 2H), 7.08 (d, *J* = 8.25 Hz, 2H), 6.89 (s, 2H), 1.58 (s, 6H).

^{13}C NMR (CD_3COCD_3): δ 159.46, 153.30, 143.46, 141.50, 137.70, 137.18, 134.70, 130.64, 130.03, 129.98, 128.19, 126.53, 119.93, 118.90, 117.07, 15.08.

4.2.5.1.Synthesis of bis(perylenediimide) ruthenium(II) complex (23)

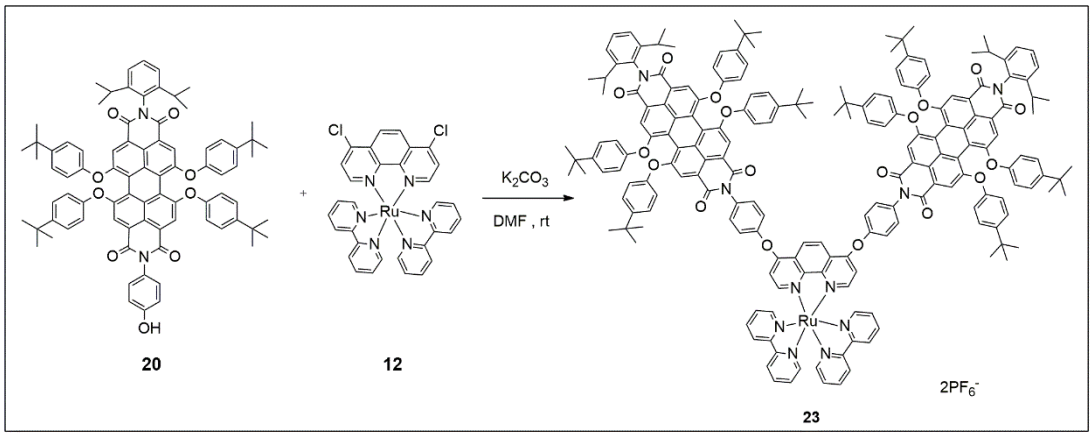

Figure 4.17: Synthesis of 23.

A mixture of ruthenium perylenediimide **20** (0.08 g, 0.06 mmol) and K_2CO_3 (8.2 mg, 0.06 mmol) and (II) dichloro complex (**12**) (0.02 g, 0.03 mmol) was stirred under Ar at room temperature in DMF for 72. Next, the mixture was extracted with H_2O/CH_2Cl_2. Chromatography on silica gel (CH_2Cl_2 → CH_2Cl_2 /EtOH (50/1) yielded dark purple solid (0.06 g, 60% yield). The structural analyses of **23** have been

achieved by using mass spectrometry, FT-IR spectroscopy and ^{1}H NMR, ^{13}C NMR spectroscopy.

Mass spectrum: MALDI-TOF (m/z) Calc. for $C_{196}H_{176}F_{12}N_{10}O_{18}P_2Ru^{2-}$: 3350.6 Found: 3060 $[M\text{-}2PF_6]^+$ and 3204 $[M\text{-}PF_6]^+$.

FT-IR ν_{max} (cm^{-1}): 3067, 2962 (C-H, *t*-butyl), 2906, 2869, 1705 (C=O, imide), 1671, 1585, 1501, 1466, 1405, 1363, 1339, 1281, 1206, 1173, 1110, 1014, 834, 761, 729.

^{1}H-NMR ($CDCl_3$): δ ppm 8.61 (s, 2H), 8.30-8.27 (m, 8H), 8.24 (s, 4H), 7.93-7.91 (m, 4H), 7.86-7.83 (m, 4H), 7.59 (d, J = 6.0 Hz, 2H), 7.47-7.38 (m, 14 H), 7.25-7.20 (m, 21H), 6.99 (d, J = 6.0 Hz, 2H), 6.86-6.82 (m, 16 H), 2.7 (septet, J = 6.5 Hz, 4H), 1.26 (s, 72 H), 1.11 (d, J = 6.5 Hz, 24H).

^{13}C NMR ($CDCl_3$): δ 181.37, 180.87, 163.61, 163.56, 163.49, 162.62, 157.40, 156.40, 156.34, 156.12, 153.07, 152.88, 152.67, 152.57, 148.18, 147.59, 145.82, 137.83, 137.56, 137.48, 133.92, 133.41, 133.38, 131.51, 130.88, 129.70, 129.62, 129.19, 128.77, 128.08, 127.10, 126.88, 126.70, 126.65, 124.09, 123.87, 123.68, 123.59, 123.42, 123.00, 122.38, 122.27, 122.16, 122.09, 121.38, 120.73, 120.63, 120.55, 120.34, 120.30, 120.05, 119.63, 119.49, 119.46, 119.33, 119.28, 116.87, 110.36, 34.72, 34.58, 34.44, 33.40, 32.14, 31.84, 31.78, 31.65, 31.50, 29.92, 29.67, 29.58, 29.50, 29.46, 29.39, 29.30, 24.97, 24.24, 22.91.

4.2.5.2.Synthesis of bis(perylenediimide) iridium(III) complex (24)

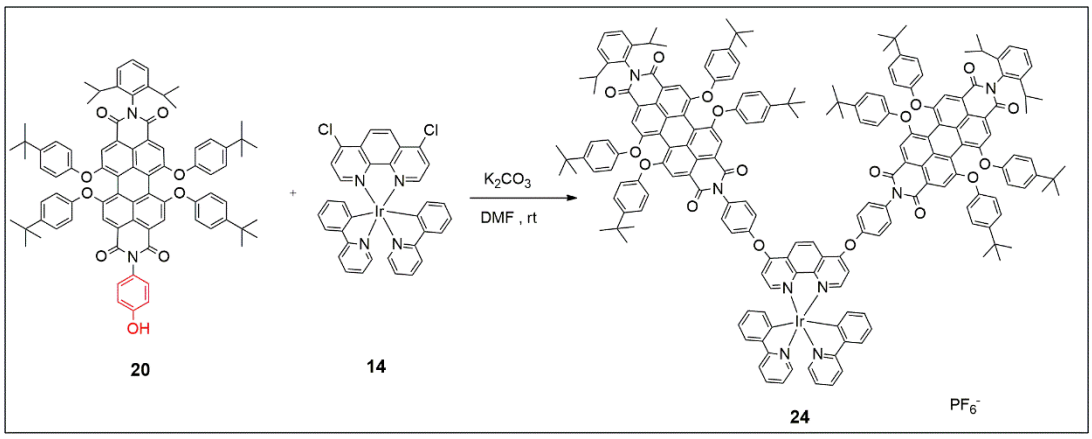

Figure 4.18: Synthesis of 24.

A mixture of perylenediimide **20** (0.08 g, 0.07 mmol), iridium (II) complex (**14**) (0.03 g, 0.03 mmol) and K_2CO_3 (15 mg, 0.11 mmol) was stirred under Ar at room temperature in DMF for 72. After extraction with H_2O/CH_2Cl_2, chromatography on silica gel (CH_2Cl_2 → CH_2Cl_2 /EtOH (50/1) yielded dark purple solid (0.05 g, 47% yield). The structural analyses of **24** have been achieved by using mass spectrometry, FT-IR spectroscopy and ^{1}H NMR, ^{13}C NMR spectroscopy.

Mass spectrum: MALDI-TOF (m/z) Calc. for $C_{198}H_{176}F_6IrN_8O_{18}P^-$: 3292.7 Found: 3147 $[M\text{-}PF_6]^+$.

FT-IR ν_{max} (cm^{-1}): 2958, 2925, 2856, 1703 (C=O), 1668, 1609, 1584, 1552, 1499, 1413, 1364, 1341, 1364, 1288, 1212, 837, 738.

^{1}H-NMR ($CDCl_3$): δ ppm 8.62 (s, 2H), 8.28 (s, 4H), 8.25 (s, 4H), 7.90 (d, J = 6.0 Hz, 2H), 7.82 (d, J = 8.0 Hz, 2H), 7.66 (t, J = 7.5 Hz, 4H), 7.61 (d, J = 7.5 Hz, 2H), 7.55 (d, J = 5.5 Hz, 2H), 7.41 (m, 12 H), 7.24 (m, 20H), 7.0 (t, J = 6.0 Hz, 2H), 6.96 (t, J = 7.5 Hz, 4H), 6.86 (m, 16H), 2.70 (S, J = 2.0 Hz, 4H), 1.27 (s, 72H), 1.11 (d, J = 1.5 Hz, 24H).

^{13}C NMR ($CDCl_3$): δ 167.86, 163.75, 163.65, 163.55, 156.34, 156.17, 153.07, 152.91, 151.88, 150.13, 149.41, 149.30, 148.11, 147.67, 147.61, 145.82, 144.03, 138.03, 133.95, 133.43, 133.38, 132.25, 132.21, 132.10, 131.46, 131.42, 130.92, 130.88, 130.77, 129.62, 126.91, 124.74, 124.22, 124.09, 123.74, 123.03, 122.68, 122.45, 122.14, 121.36, 120.75, 120.56, 120.36, 120.31, 120.08, 119.52, 119.44, 119.40, 109.52, 34.59, 31.65, 29.91, 29.29, 24.22.

4.2.6. Synthesis of Ruthenium and Iridium BODIPY Metal Complexes

4.2.6.1.Synthesis of BODIPY ruthenium(II) complex (25)

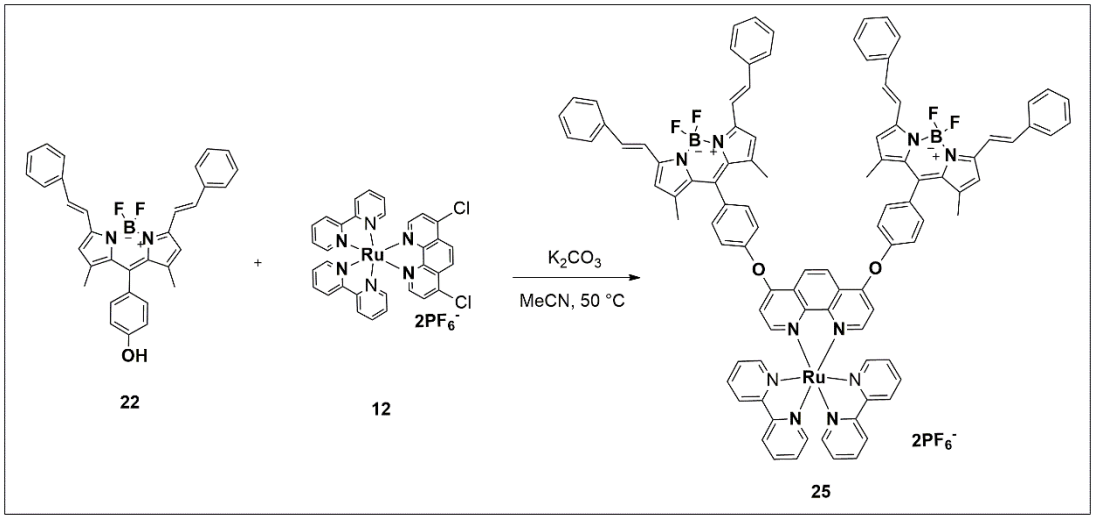

Figure 4.19: Synthesis of 25.

A mixture of **22** (0.05 g, 0.097 mmol), **12** (0.05 g, 0.048 mmol) and K_2CO_3 (13.2 mg, 0.097 mmol) was heated to 50℃ in MeCN under argon gas. The solvent was removed using rotary evaporation after 36 h then column chromatography with silica gel (CH_2Cl_2 → CH_2Cl_2 /EtOH (25/1) yielded **25** (0.08 g, 45% yield). The structural analyses of **25** have been achieved by using mass spectrometry, FT-IR spectroscopy and ^{1}H NMR, ^{13}C NMR spectroscopy.

Mass spectrum: MALDI-TOF (m/z) Calc. for $C_{98}H_{74}B_2F_{16}N_{10}O_2P_2Ru^{2-}$: 1912.3 Found: 1622 $[M\text{-}2PF_6]^+$.

FT-IR ν_{max} (cm^{-1}): 3706, 3059, 2965, 2920, 2850, 1706, 1615, 1583, 1576, 1539, 1488, 1464, 1446, 1408, 1370, 1311, 1300, 1284, 1229, 1202, 1178, 1163, 1112, 1081, 1056, 1016, 991, 958, 919, 875, 841, 821, 763, 732, 695.

^{1}H-NMR (CD3COCD3): δ ppm 8.83 (m, 6H), 8.31 (d, *J* = 6.14 Hz, 2H), 8.23 (t, *J* = 8.53 Hz, 2H), 8.19 (t, *J* = 8.51 Hz, 2H), 8.16 (d, *J* = 5.29 Hz, 2H), 8.11 (d, *J* = 5.65 Hz, 2H), 7.76 (m, 10H), 7.68 (m, 14H), 7.60 (m, 2H), 7.58 (d, trans, *J* = 16.57 Hz, 4H), 7.49 (t, *J* = 7.46 Hz, 10H), 7.41 (t, *J* = 7.42 Hz, 2H), 7.23 (d, *J* = 6.06 Hz, 2H), 6.95 (s, 4H), 1.60 (s, 12H).

^{13}C NMR (CD_3COCD_3): δ 174.74, 163.11, 158.74, 158.36, 155.07, 154.99, 153.83, 153.15, 153.01, 138. 80, 137.82, 137.55, 132.45, 130.32, 130.28, 130.13, 130.12, 130.05, 128.69, 128.27, 125.29, 124.89, 123.06, 122.79, 119.32, 110.86., 15.26, 14.42.

4.2.6.2.Synthesis of BODIPY iridium(III) complex (26)

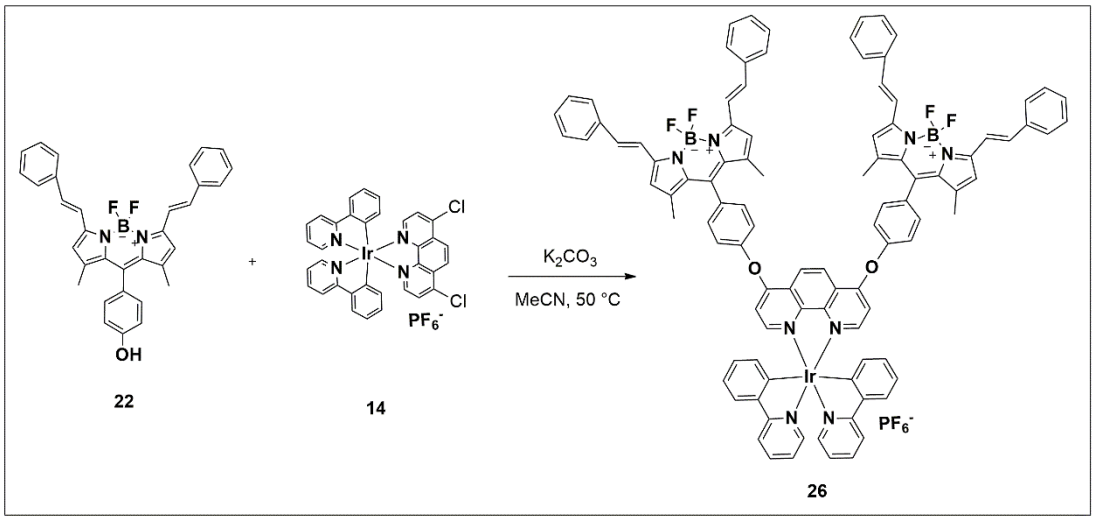

Figure 4.20: Synthesis of 26.

A mixture of **14** (0.04 g, 0.048 mmol), **22** (0.05 g, 0.097 mmol) and K_2CO_3 (14.0 mg, 0.01 mmol) was heated to 50℃ in MeCN under argon gas. The solvent was removed using rotary evaporation after 36 h. Then, column chromatography on silica gel (CH_2Cl_2 /EtOH (200/1→ CH_2Cl_2 /EtOH (50/1) yielded **26** (0.02 g, 20% yield). The structural analyses of **26** have been achieved by using mass spectrometry, FT-IR spectroscopy and ^{1}H NMR, ^{13}C NMR spectroscopy.

Mass spectrum: MALDI-TOF (m/z) Calc. for $C_{100}H_{74}B_2F_{10}IrN_8O_2P^-$: 1854.5 Found: 1709 $[M\text{-}PF_6]^+$.

FT-IR ν_{max} (cm^{-1}): 3060, 2959, 2924, 2853, 1710, 1608, 1583, 1539, 1490, 1462, 1447, 1410, 1387, 1369, 1301, 1281, 1263, 1229, 1203, 1164, 1111, 1080, 1063, 1016, 992, 960, 918, 843, 761, 730, 696.

^{1}H-NMR (CD3COCD3): δ ppm 8.83 (s, 2H), 8.30 (d, J = 6.0 Hz, 2H), 8.24 (d, J = 7.10 Hz, 2H), 7.93 (m, 4H), 7.86 (d, J = 5.5 Hz, 2H), 7.75 (m, 8H), 7.69 (m, 12H),

7.57 (d, J = 16.37, trans, 4H), 7.48 (t, J = 7.56 Hz, 8H), 7.40 (t, J = 7.33 Hz, 4H), 7.36 (d, J = 6.0 Hz, 2H), 7.06 (m, 4H), 6.93 (m, 6H), 6.42 (d, J = 7.50 Hz, 2H), 1.62 (s, 12).

^{13}C NMR (CD_3COCD_3): δ 168.95, 163.88, 154.89, 154.04, 153.82, 151.04, 150.35, 149.19, 145.32, 143.23, 139.51, 137.79, 137.57, 134.51, 134.18, 132.76, 132.44, 131.25, 130.26, 130.04, 128.27, 125.85, 125.15, 124.40, 123.37, 123.19, 122.79, 120.78, 120.70, 119.73, 119.32, 110.94, 15.31.

4.2.7. Synthesis of benzimidazole-fused perylene ruthenium(II) complex (27)

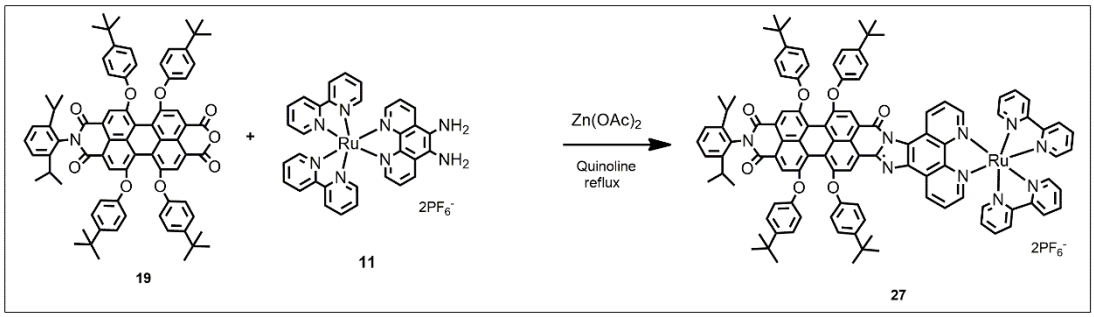

Figure 4.21: Synthesis of 27.

A mixture of **11** (0.11 g, 0.096 mmol) and **19** (0.03 g, 0.048 mmol) was refluxed in quinoline using presence of $Zn(OAc)_2$ under argon gas for 24 h. After cooling, the reaction was poured into 5 % HCl solution. The extraction of the resulting mixture was done with CH_2Cl_2, then chromatography on silica gel using CH_2Cl_2 yielded **27** as dark red solid (0.02 g, 15% yield). The structural analyses of **27** have been achieved by using mass spectrometry, FT-IR spectroscopy and ^{1}H NMR, ^{13}C NMR spectroscopy.

Mass spectrum: MALDI-TOF (m/z) Calc. for $C_{108}H_{95}F_{12}N_9O_7P_2Ru^{2-}$: 2021.97 Found: 1732 $[M\text{-}2PF_6]^+$.

FT-IR ν_{max} (cm^{-1}): 3055, 2964 (C-H, *t*-butyl), 2932, 2871, 1699 (C=O, imide), 1665, 1587, 1503, 1398, 1364, 1328, 1283, 1265, 1216, 1173, 884, 833, 735, 703.

^{1}H-NMR ($CDCl_3$): δ ppm 9.03(m, 2H), 8.40 (m, 5H), 8.02 (s, 1H), 7.88 (d, *J* = 8.5 Hz, 1H), 7.77 (t, *J* = 8.0 Hz, 1H), 7.72 (m, 1H), 7.61 (t, *J* = 7.5 Hz, 1H), 7.49 (m, 1H), 7.42 (t, *J* = 8.0 Hz, 2H), 7.25-7.21 (m, 14H), 7.08 (d, *J* = 8.5 Hz, 2H), 6.88 (t, *J*

= 10 Hz, 5H), 6.83 (d, *J* = 8.5 Hz, 4H), 2.70 (septet, *J* = 7.0 Hz, 2H), 1.26 (d, *J* = 4.0 Hz, 36 H), 1.11 (d, *J* = 7.0 Hz, 12H).

^{13}C NMR ($CDCl_3$): δ 163.84, 156.11, 154.97, 154.57, 154.40, 154.78, 153.70, 153.60, 153.55, 153.36, 147.0, 146.83, 146.73, 145.91, 134.89, 133.86, 133.0, 131.23, 129.75, 129.43, 128.64, 128.54, 126.69, 126.67, 126.59, 126.47, 124.01, 123.23, 122.81, 121.95, 121.74, 120.98, 120.61, 120.56, 119.47, 119.33, 119.22, 119.07, 118.41, 114.95, 52.93, 45.71, 34.51, 32.15, 31.67, 29.9, 29.88, 29.58, 29.22, 24.22, 22.91, 14.33, 8.80, 8.36, 7.97.

4.3. Singlet Oxygen Measurements

Singlet oxygen quantum yields (ΦΔ) were calculated according to the literature [78]. The relative quantum yields were calculated with reference to Methylene Blue (MB) in DMSO as 0.52 [79]. Air saturated DMSO was obtained by bubbling air for 30 minutes. The absorbance of DPBF was adjusted around 1.0-1.1 in air saturated DMSO. Then, the sample was added to cuvette and sample's absorbance was adjusted around 0.1-0.2. After, taking some measurements in dark, we exposed the cuvette to red LED (λ= 632 nm, 2.5 mW /cm^2) at the peak absorption wavelength for a certain time for compounds. Absorbance was measured for several times after each irradiation. Then, slope of absorbance maxima of DPBF at 414 nm versus time graph for each sample was calculated. Singlet oxygen quantum yield was calculated according to the equation:

$$\Phi\Delta\,(\text{samp}) = \Phi\Delta\,(\text{ref}) \times [m\,(\text{samp})/m(\text{ref})]\times[F(\text{ref})/F(\text{samp})] \quad (4.1)$$

"m" is the slope of difference in change in absorbance of DPBF (414 nm) with the irradiation time, "F" is the absorption correction factor, which is given by

$$F = 1 - 10^{-OD}\ (\text{OD at the irradiation wavelength}) \quad (4.2)$$

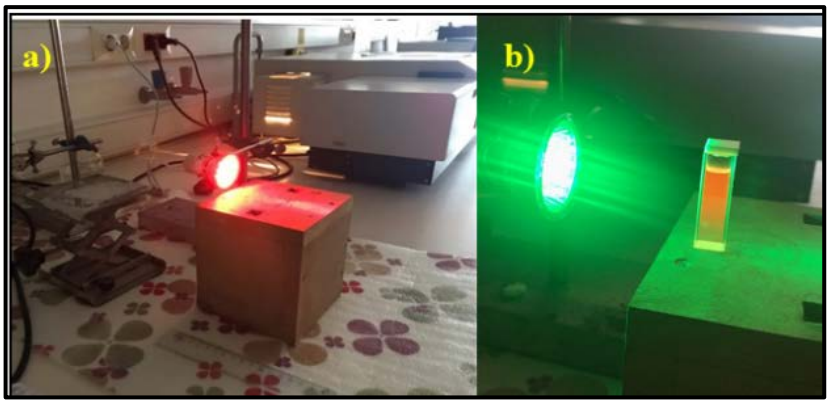

Figure 4.22: Set-up of the singlet oxygen measurement,
b) Uv cuvette during the red light treatment.

4.4. X-ray crystallography

Intensity data were recorded on a Bruker APEX II QUAZAR diffractometer. Absorption correction by multi-scan has been applied [80] and space groups were determined using XPREP implemented in APEX2 [81]. Structures were determined using the direct methods procedure in SHELXS-97 and refined by full-matrix least squares on F2 using SHELXL-97 [82]. All non-hydrogen atoms were refined with anisotropic displacement factors and C-H hydrogen atoms were placed in calculated positions and allowed to ride on the parent atom. The final geometrical calculations and the molecular drawings were carried out with PLATON [83], MERCURY [84] and DIAMOND (Version 3.1) [85] programs.

Figure 4.23: X-ray instrument.

4.5. *In vitro* PDT Studies

4.5.1. Cell lines and cell culture

In this study, human chronic myeloid leukemia, K562 cell line and cervical cancer cell line (HeLa)were used for photodynamic therapy studies (Figure 4.24). Cells were maintained in RPMI 1640 medium (Biochrom AG, Germany) in the presence of 10% FBS (v/v; Biochrom AG, Germany) and 1% gentamycin (v/v; Biological Industries, Israel) at 37^0C and 5% CO_2.

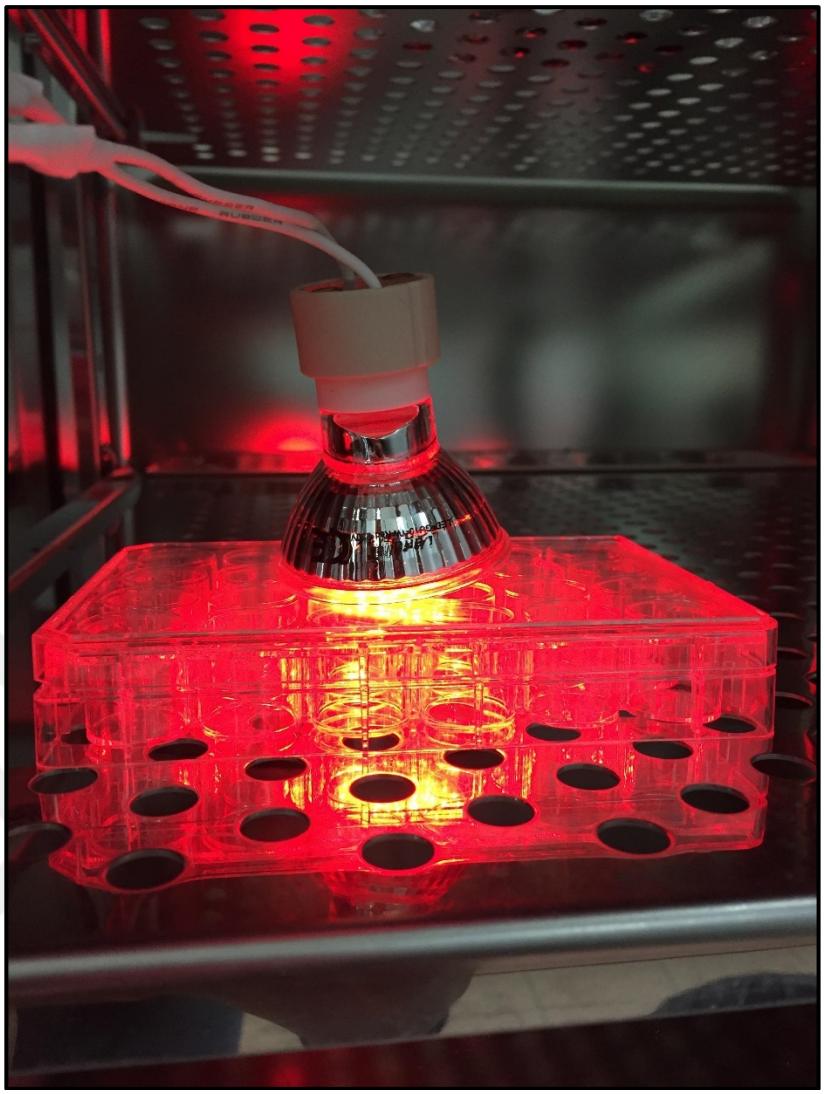

Figure 4.24: Set up of *in vitro* PDT studies.

4.5.2. Cell viability assay

In the first part of the study, we studied with bis(perylenediimide) ruthenium(II) complex (**23**). Cell viabilities were analysed by 3-(4,5-dimethylthiazol-2-yl)-2,5 diphenyltetrazolium bromide (MTT) assay. $30x10^3$ cells were seeded into two different 96-well plates and incubated for 24h. Next, cells were treated DMSO to check the solvent effect and increasing concentration of Ru-BP (0.3125-20 µM). One of the plates was incubated in dark while the other was incubated under red LED for 5 hours. Then, 10 µl of MTT solution (5mg/mL) was added onto cells and incubated for 4h. Finally, cells were disrupted with SDS-HCl solution (1g SDS in 0.01M HCI in 10 mL final volume) overnight and the microplates were read by microplate

spectrophotometer (Multiskan GO, Thermo Fisher Scientific, USA) at a wavelength of 570 nm. Optical densities were converted to % viability by using untreated cells as 100% and all the treatments were correlated to untreated group. Data were analysed by GraphPad Prism 7.0 software (GraphPadInc, USA). The results were considered significant at the level of 0.05.

In the second part of the study we studied with BODIPY ruthenium(II) complex (**25**) and BODIPY iridium(III) complex (**26**). Cell viabilities were determined by MTT assay. For HeLa cells, 30 x 10^3 cells were seeded into two different 96-well plates and incubated for 48 h. Then, cell were washed with PBS twice and treated with DMSO, **23**, and increasing concentrations (1.5–25.0 μM) of **25** and **26** for 5h in the dark or under red light. Appropriate medium controls were added to the experiments. For K562 cells, cells were pelleted and pellets were washed with PBS twice. Then, cells were counted in PBS and 50 x 10^3 cells were pelleted and resuspended in the medium containing related treatment of DMSO, **22** and increasing concentrations (1.5–25.0 μM) of **25** and **26**. Next, cells were seeded into two different 96-well plate and incubated in the dark or under red light for 5h. After 5h, 10.0 μL of MTT solution (5 mg/mL) was added onto cells and incubated for 4h. Cells were disrupted with SDS-HCl solution (1.0 g SDS in 0.01 M HCI in 10.0 mL final volume) overnight and the microplates were read using a microplate spectrophotometer (Multiskan GO, Thermo Fisher Scientific, USA) at 570 nm. Optical densities were converted to % viability by considering untreated cells to have 100% viability and all the treatments were correlated with the untreated group.

4.5.3. Trypan Blue staining

To further demonstrate the cell death, 480x10^3 cells were treated into two different 6-well plates. One of the plates was incubated in dark while the other was treated red light for 5 h. Next, cells were incubated with Trypan Blue (10%) for 5 min and washed by PBS twice. Next, cells were imaged under a light microscope.

4.5.4. Statistical analysis

All biological experiments were performed as three replica each of which including four technical replica. Data were analyzed by Two-way ANOVA by GraphPad Prism 8.0 software (GraphPadInc, USA). The results were considered significant at the level of 0.05.

5. RESULTS AND DISCUSSION

Among the thesis study, syntheses of perylene (**23**, **24** and **27**) and BODIPY (**25**, **26**) bearing ruthenium and iridium metal complexes have been accomplished. The chemical characterizations of the compounds have been performed by mass spectrometry, FT-IR and NMR spectroscopies. The photophysical studies of all the compounds have been carried out by UV-Vis absorption and fluorescence emission spectroscopies. *In vitro* PDT studies of the metal complexes (**23**, **25** and **26**) have been completed using human cancer cell lines like, K562 or HeLa.

5.1. Synthesis and Characterization

5.1.1. Synthesis and characterization of phenanthrolines

5.1.1.1. Synthesis and characterization of 5-nitro-1,10-phenanthroline (2).

In the first step, syntheses of phenanthroline starting compounds were carried out. In order to synthesize 5-nitro-1,10-phenanthroline (**2**), we used commercially available 1,10-phenanthroline in the presence of H_2SO_4/HNO_3 mixture [68]. Nitration reaction at 100 °C yielded the compound **2** (Figure 5.1).

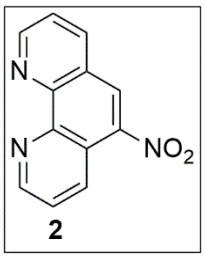

Figure 5.1: Molecular structure of 2.

In the mass spectrum of the compound **2**, molecular ion peak was observed at 225.16 that represent $[M]^+$ (Figure 5.2). Also, in the FT-IR spectrum, NO_2 stretches at 1505, 1517 and 1353 cm^{-1} supports the structure of **2** (Figure 5.3).

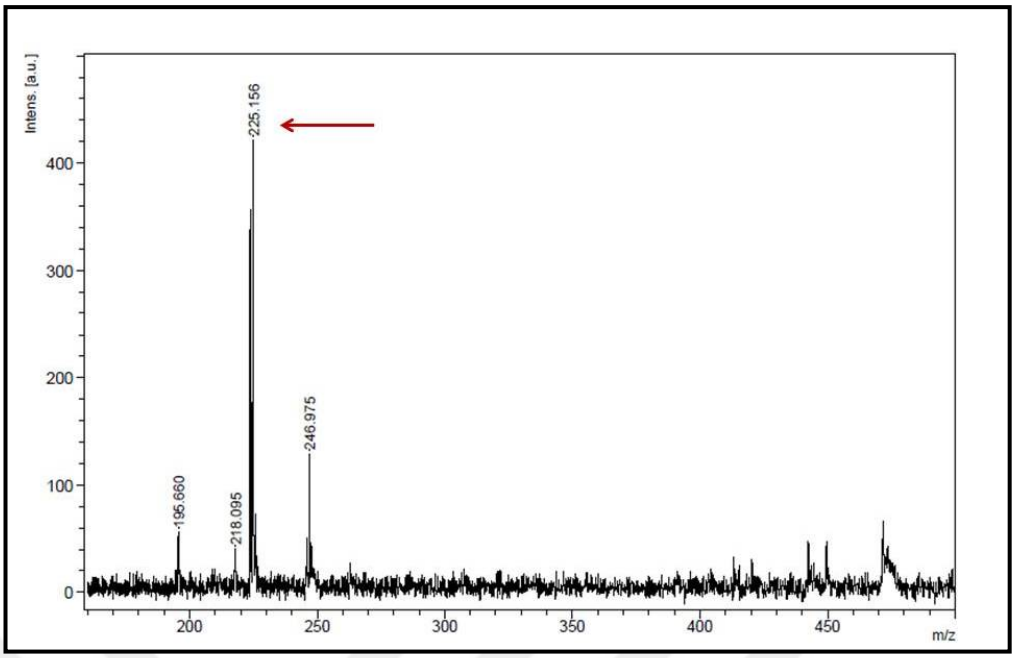

Figure 5.2: Mass spectrum of 2.

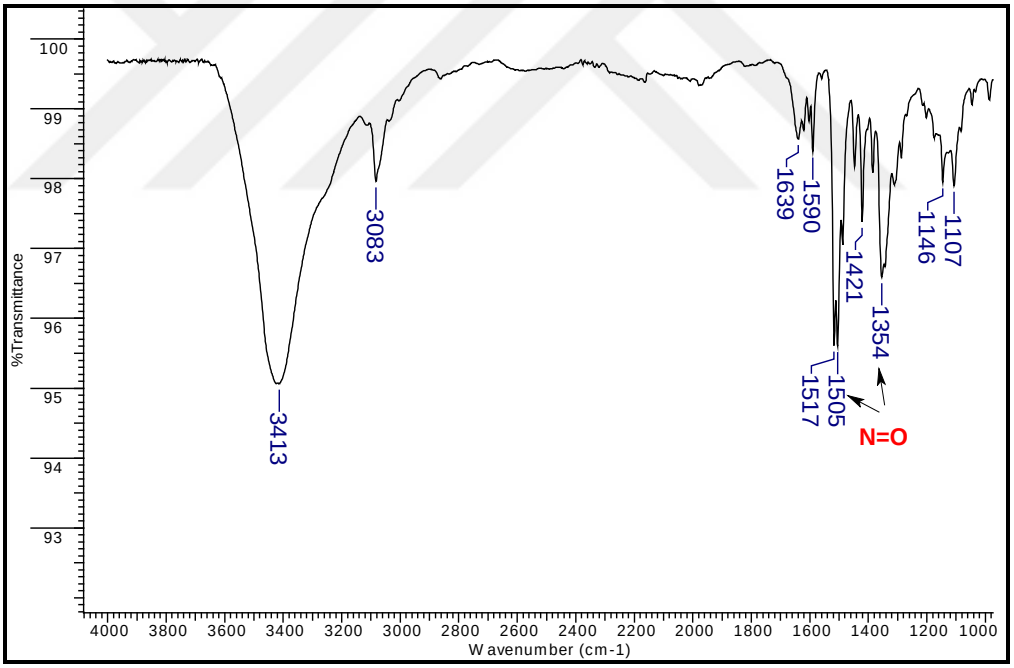

Figure 5.3: FT-IR spectrum of 2.

5.1.1.2.Synthesis and characterization of 5-nitro-6-amino-1,10-phenanthroline (3).

The synthesis of 5-nitro-6-amino-1,10-phenanthroline (**3**) performed with compound **2** and hydroxylamine hydrochloride in EtOH (Figure 5.4) [68].

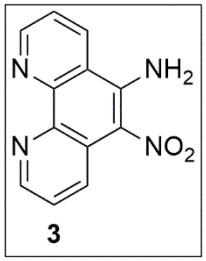

Figure 5.4: Molecular structure of 3.

In the mass spectrum, molecular ion peak at 240.94 belongs to $[M]^+$ supports the structure of **3** (Figure 5.5). In the FT-IR spectrum of **3**, N-H stretch of the amino group comes at 3266 cm^{-1} (Figure 5.6).

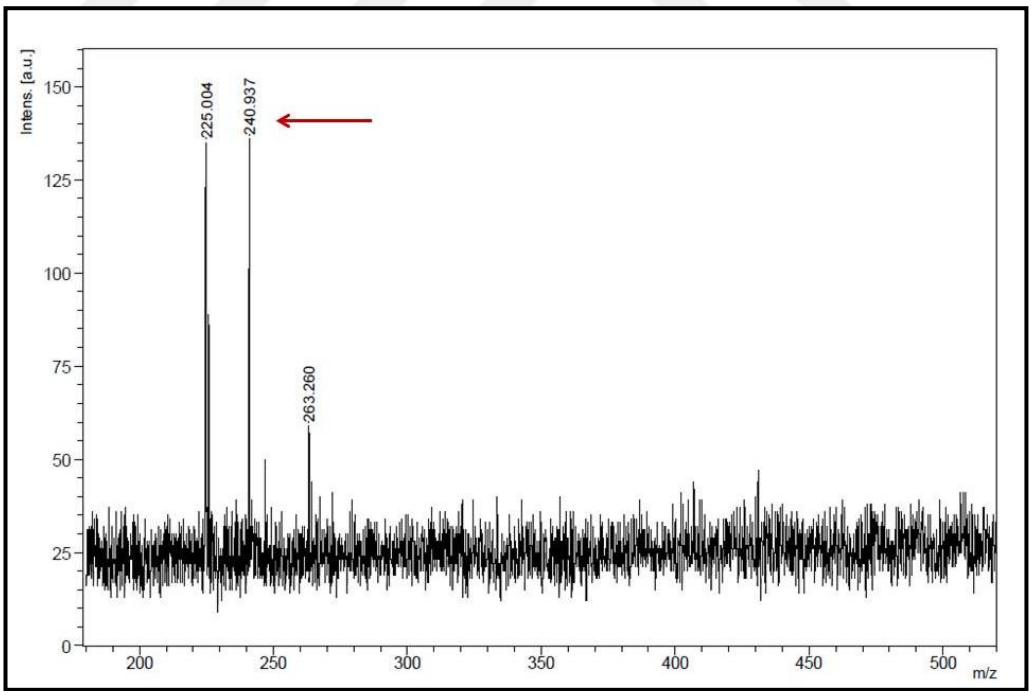

Figure 5.5: Mass spectrum of 3.

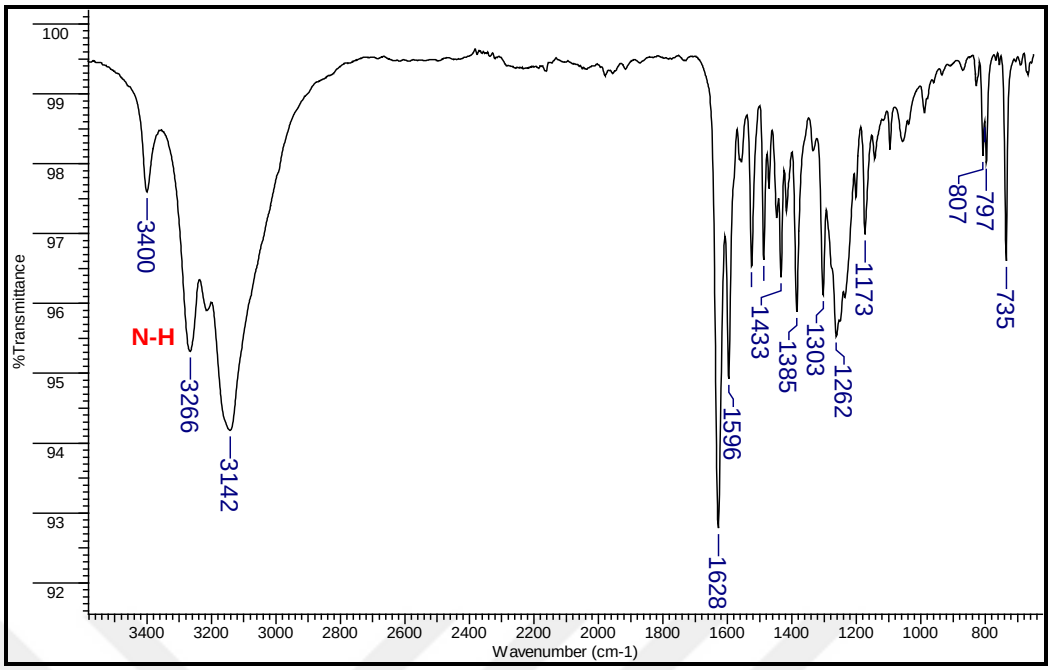

Figure 5.6: The FT-IR spectrum of 3.

5.1.1.3.Synthesis and characterization of 1,10-Phenanthroline-5,6-diamine (4)

1,10-Phenanthroline-5,6-diamine (**4**) was synthesized according to the literature method [68]. Nitration of **3** was carried out in the presence of hydrazine hydrate and Pd catalyst in EtOH (Figure 5.7).

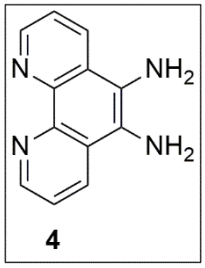

Figure 5.7: Molecular structure of 4.

The mass spectrum of the compound supports the molecular ion peak that comes at 210.16 (Figure 5.8). Also, in Figure 5.9, N-H stretch of the two amino groups can be shown easily at around 3300 cm^{-1}.

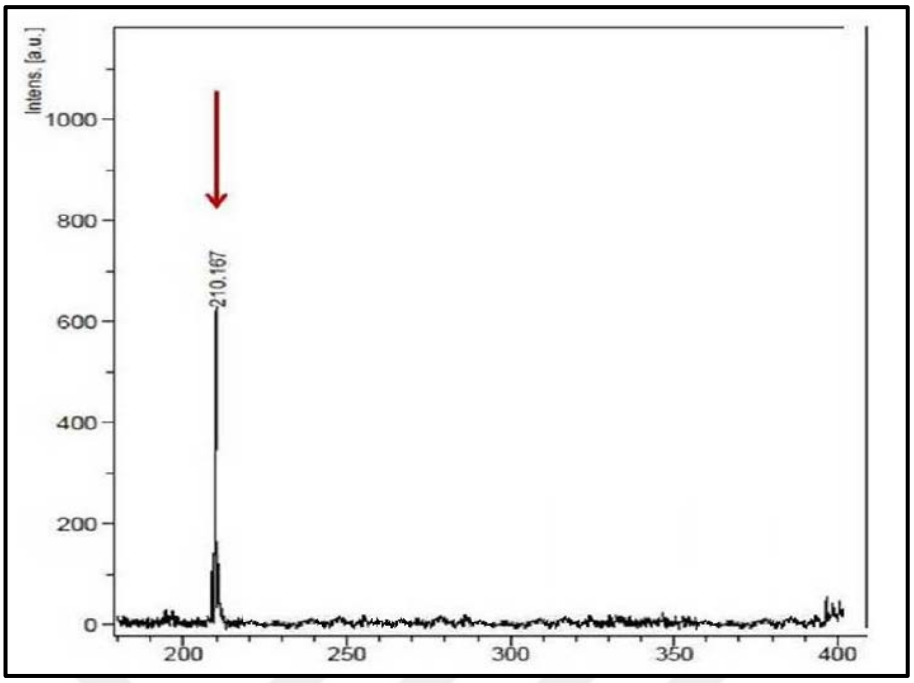

Figure 5.8: Mass spectrum of 4.

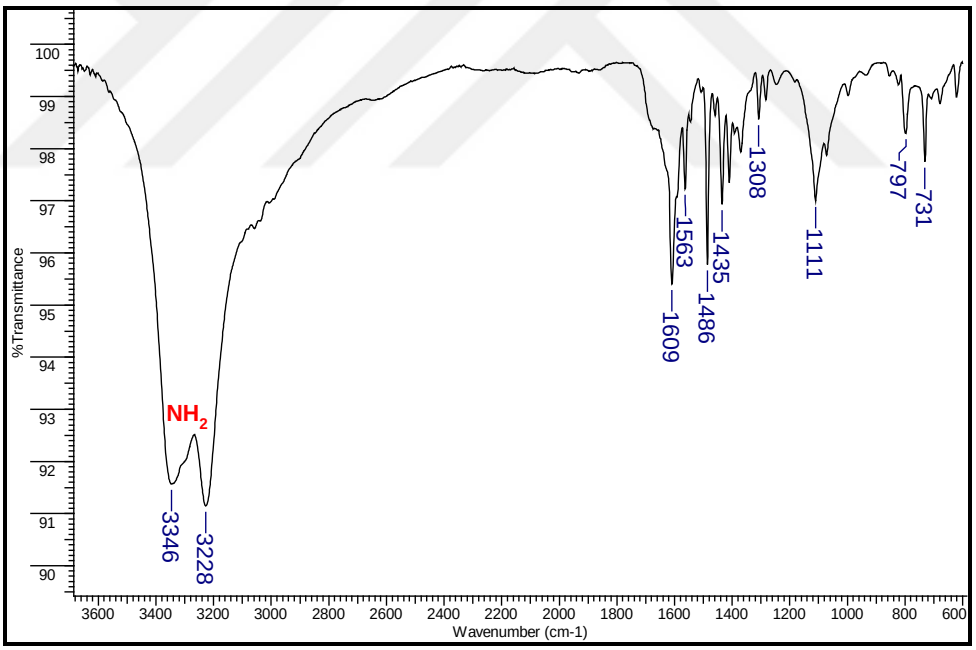

Figure 5.9: The FT-IR spectrum of 4.

5.1.1.4.Synthesis and characterization of 1,2-Bis-[(2,2-dimethyl-4,6-dioxo-1,3-dioxan-5-ylidenemethyl)amino]benzene (7).

For the synthesis of 1,2-Bis-[(2,2-dimethyl-4,6-dioxo-1,3-dioxan-5-ylidenemethyl)amino]benzene (**7**) we applied literature method [69].

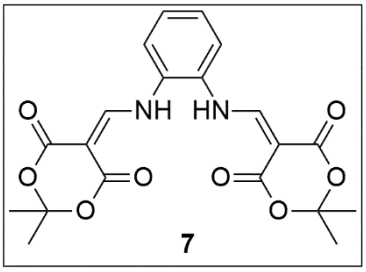

Figure 5.10: Molecular structure of 7.

In the mass spectrum of **7**, the molecular ion peak that appears at 438.24 represents $[M+Na]^+$ (Figure 5.11). Also in the FT-IR spectrum of compound show the necessary peaks, as ester C=O at 1725 cm^{-1} (Figure 5.12).

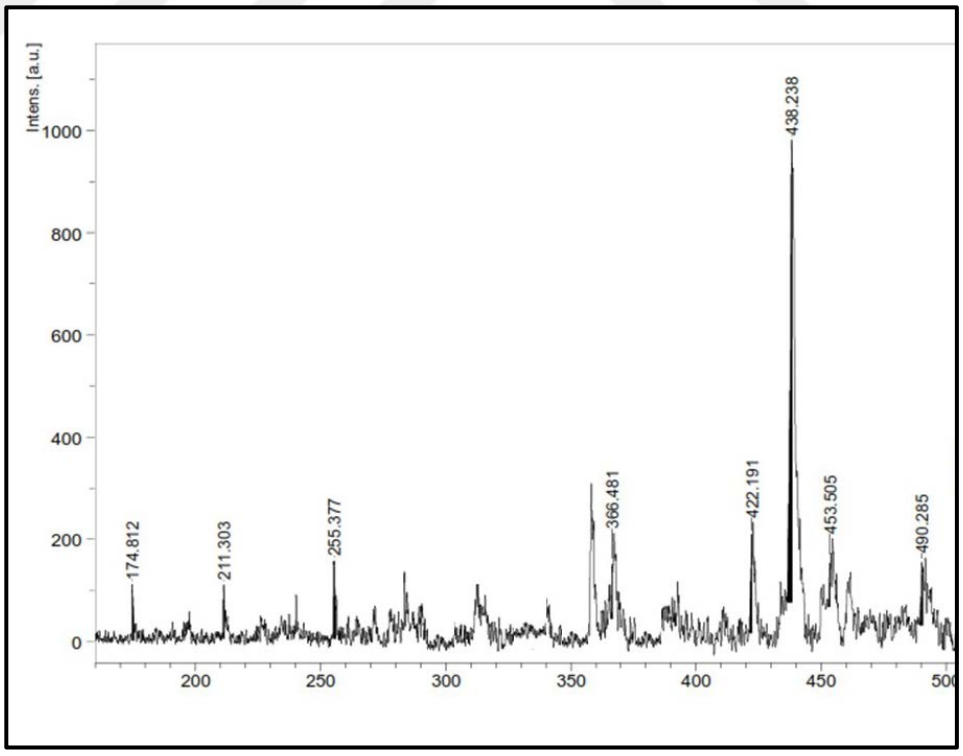

Figure 5.11: Mass spectrum of compound 7.

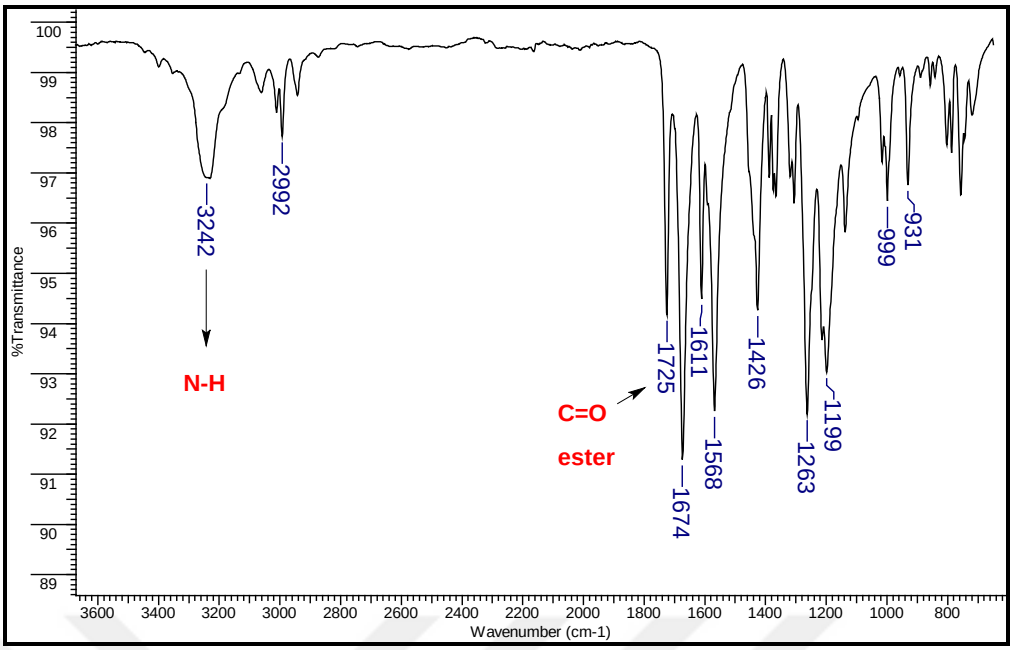

Figure 5.12: The FT-IR spectrum of compound 7.

5.1.1.5.Synthesis of 4,7-dione 1,10-phenanthroline (8)

The synthesis of 4,7-dione 1,10-phenanthroline (**8**) was carried out in the diphenyl ether over 30 minutes [70].

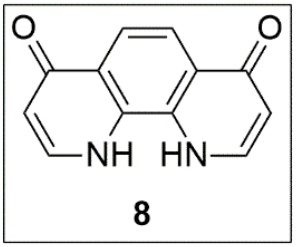

Figure 5.13: Molecular structure of 8.

The mass spectrum of the compound **8** demonstrates the molecular ion peak at 210.77 $(M-2H]^+$ (Figure 5.14). In Figure 5.15, the C=O stretch of the -dione can be seen at 1726 cm^{-1}. Other necessary peak belongs to the N-H that comes at 3226 cm^{-1}.

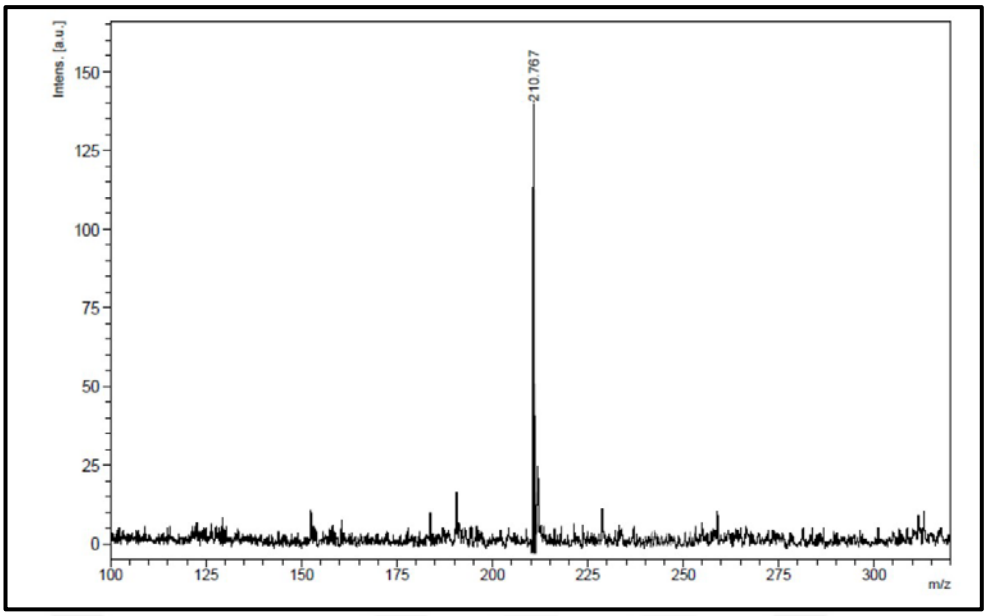

Figure 5.14: Mass spectrum of 8.

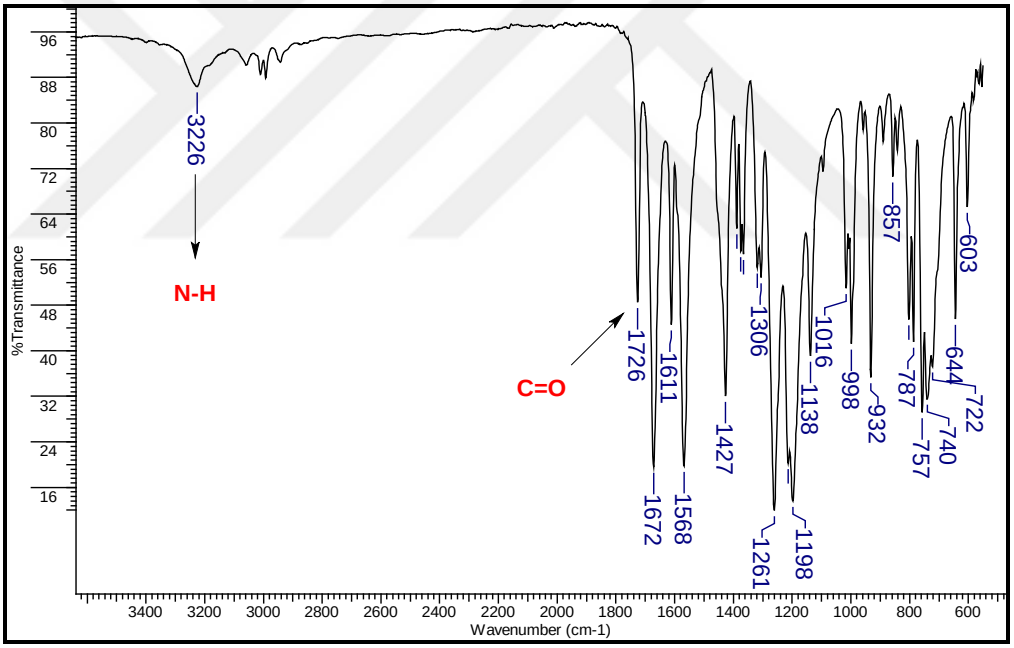

Figure 5.15: FT-IR spectrum of 8.

5.1.1.6.Synthesis of 4,7-Dichloro 1,10-Phenanthroline (9)

4,7-Dichloro 1,10-Phenanthroline (**9**) was synthesized according to the literature [70].

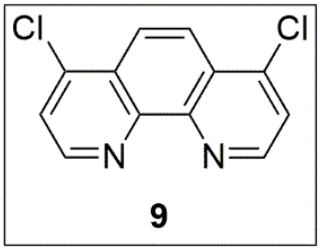

Figure 5.16: Molecular structure of 9.

According to the mass spectrometry analysis of **9**, molecular ion peak $[M]^+$ can be seen at 249.1 in Figure 5.17 below. In addition, FT-IR spectrum of the compound supports the molecular structure (Figure 5.18). All corresponding bond stretches are consisted with the compound **9**.

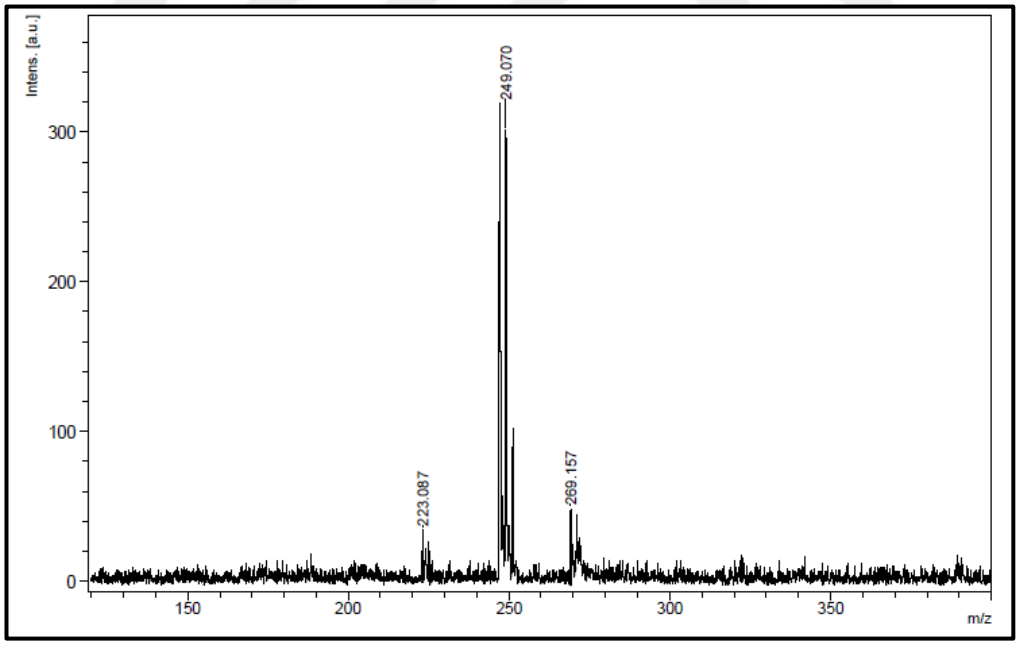

Figure 5.17: Mass spectrum of 9.

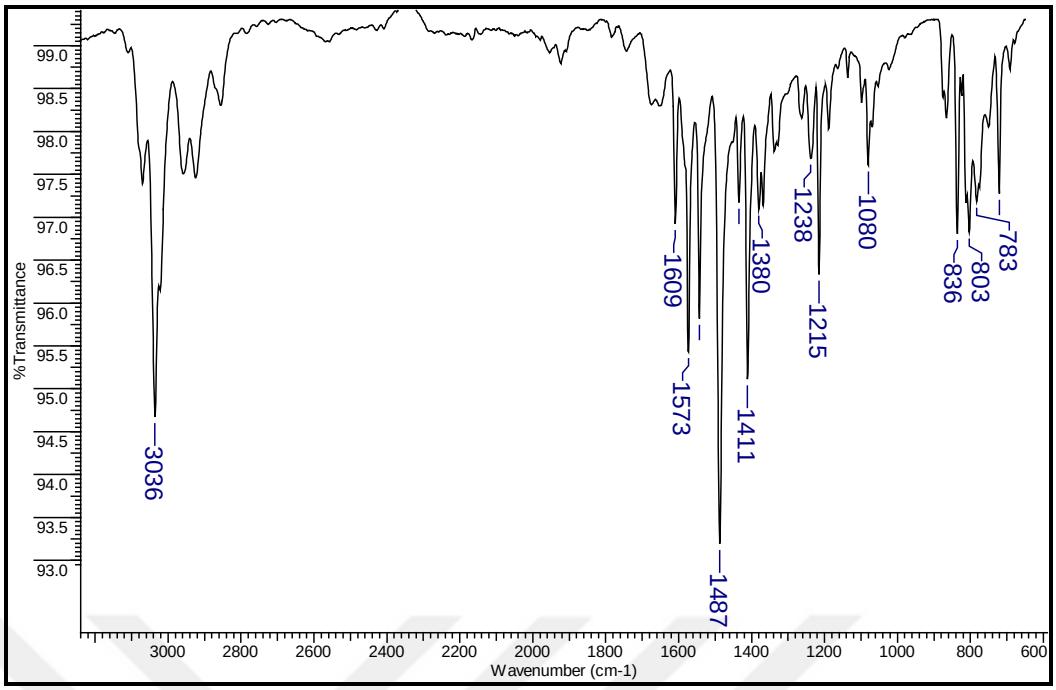

Figure 5.18: FT-IR spectrum of 9.

5.1.2. Synthesis and Characterization of Ruthenium(II) Complexes

5.1.2.1.Synthesis and Characterizations of bis(2,2'-bipyridine)dichlororuthenium(II) (10)

For the synthesis of bis(2,2'-bipyridine)dichlororuthenium(II) (**10**) a literature method was applied [71].

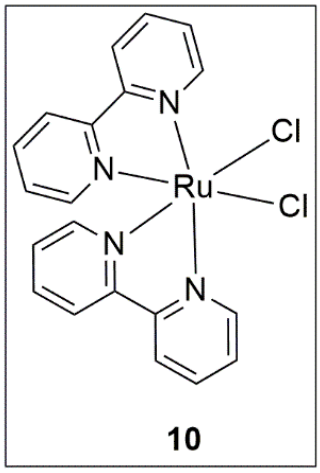

Figure 5.19: Molecular structure of 10.

In the Figure 5.20, the molecular ion peak at 484.77, and other related peaks that represent chlorine splits from the molecule can be easily noticed. Moreover, FT-IR spectrum of **10** confirms the molecular structure (Figure 5.21).

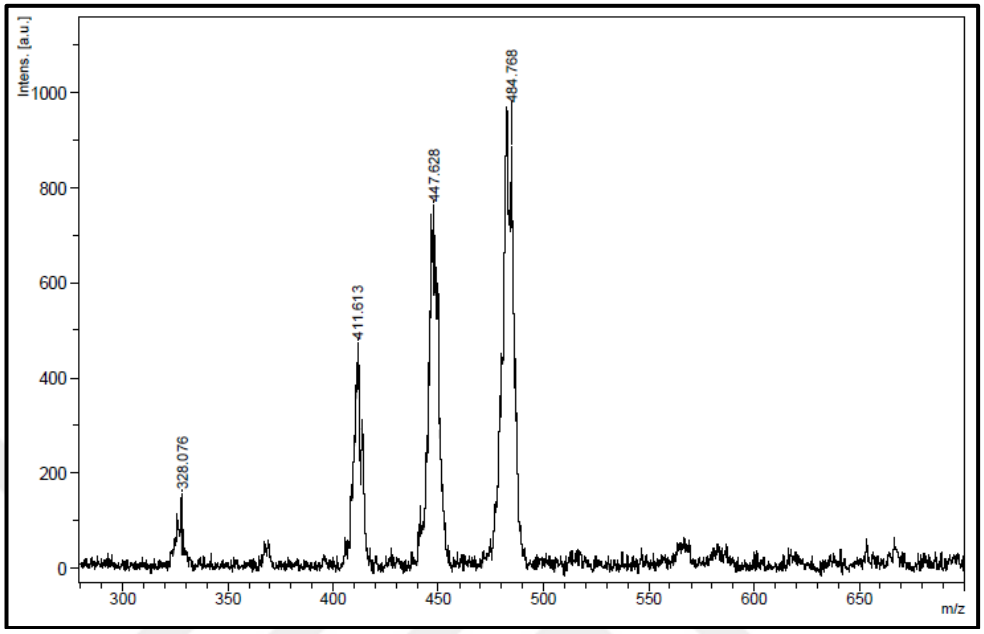

Figure 5.20: Mass spectrum of compound 10.

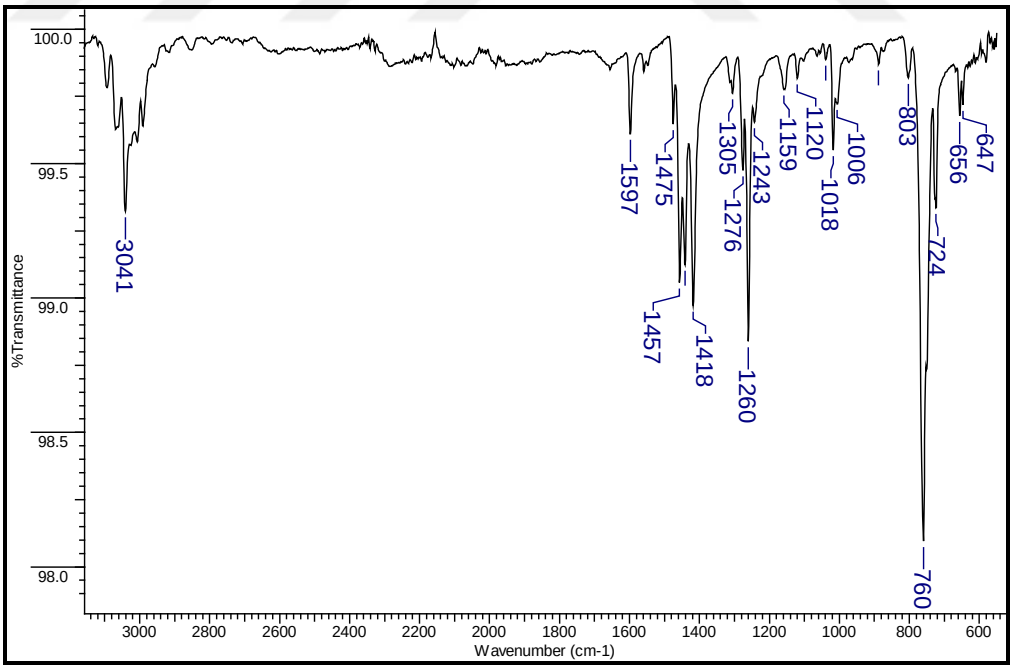

Figure 5.21: The FT-IR spectrum of compound 10.

5.1.2.2.Synthesis and Characterizations of 5,6-diamino phenanthroline Ruthenium(II) complex (11)

Synthesis of novel diamino-phenanthroline ruthenium complex (**11**) was developed by our group. The reaction was performed in EtOH, and ammonium hexafluorophosphate salt of the final complex was obtained.

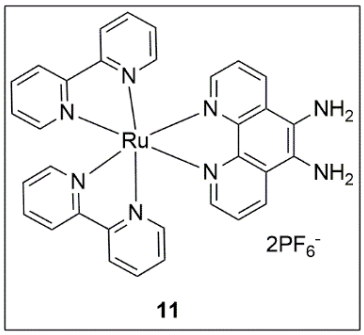

Figure 5.22: Molecular structure of 11.

According to the mass spectrum of **11**, 623.18 represents molecular ion peak with PF_6^- splits from the molecule $[M-2PF_6]^+$ (Figure 5.23). In the FT-IR spectrum of the compound **11**, all peaks are consisted with expected stretches. Also, at 835 cm^{-1} , peaks of PF_6^- counter ion of the complex are clear (Figure 5.24).

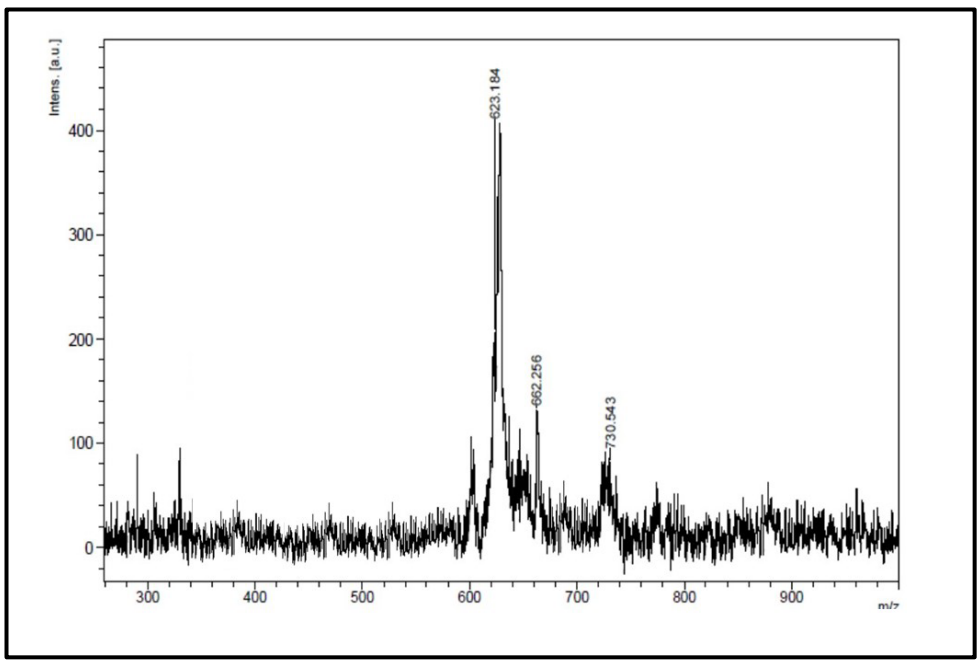

Figure 5.23: Mass spectrum of compound 11.

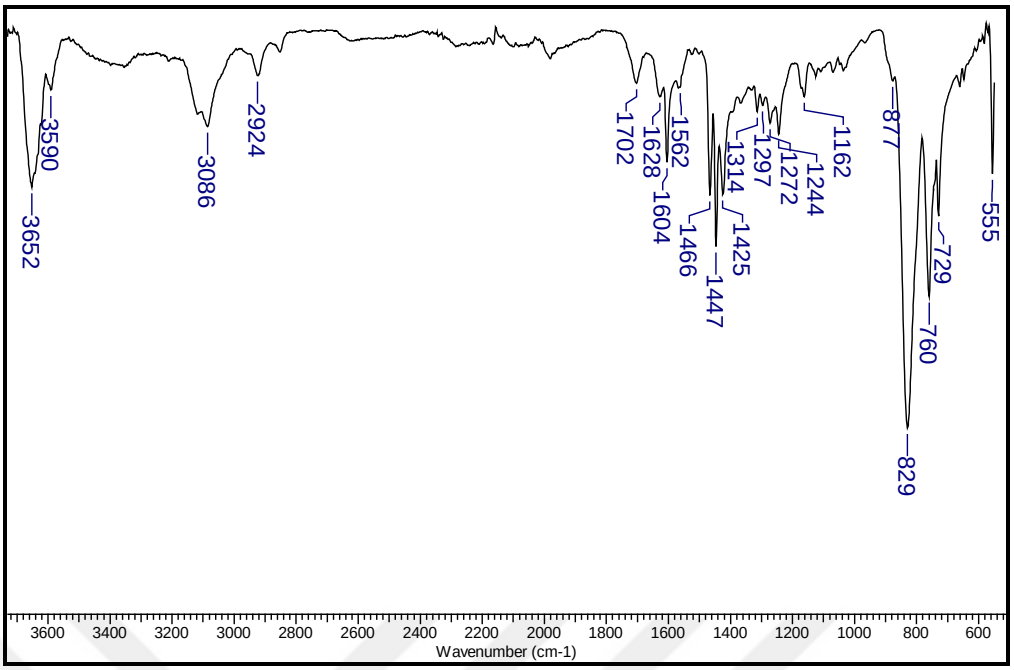

Figure 5.24: FT-IR spectrum of compound 11.

5.1.2.3.Synthesis and Characterizations of 4,7-dichlorophenanthroline ruthenium(II) complex (12)

The synthesis of novel ruthenium complex (**12**) that bearing 4,7-dichlorophenanthroline substitution was performed in EtOH/H_2O solvent mixture.

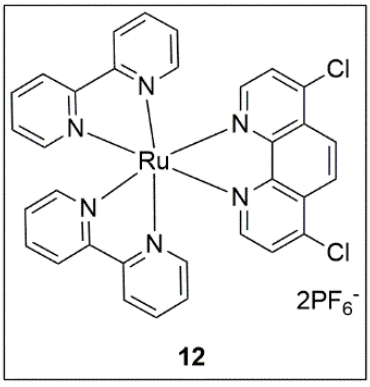

Figure 5.25: Molecular structure of **12**.

The resulting complex was analysed by mass and FT-IR spectrometry. In the mass spectrum of complex **12**, molecular ion peaks at *m/z* 662.07 and 629.42 represents $[M\text{-}2PF_6]^+$and $[M\text{-}2PF_6\text{-}Cl]^+$, respectively (Figure 5.26). Also, FT-IR spectrum of the complex confirms the molecular structure (Figure 5.27).

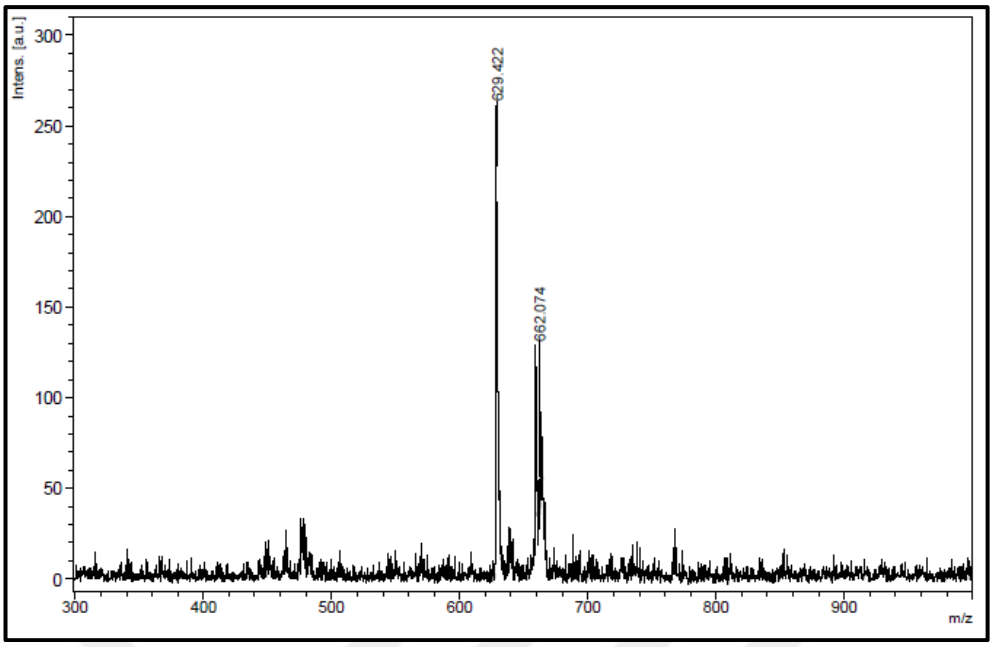

Figure 5.26: Mass spectrum of **12**.

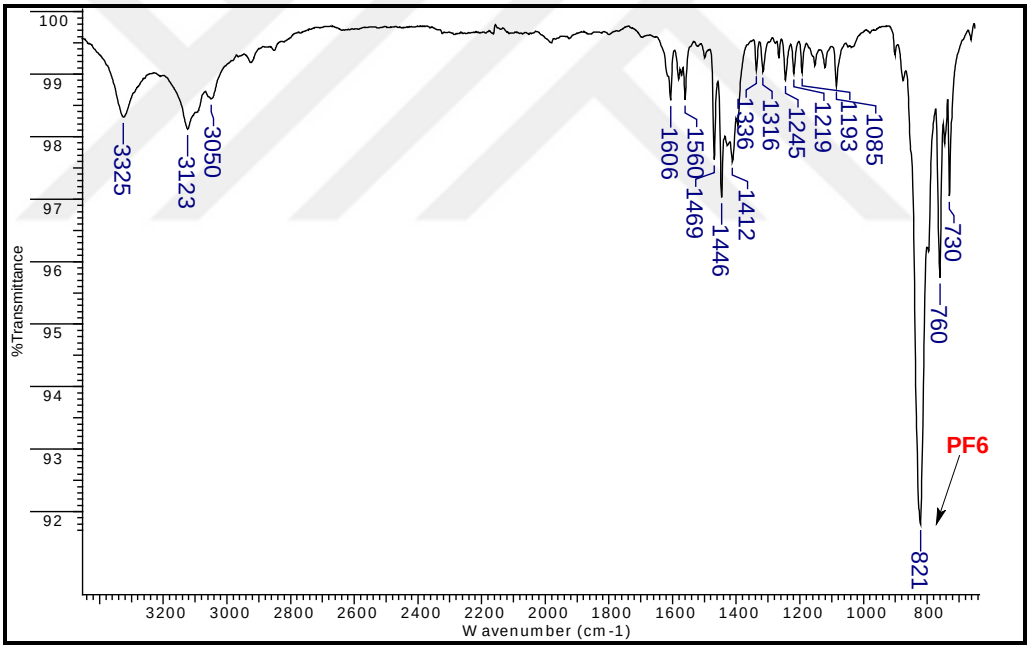

Figure 5.27: FT-IR spectrum of **12**.

This product was used in the next reactions without any detailed purification. By crystallization we could solve its single X-ray crystallographic data (Table 5.1). Both the crystal structure and the synthesis of **12** were reported for the first time by our group. Moreover, crystal structure of compound **12** with the atom-numbering representation is demonstrated in the Figure 5.28. According to the analysis, the central

metal has the distorted octahedral geometry and the Ru-N bond has an average distance as 2.065 Å. Phenanthroline core of the complex is planar. There is a distortion on phenylene ring (N3-N4-bipyridyl ring) that belongs one of the two bipyridyl parts. The bond lengths of the C-Cl atoms is 1702 and 1720 Å. Ruthenium(II) complex (**12**) has a hexafluorophosphate counter anion therefore it has two hexagonal PF_6 salt crystals in its structure (Figure 5.28).

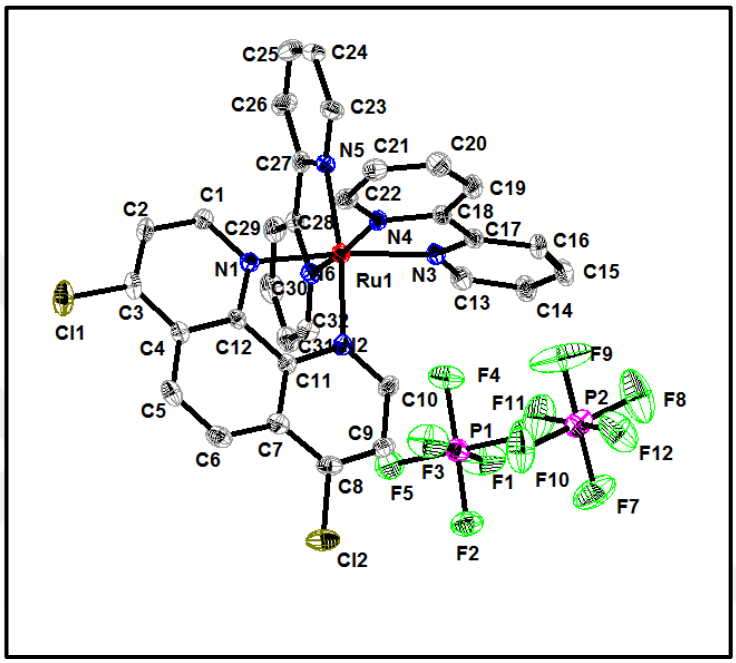

Figure 5.28: Crystal structure of compound **12** with the atom-numbering scheme. Displacement ellipsoids are drawn at the 30% probability level. The hydrogen atoms have been omitted for clarity.

Table 5.1: X-ray crystallographic data and refinement parameters for compound 12.

Empirical formula	$C_{32}H_{22}Cl_2F_{12}N_6P_2Ru$
Formula weight	952.46
Temperature (K)	295
Crystal system	Monoclinic
Space group	$P2_1/n$
a (Å)	11.1241 (12)
b (Å)	20.936 (2)
c (Å)	14.7692 (19)
β (°)	94.332 (6)
Volume (Å^3)	3429.8 (7)
Z	4
Density (calc, Mg/m^3)	1.845
Absorption coeff. (mm^{-1})	0.81
F(000)	1888
θ_{max} (°)	28.4
Reflections collected	33225
Independent reflections	8560
R_{int} (merging R value)	0.085
Parameters	496
R ($F^2>2\sigma F^2$)	0.058
wR (all data)	0.162
Goodness-of-fit on F^2	1.02

5.1.3. Synthesis and Characterization of 4,7-dichloro-phenanthroline iridium(III) complex (14)

The synthesis of 4,7-dichloro-phenanthroline iridium(III) complex (**14**) was performed in ethylene glycol. Once again, the PF_6 salt of the iridium complex was obtained.

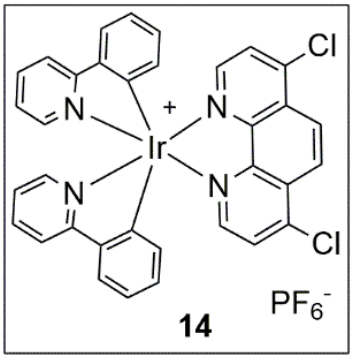

Figure 5.29: Molecular structure of 14.

In Figure 5.30, mass spectrum of complex **14** demonstrates the molecular ion peak at 749.51 which belongs to 749 $[M\text{-}PF_6]^+$. In addition, FT-IR spectrum of the molecule confirms the structure (Figure 5.31).

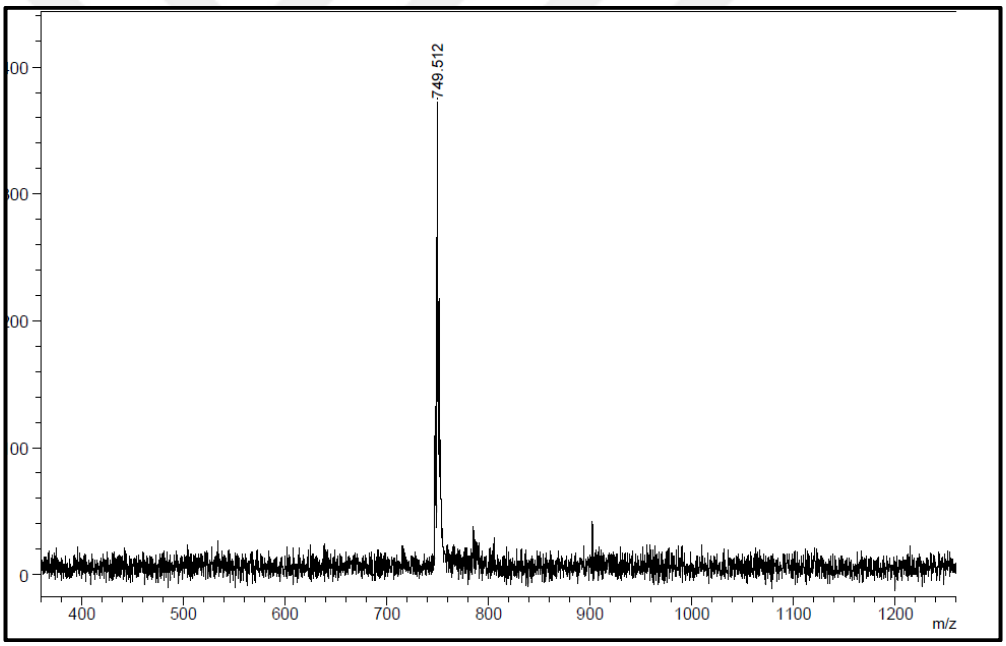

Figure 5.30: Mass spectrum of 14.

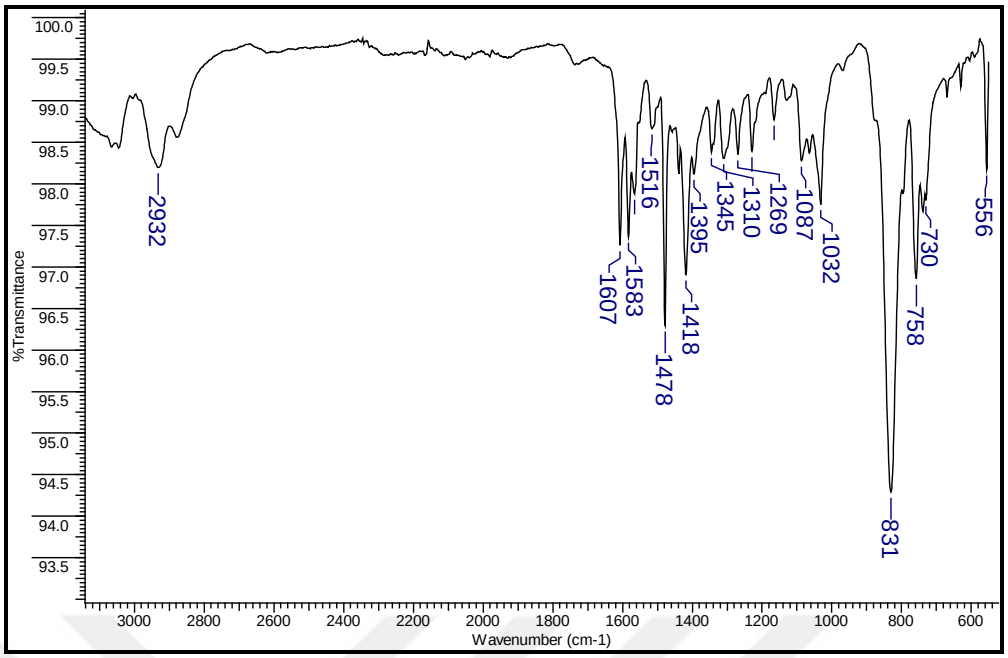

Figure 5.31: FT-IR spectrum of 14.

5.1.4. Synthesis and Characterization of Perylenes

5.1.4.1. Synthesis of 1,6,7,12-tetrabromo-3,4:9,10-dianhydride (16)

1,6,7,12-Tetrabromo-3,4:9,10-dianhydride (**16**) was synthesized by following a literature method [73].

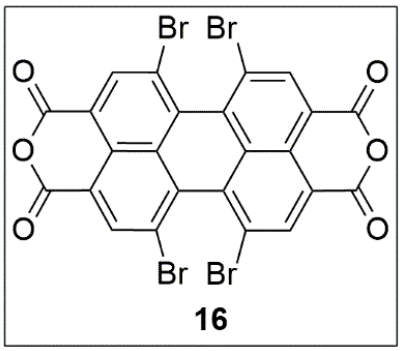

Figure 5.32: Molecular structure of 16.

Since **16** is insoluble in organic solvents, there is only FT-IR spectrum of the reaction mixture that contains tetrabromo-, tribromo- and dibromo-substituted

perylene dianhydride derivatives (Figure 5.33). Without any advanced purification techniques crude product was used for next steps.

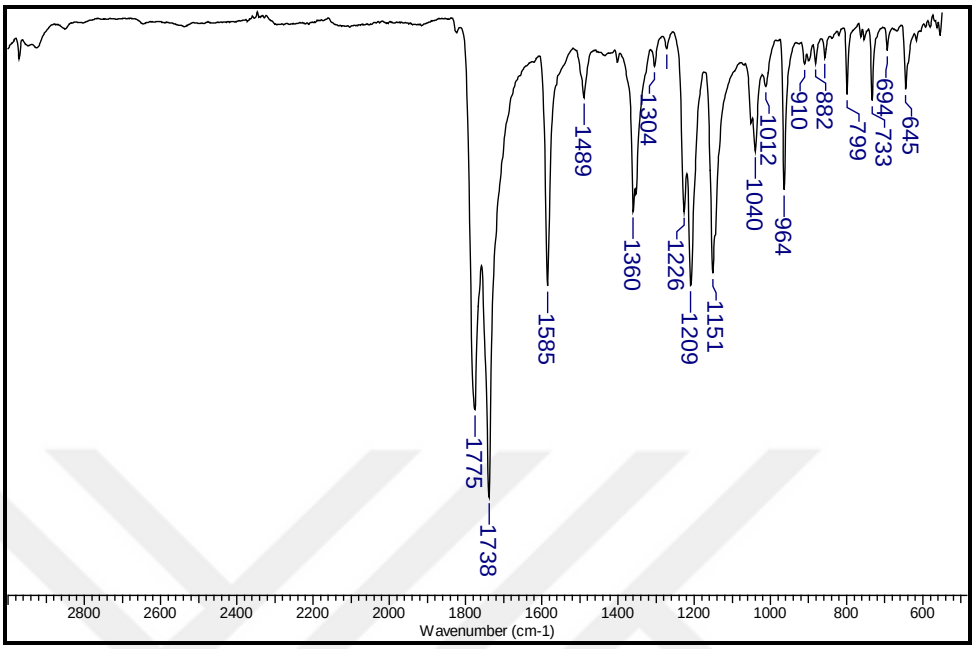

Figure 5.33: FT-IR spectrum of compound 16.

5.1.4.2.Synthesis and characterization of 1,6,7,12-tetrabromo-N,N'-(2,6-diisopropylphenyl)-perylene-3,4,9,10-bis(dicarboximide) (17)

1,6,7,12-Tetrabromo-N,N'-(2,6-diisopropylphenyl)-perylene-3,4,9,10-bis(dicarboximide) (**17**) was synthesized according to the literature method [74].

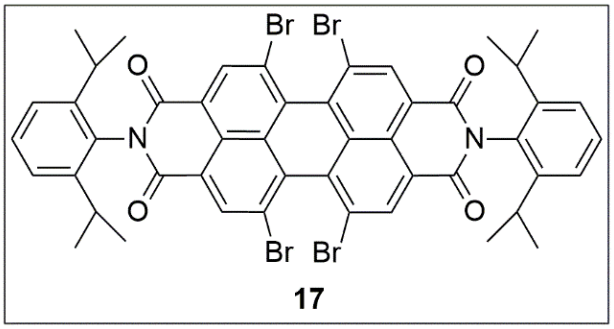

Figure 5.34: Molecular structure of 17.

There are only mass spectrum and FT-IR spectrum of compound, due to the fact that the reaction mixture contains tetrabromo-, dibromo- and tribromo substituted

diimides beside the target compound. Without purification of the mixture, next step was followed. In the mass spectrum of the compound **17**, side products are easily noticed (Figure 5.35). In the FT-IR spectrum, the C=O bond peaks are distinctive (Figure 5.36).

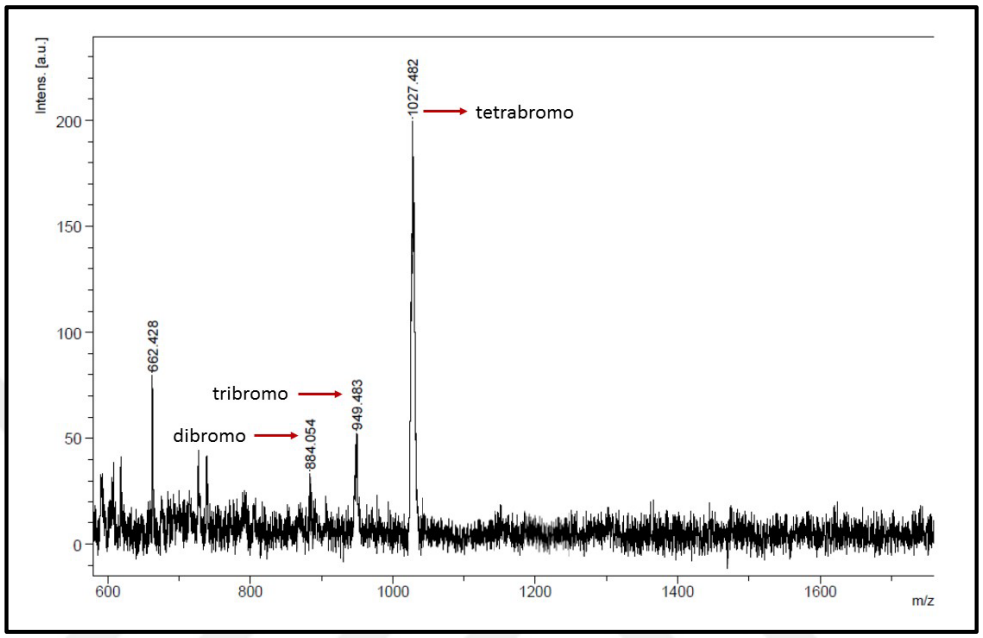

Figure 5.35: Mass spectrum of 17.

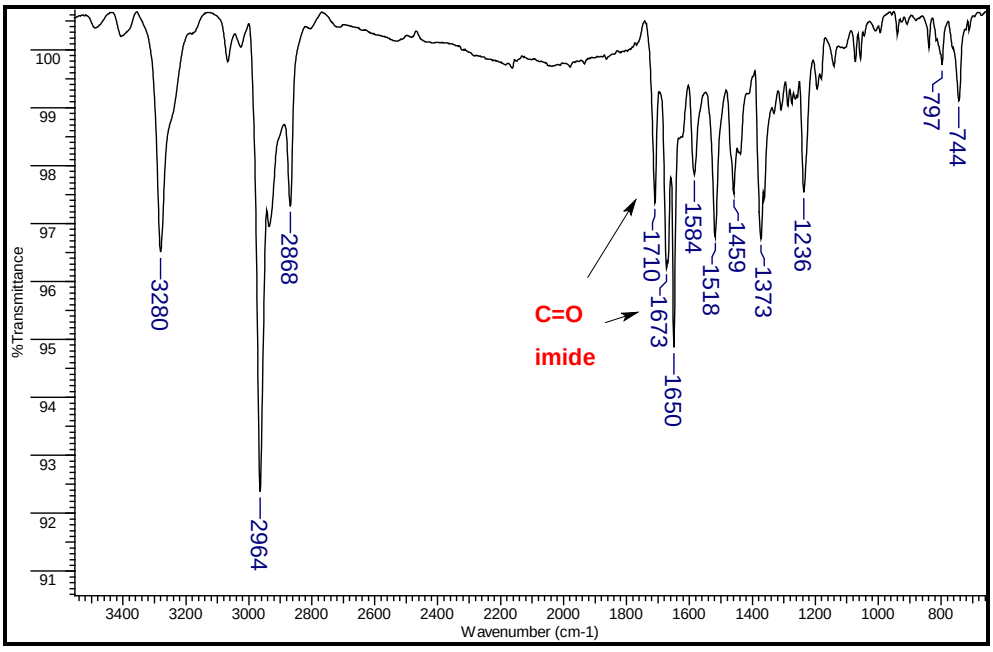

Figure 5.36: The FT-IR spectrum of **17**.

5.1.4.3.Synthesis and characterization of 1,6,7,12-tetra(4-tert-butyl-phenoxy)-N,N'-bis-(2,6-diisopropylphenyl)-perylene-3,4:9,10-bis(dicarboximide) (18)

1,6,7,12-Tetra(4-tert-butyl-phenoxy)-N,N'-bis-(2,6-diisopropylphenyl)-perylene-3,4:9,10-bis(dicarboximide) (**18**) was synthesized applying a literature method [75]. Full analyses of this compound were done carefully. Although the structure of the compound **18** was reported in some papers before, the crystal structure of the compound is published firstly by our group [86].

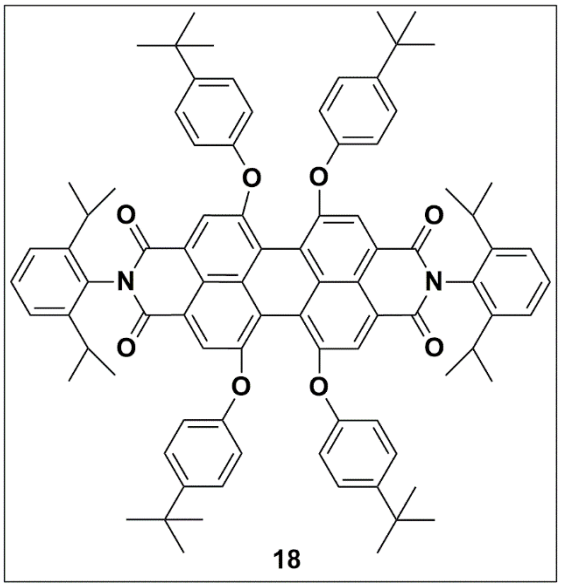

Figure 5.37: Molecular structure of **18**.

In Figure 5.38, the mass spectrum confirms the purity of the compound and the molecular ion peak 1303.29 represents $[M+H]^+$. Also in the FT-IR spectrum, all necessary peaks are consistent with the structure (Figure 5.39). The specific C=O imide peaks are shown at 1706 cm^{-1}.

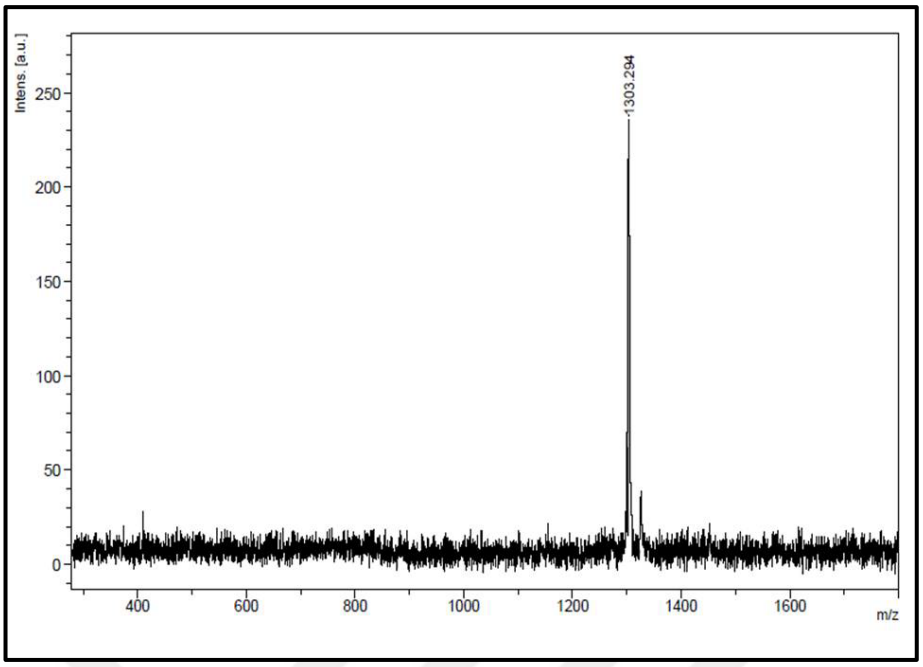

Figure 5.38: Mass spectrum of compound **18**.

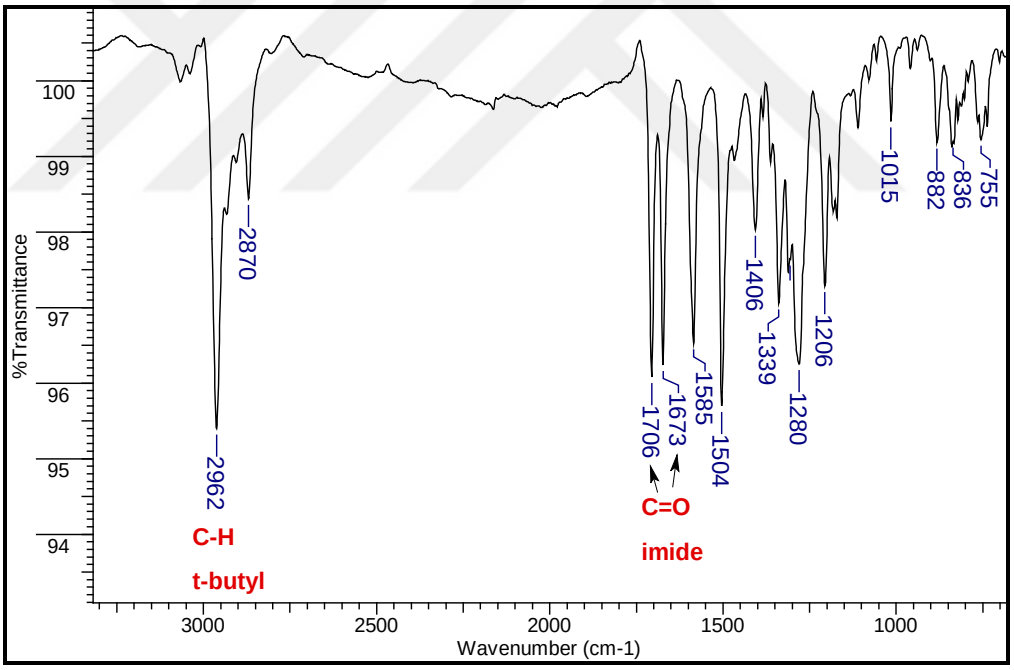

Figure 5.39: The FT-IR spectrum of compound **18**.

^{1}H NMR spectrum of compound **18** is given in Figure 5.40. Aromatic peaks appear between 8.50-6.70 ppm. Tertiary H of *i*-propyl groups of imide parts give a septet at 2.73 ppm. Methyl protons of the t-butyl groups appear at 1.28 while methyl protons of *i*-propyls come at 1.13 ppm. Also in the ^{13}C NMR spectrum of **18**, aromatic

carbons resonate between 163 and 119 ppm as expected (Figure 5.41). Aliphatic sp^3 carbons appear between 34-24 ppm in the high field of the spectrum.

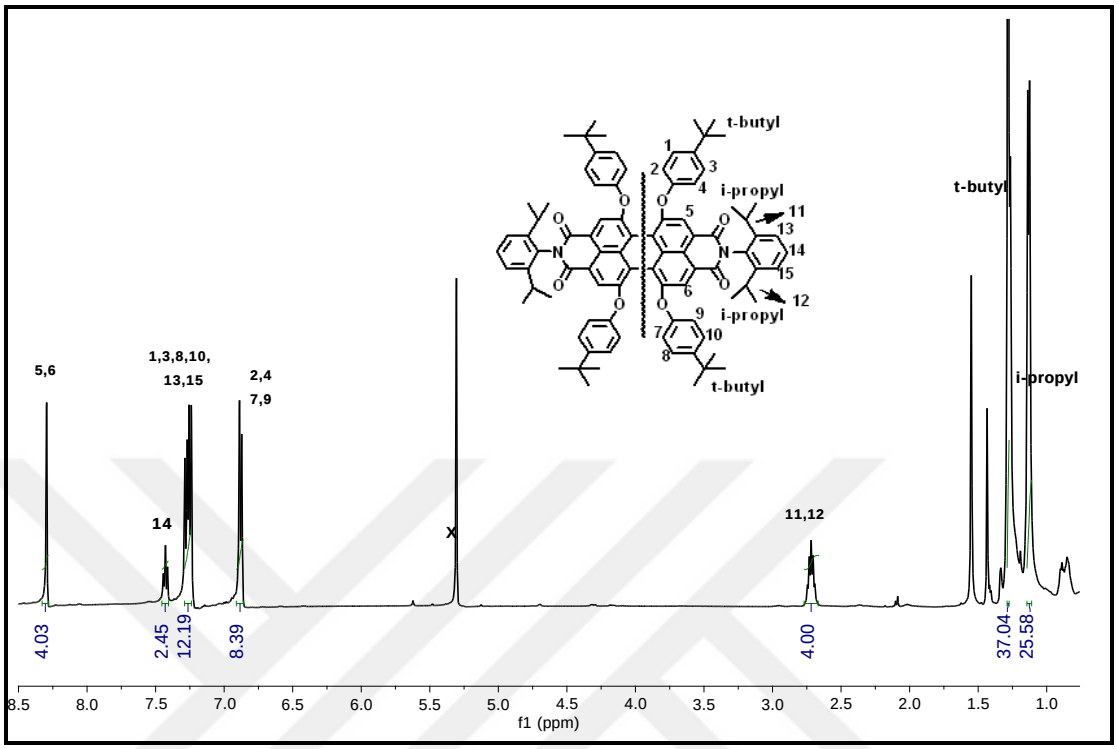

Figure 5.40: The ^{1}H NMR spectrum of compound 18.

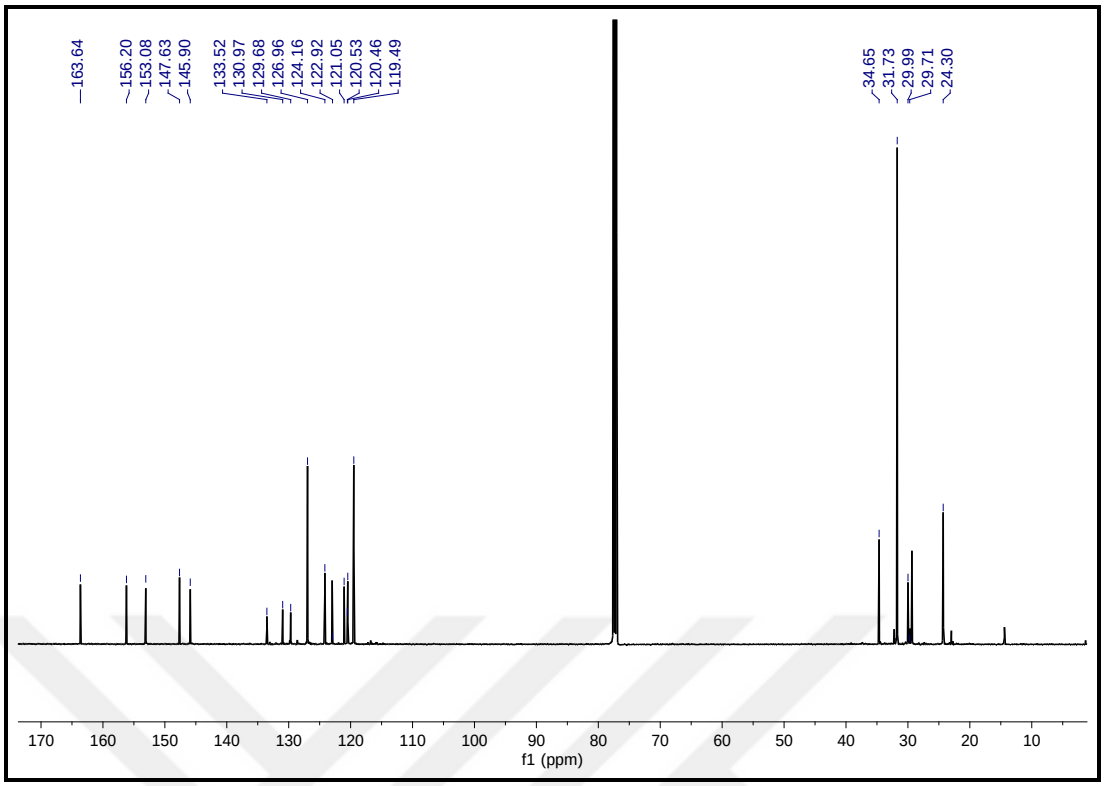

Figure 5.41: The ^{13}C NMR spectrum of compound 18.

As mentioned before, single X-ray crystal structure of **18** was characterized and published by our group for the first time (Figure 5.42). In the Table 5.2, refinement parameters are given in detail. The *tert*-butylphenoxy parts are oriented almost vertical to the naphthyl- part of perylene unit. Due to symmetry four *tert*-butylphenoxy units possess the same order according to naphtyl part. The value of the dihedral angle between the planes of two *tert*-butylphenoxy cores attached to same naphthyl unit is 54.48°. In the crystal of **18** there are only Van der Waals and edge-to-face interactions between the molecules (Table 5.3). Because the twisting of perylene skeleton its π–system was destroyed but the naphthyl moieties are planar.

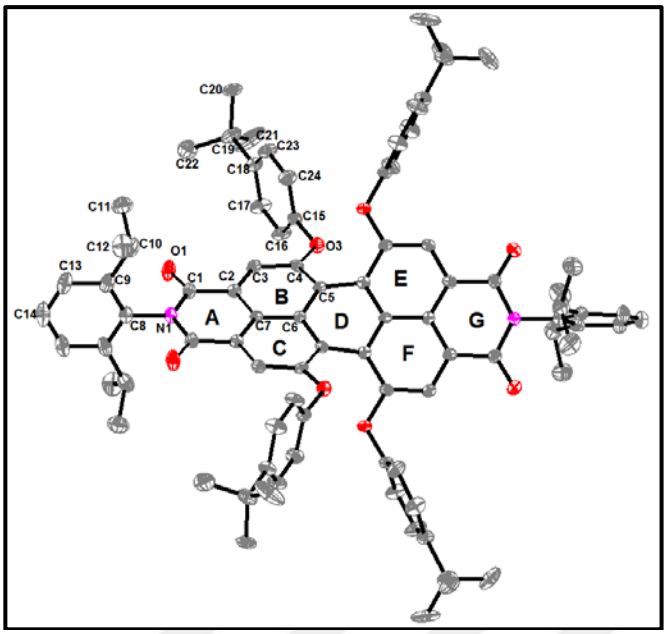

Figure 5.42: Crystal structure of compound 18. Displacement ellipsoids are drawn at the 30% probability level.

Table 5.2: X-ray crystallographic data and refinement parameters for compound 18.

Empirical formula	$C_{88}H_{90}N_2O_8$
Formula weight	1303.61 g/mol
Temperature (K)	173(2) K
Crystal system	Orthorhombic
Space group	F d d d
a (Å)	24.160(5)
b (Å)	25.471(5)
c (Å)	26.711(6)
Volume (Å^3)	16437.(6) Å^3
Z	8
Density (calc, Mg/m^3)	1.054 g/cm^3
Absorption coeff. (mm^{-1})	0.067 mm^{-1}
F(000)	5568
θ_{max} (°)	25.0
Reflections collected	26289
Independent reflections	3614

Table 5.2: Continued.

R_{int} (merging R value)	0.0940
Parameters	229
R (F^2>2σF^2)	0.0694
wR (all data)	0.2036
Goodness-of-fit on F^2	1.056

Table 5.3: Short ring-interactions for 18. d is the distance between ring centroids CgI and CgJ, α is the dihedral angle between planes I and J.

Planes *I* and *J*	**d, Å**	**α,^{0}**	**β,^{0}**	**Symmetry code for CgJ**
Cg1···Cg2	5.06	87.8	23.0	1/2-x,2-y,1/2-z
Cg1···Cg2	5.06	87.8	23	1/2-x,-1/4+y,1/4+z
Cg3···Cg2	5.112	84.9	25.5	1/2-x,2-y,1/2-z
Cg4···Cg2	5.112	84.9	25.5	1/2-x,-1/4+y,1/4+z
Cg1:N1C1C2C7C2#C1#; Cg2:C15C16C17C18C23C24; Cg3:C3C4C5C6C7; Cg4: C6C7C2#C3#C4#C5#				

5.1.4.4.Synthesis and characterization of 1,6,7,12-tetra(4-tert-butyl-phenoxy) carboximide carboxyanhydride (19)

Synthesis of 1,6,7,12-tetra(4-tert-butyl-phenoxy) carboximide carboxyanhydride (**19**) was achieved by a standard method [76].

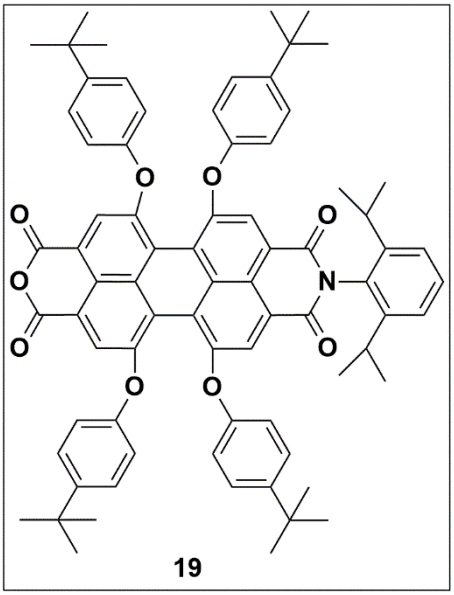

Figure 5.43: Molecular structure of 19.

The mass spectrum of the compound **19** is given in the Figure 5.44. The molecular ion peak at 1145.19 represents $[M+H]^+$. Moreover, in the FT-IR spectrum of the compound, we can see the necessary peaks of the structure in detail. Especially C=O peak observed at 1771 cm^{-1} supports the anhydride existence in the molecule (Figure 5.45).

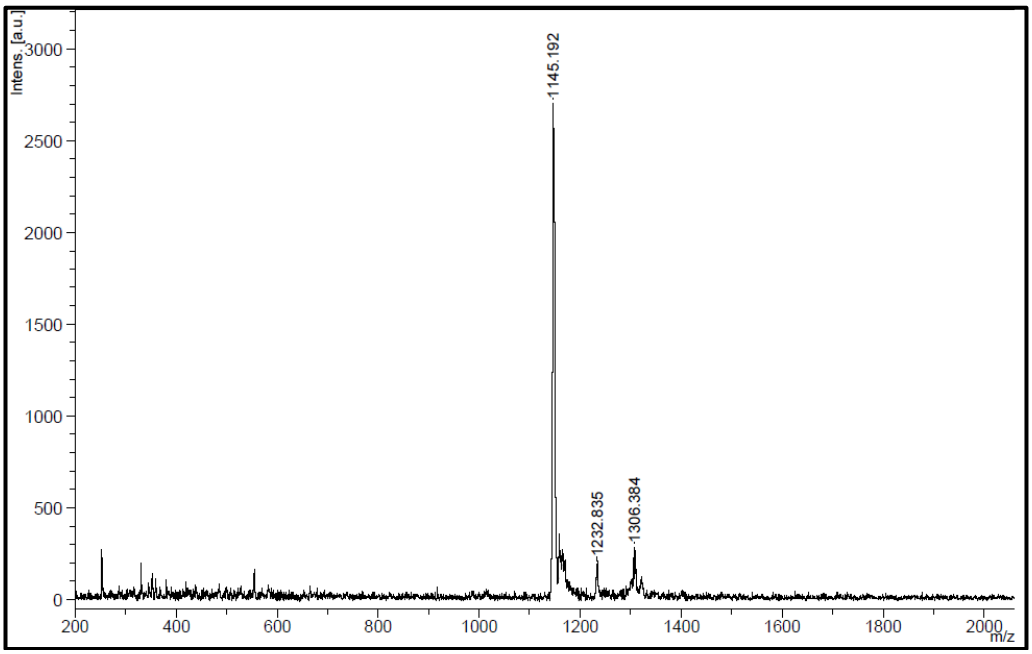

Figure 5.44: Mass spectrum of 19.

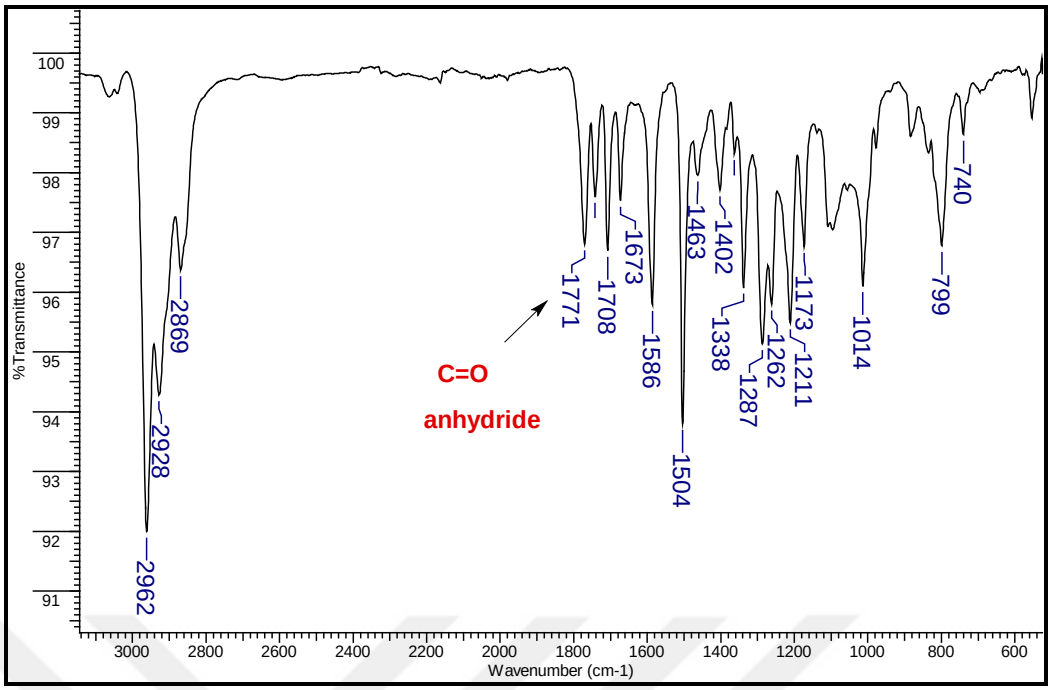

Figure 5.45: FT-IR spectrum of 19.

In the ^{1}H NMR of the spectrum, aromatic protons of the compound **19** appear between 8.27-7.25 ppm (Figure 5.46). As noted in the illustration, the specific tertiary protons of the two isopropyl group come at 2.6 ppm as septet. The peaks of t-butyl and i-propyl methyl protons are given at 1.3 and 1.1 ppm, respectively. ^{13}C NMR spectrum of compound **19** is shown in Figure 5.47. The sp^2 carbons of the structure resonate between 163-115 ppm. Also aliphatic carbons appear between 34-14 ppm in the spectrum.

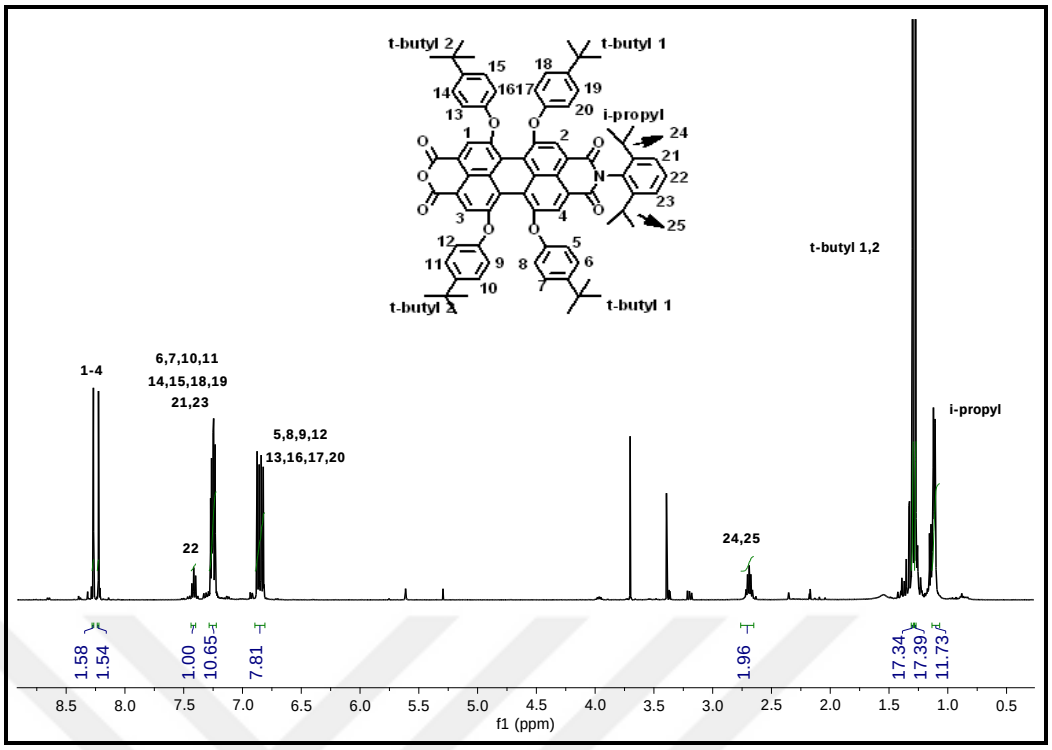

Figure 5.46: The ^{1}H NMR spectrum of compound 19.

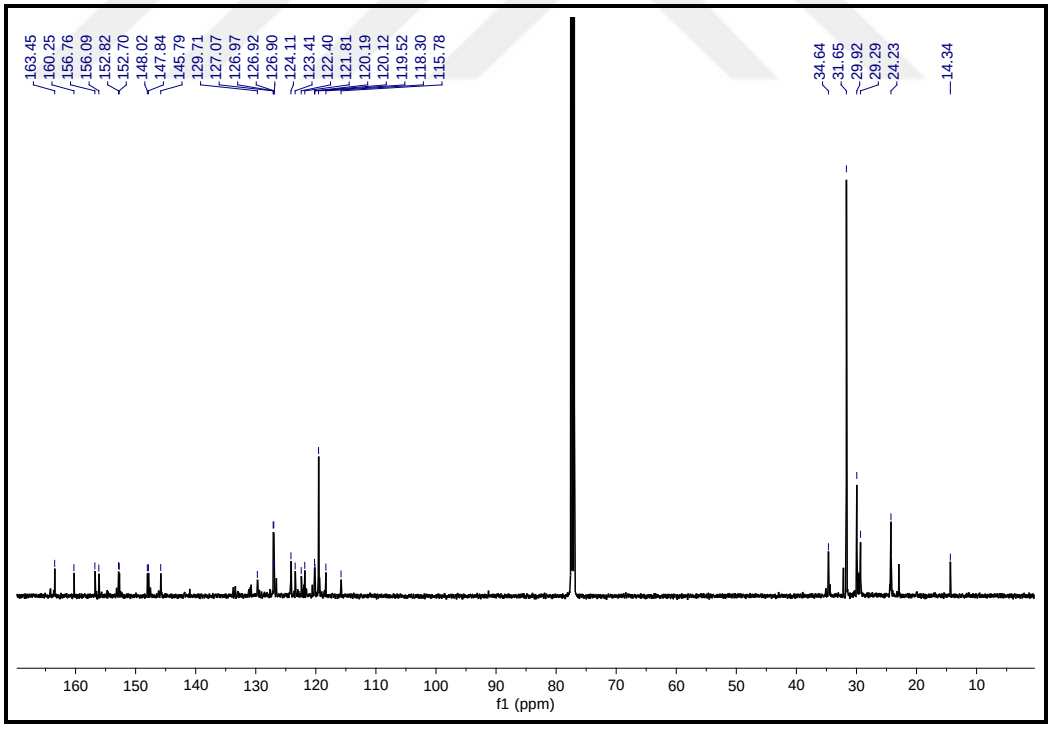

Figure 5.47: The ^{13}C NMR spectrum of compound 19.

5.1.4.5.Synthesis and characterization of perylenediimide (20)

Synthesis of perylenebisimide (**20**) was performed in propionic acid over 24 h. The novel perylenebisimide derivative **20** was fully characterized by mass, FT-IR and NMR spectrometry, respectively.

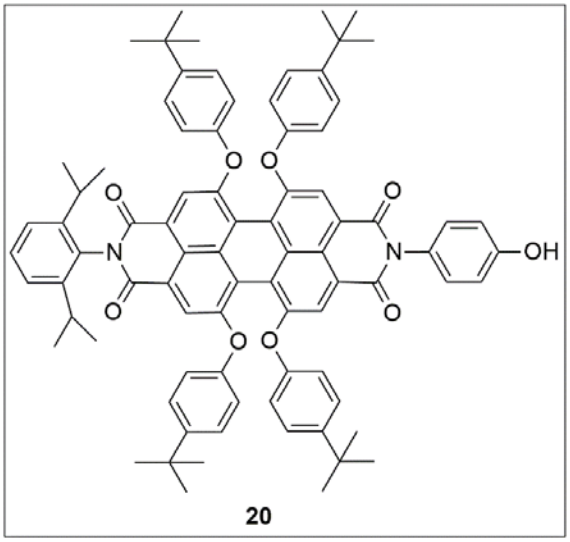

Figure 5.48: Molecular structure of 20.

In the mass spectrum of compound **20**, molecular ion peak is seen at 1235.50 that belongs to $[M]^+$ (Figure 5.49). Additionally, in Figure 5.50, FT-IR spectrum of the compound confirms the molecular structure of **20**. Specifically, O-H signal comes at 3406 cm^{-1} and C=O imide signal comes at 1705 cm^{-1} supports the molecular structure clearly.

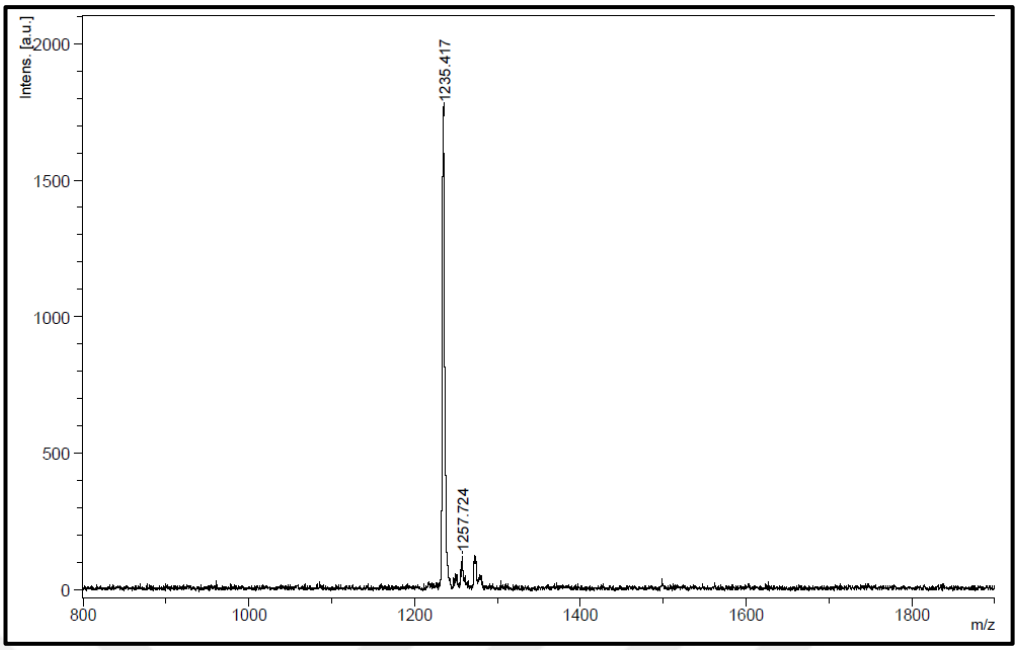

Figure 5.49: Mass spectrum of 20.

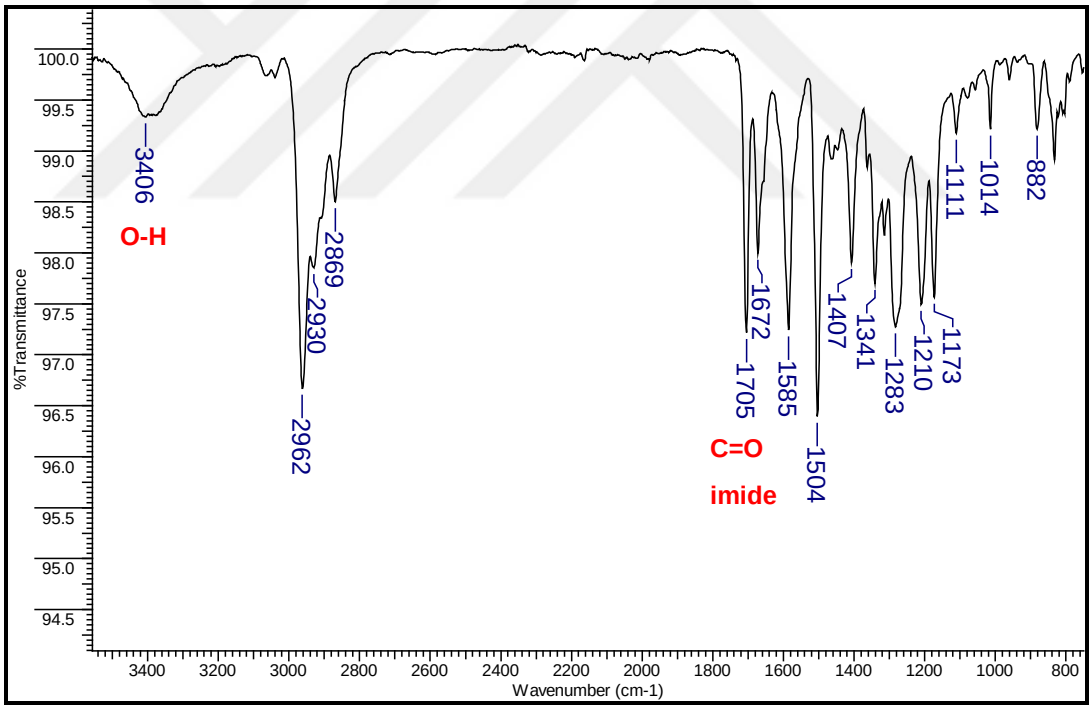

Figure 5.50: FT-IR spectrum of 20.

^{1}H NMR and ^{13}C NMR spectra of **20** are depicted in Figure 5.51 and 4.52. Aromatic protons of the molecule come between 8.3-6.8 ppm (Figure 5.51). The specific perylene protons (6-9) appear at 8.2 ppm as two singlets. Also, the O-H proton of the diimide side comes at 5.1 ppm as singlet. The distinctive isopropyl protons

(29,30) appear at 2.7 ppm as septet. The methyl protons are showed at 1.2 and 1.1 ppm in the spectrum. In the ^{13}C NMR spectrum of the compound, aromatic carbons resonate between 164-116 ppm (Figure 5.52). The methyl carbons and other aliphatic carbons appear between 34-24 ppm.

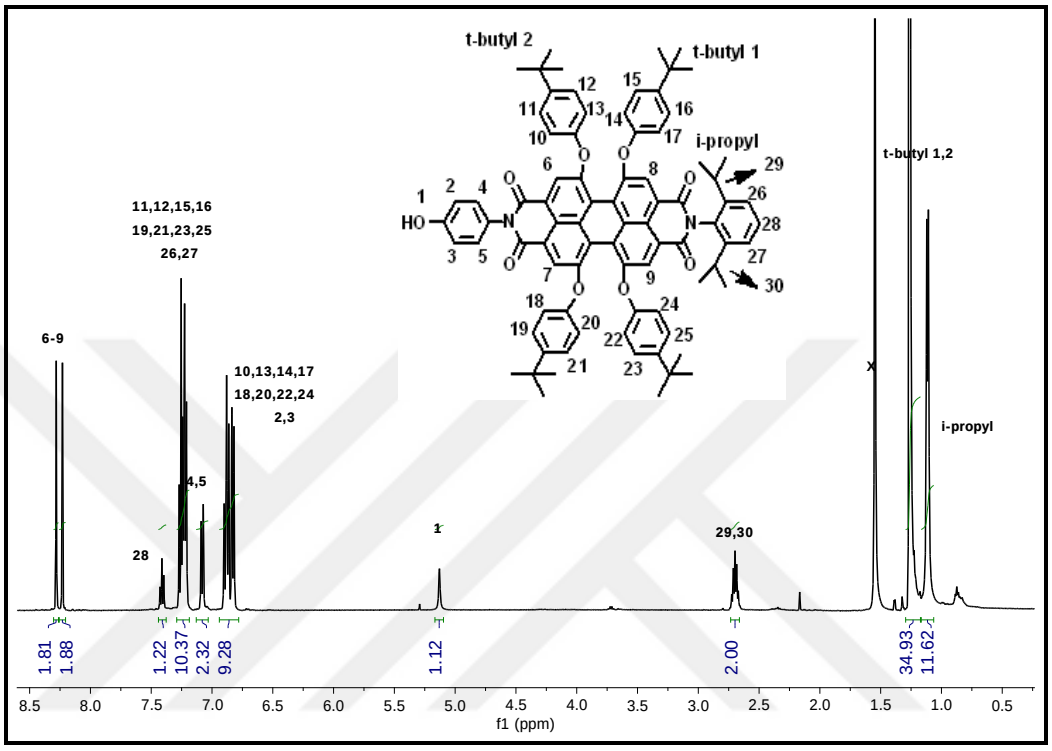

Figure 5.51: ^{1}H-NMR spectrum of 20.

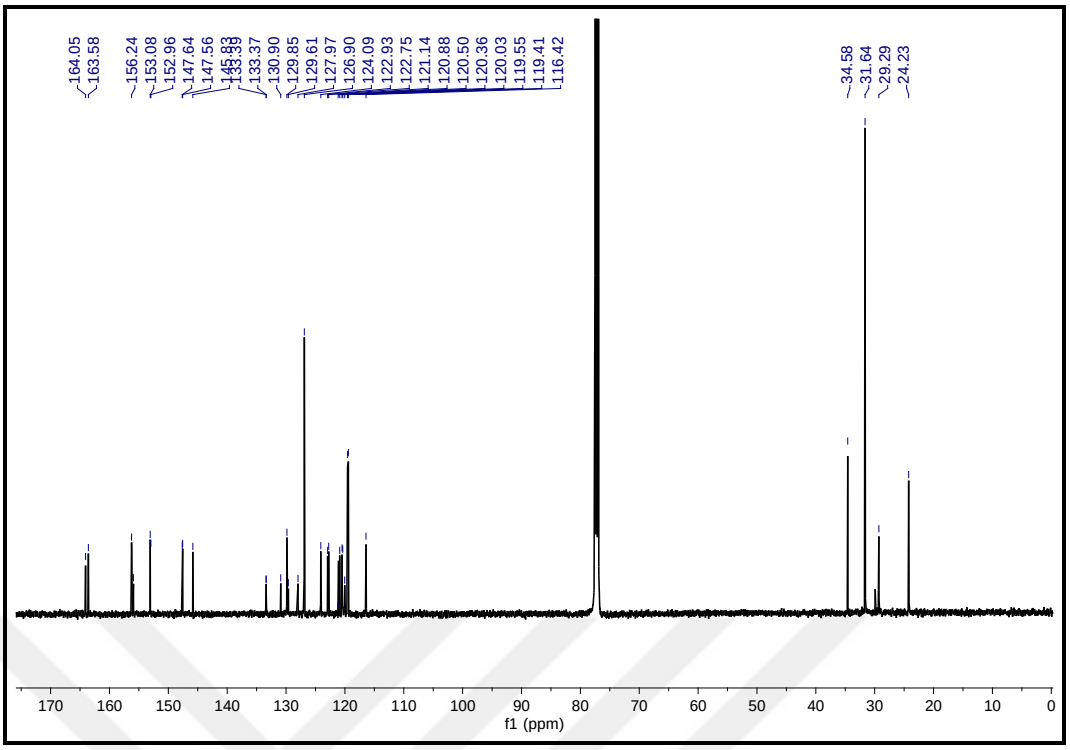

Figure 5.52: ^{13}C-NMR spectrum of 20.

5.1.5. Synthesis and Characterization of 3,5-distryl BODIPY (22)

The synthesis of 3,5-distryl BODIPY (**22**) was performed in benzene medium. The structural analyses were done by mass, FT-IR and NMR spectrometry. Both the structure and single X-ray analyses of this compound is firstly reported by our group [87].

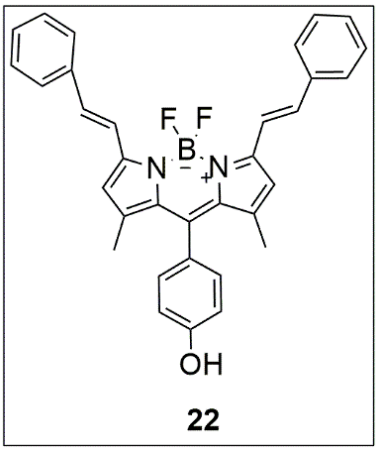

Figure 5.53: Molecular structure of 22.

According to the mass spectrum, 516.19 belongs to the molecular ion peak of **22** (Figure 5.54). Additionally, in Figure 5.55 FT-IR of the **22** is given. The sharp stretch of the O-H is shown at 3463 cm^{-1} besides other peaks are consistent with the molecular structure.

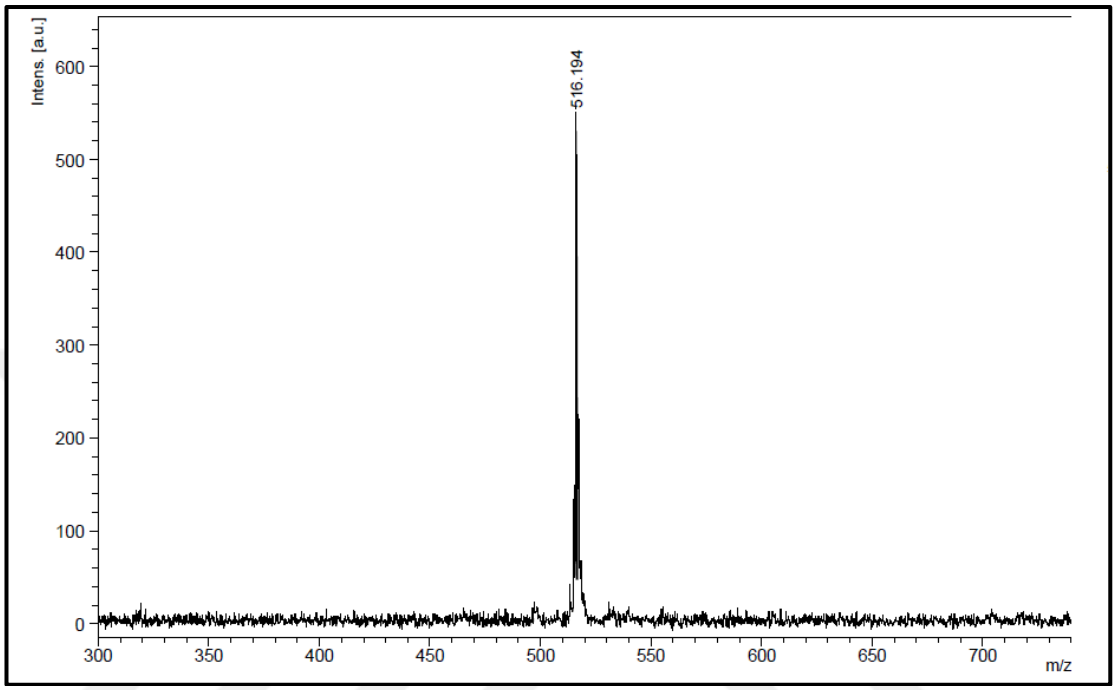

Figure 5.54: Mass spectrum of 22.

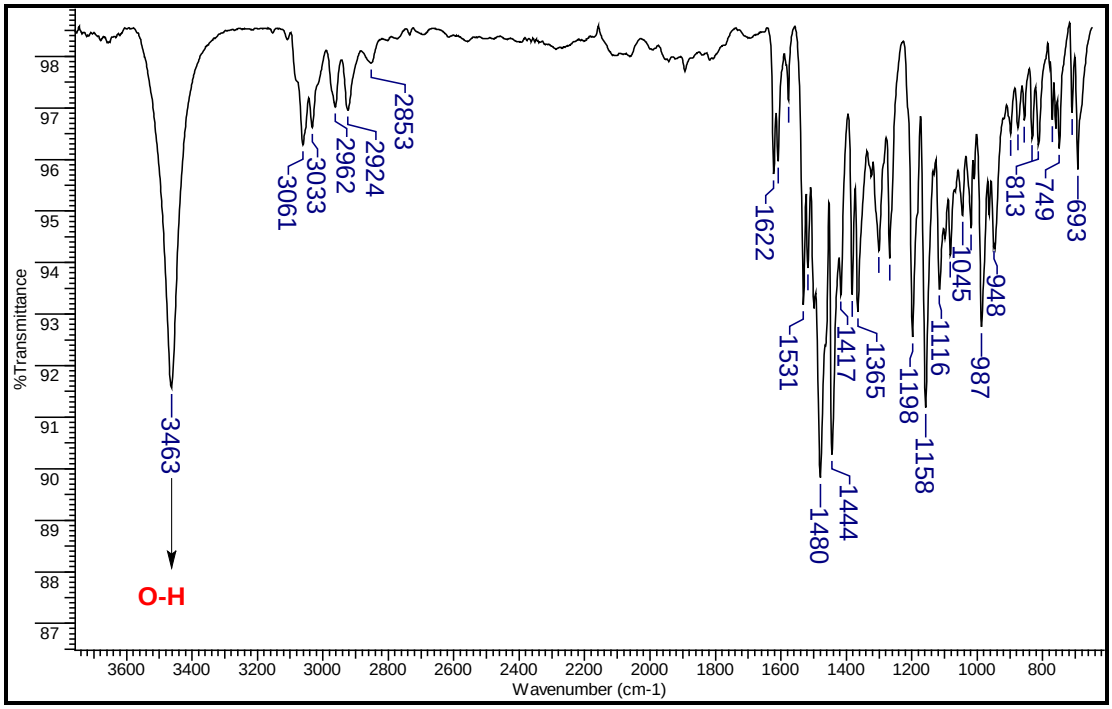

Figure 5.55: FT-IR Spectrum of 22.

The ^{1}H and ^{13}C NMR spectra of the compound **22** are shown in Figure 5.56 and 4.57. In the ^{1}H NMR spectrum of the molecule, aromatic protons resonate between 7.8-6.9 ppm. Specifically, the olefinic trans protons of the distryl units appear at 7.75 and 7.53 ppm as doublets. Moreover, in the ^{13}C NMR spectrum, aromatic sp^2 carbons resonate between 159-117 ppm. Aliphatic carbon of the methylene groups come at 15 ppm (Figure 5.57).

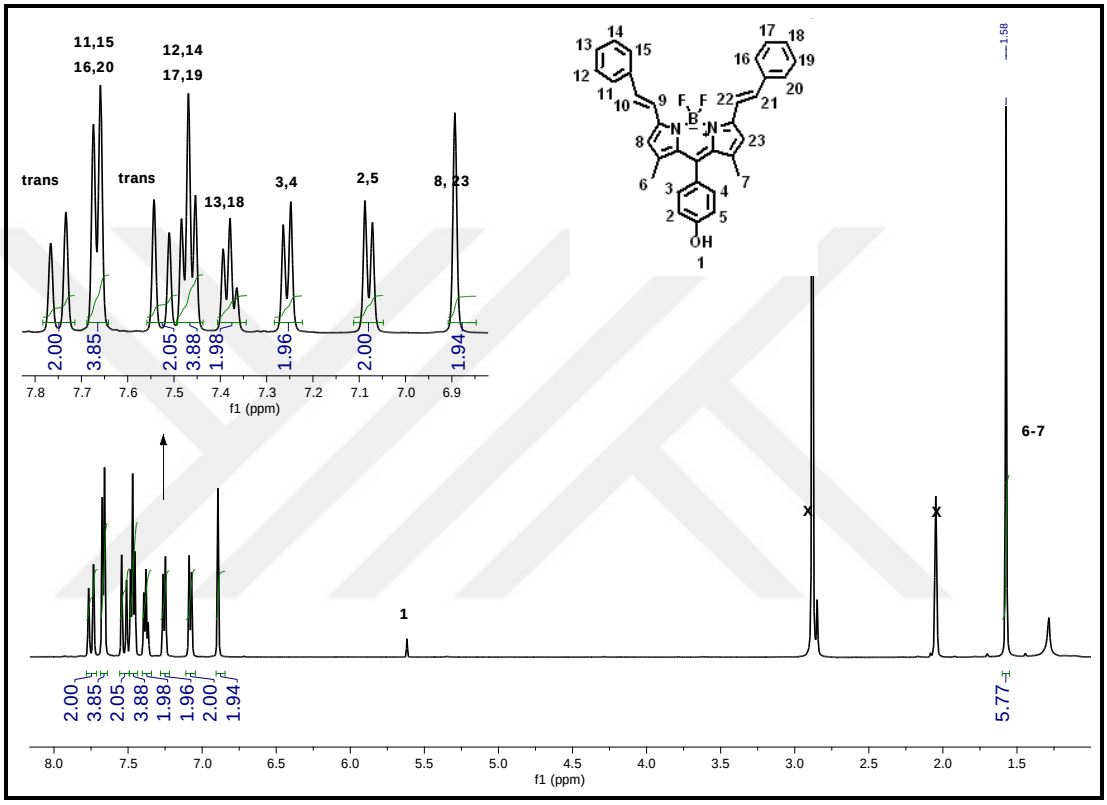

Figure 5.56: ^{1}H-NMR spectrum of 22.

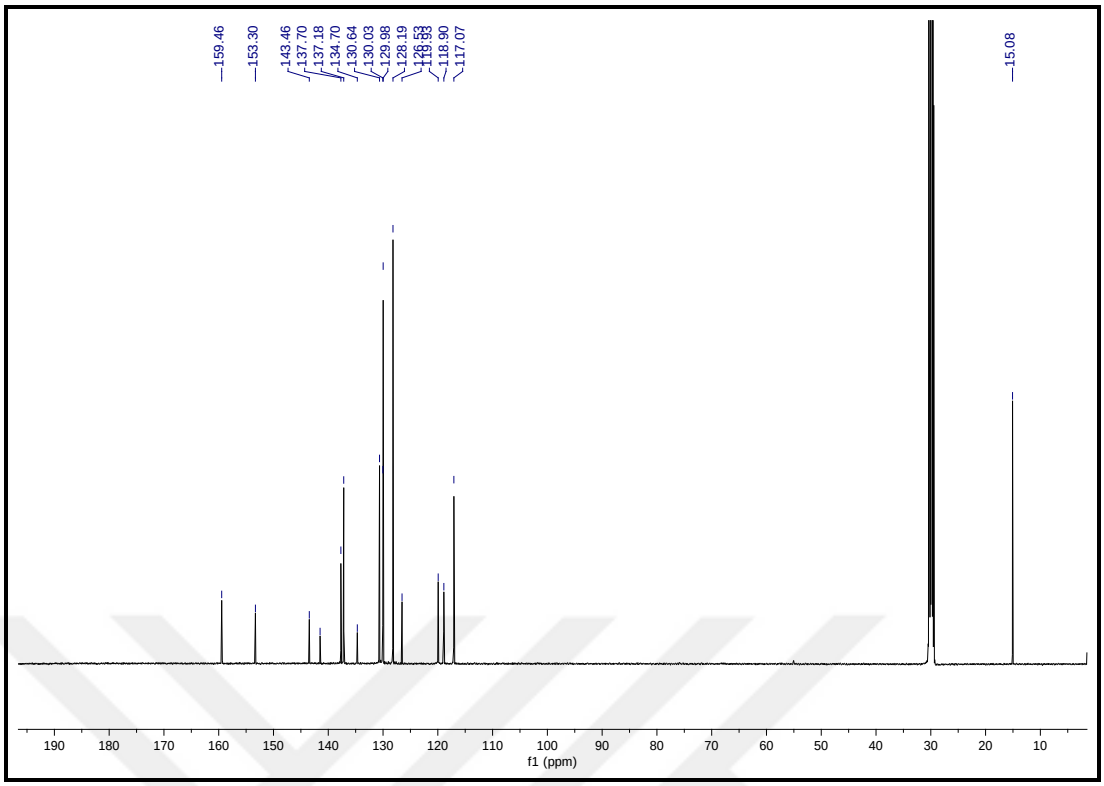

Figure 5.57: ^{13}C-NMR spectrum of 22.

The crystal structure of compound **22** is shown in Figure 5.58 and the crystallographic data are demonstrated in Table 5.4.

Compound **22** is a new BODIPY compound that including two distryl moiety bonds to C1 and C9 of the BODIPY with a *trans*-configuration. The main body of the structure is almost planar with a six-membered rings and two five-membered. The angle between the planes of BODIPY and phenol ring is 79.33°.

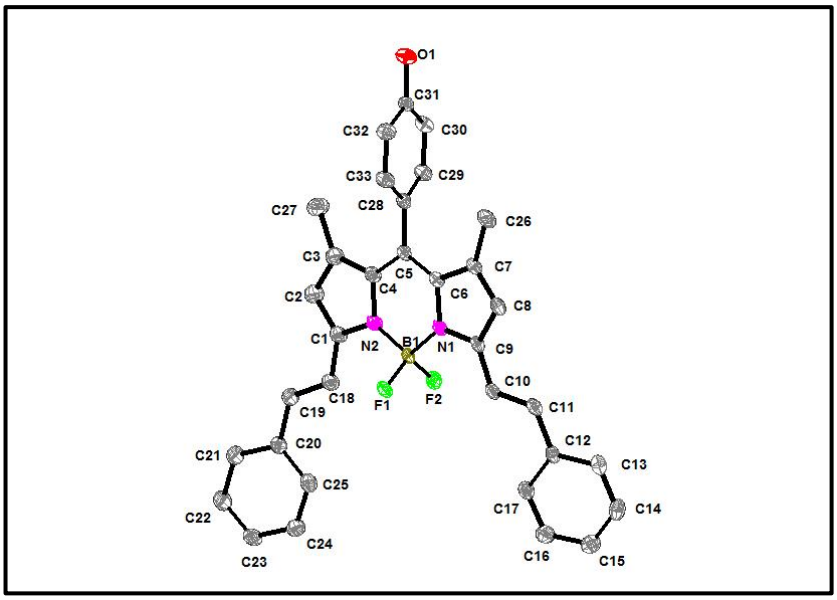

Figure 5.58: Crystal structure of compound 22 with the atom-numbering scheme. Displacement ellipsoids are drawn at the 30% probability level.

Table 5.4: X-ray crystallographic data and refinement parameters for compound 22.

Empirical formula	$C_{33}H_{27}BF_2N_2O$
Formula weight	516.73
Temperature (K)	173
Crystal system	Monoclinic
Space group	C2/c
a (Å)	26.758 (9)
b (Å)	9.137 (2)
c (Å)	22.861 (6)
β (°)	109.102 (18)
Volume ($Å^3$)	5281 (3)
Z	8
Density (calc, Mg/m^3)	1.299
Absorption coeff. (mm^{-1})	0.09
F(000)	2160
θ_{max} (°)	25.0
Reflections collected	15349
Independent reflections	4646
R_{int} (merging R value)	0.085
Parameters	357
R ($F^2>2\sigma F^2$)	0.067
wR (all data)	0.182
Goodness-of-fit on F^2	1.04

5.1.6. Synthesis and Characterization of Ruthenium and Iridium Bis(perylenediimide) Metal Complexes

5.1.6.1.Synthesis and characterization of bis(perylenediimide) ruthenium(II) complex (23)

For the synthesis of bis(perylenediimide) ruthenium(II) complex (**23**) was performed using a new ruthenium(II) dichloro complex and a new perylenediimide derivative. Nucleophilic substitution reaction in DMF gave the novel product **23** in good yields. Compound **23** is the first example of 4,7-phenanthroline substituted ruthenium complex and also it contains two perylenediimide moiety at the same time in a complex [88]. Full characterization of **23** was analysed successfully.

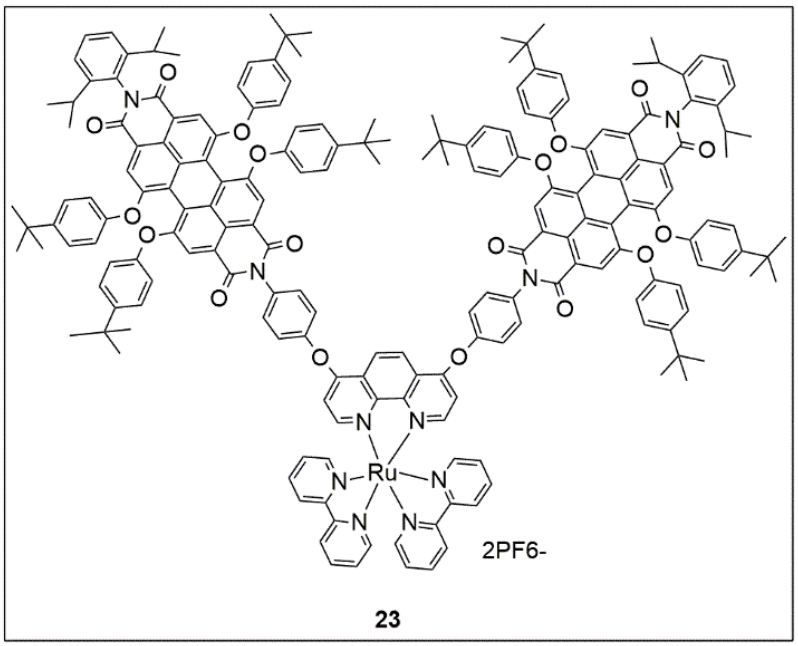

Figure 5.59: Molecular structure of 23.

According to the mass spectrum of the compound, the molecular ion peak at 3060.35 representing $[M\text{-}2PF_6]^+$ is clearly seen in Figure 5.60. Also, in the FT-IR spectrum of the complex, all the necessary aliphatic and aromatic peaks are depicted (Figure 5.61). The disappearance of the O-H stretch and the C=O bond stretch at 1705 cm^{-1} confirm the molecular structure.

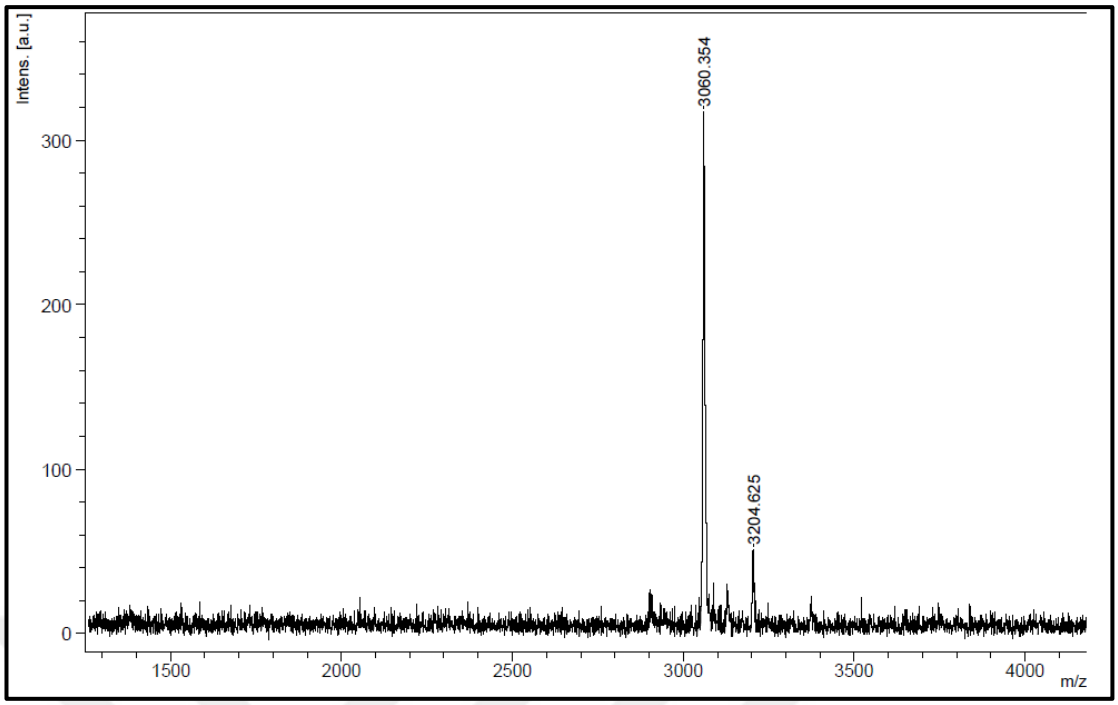

Figure 5.60: Mass spectrum of compound 23.

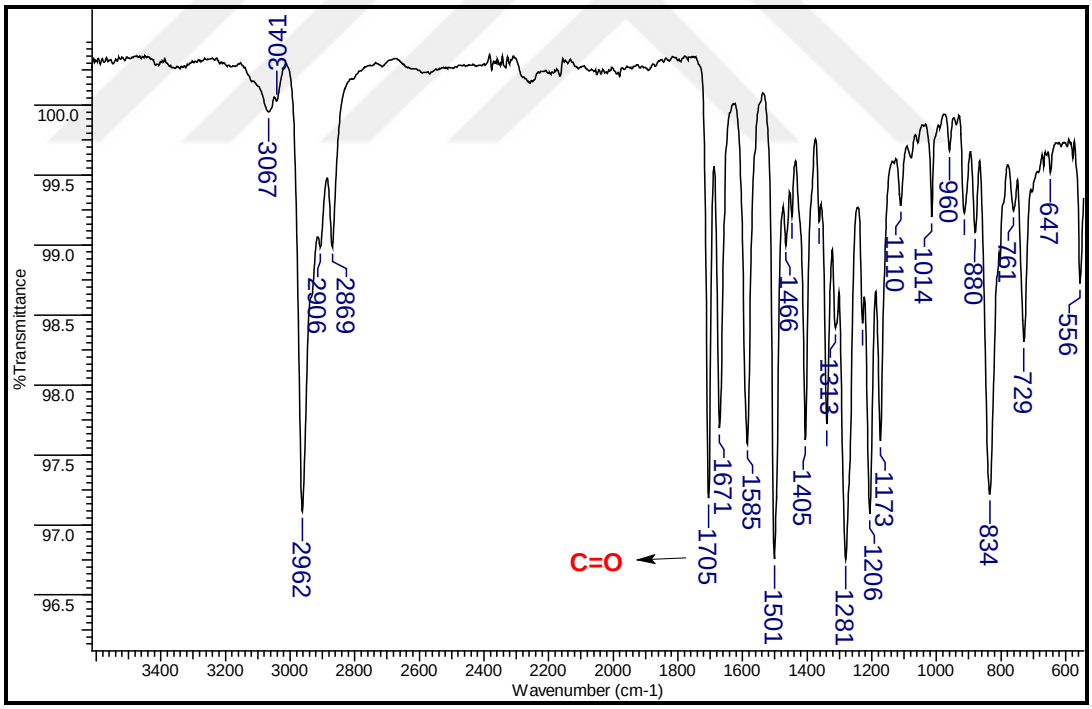

Figure 5.61: The FT-IR spectrum of compound 23.

The NMR analyses of complex were demonstrated in Figure 5.62 and 4.63. In the ^{1}H NMR spectrum of the compound, all the specific protons are numbered and depicted in the Figure 5.62. Aromatic protons of phenanthroline (9) come at lowest

field while protons of phenoxy sides (17,18) appear at the highest field of the spectrum. Aliphatic protons of the *i*-propyl groups resonate at 2.7 ppm as septet. Also the methyl protons of the compound come between 1.26-1.11 ppm. In addition, ^{13}C NMR of the spectrum confirms the structure. Aromatic carbons appear between 181-110 ppm while the rest of the carbons resonate between 34-24 ppm (Figure 5.63).

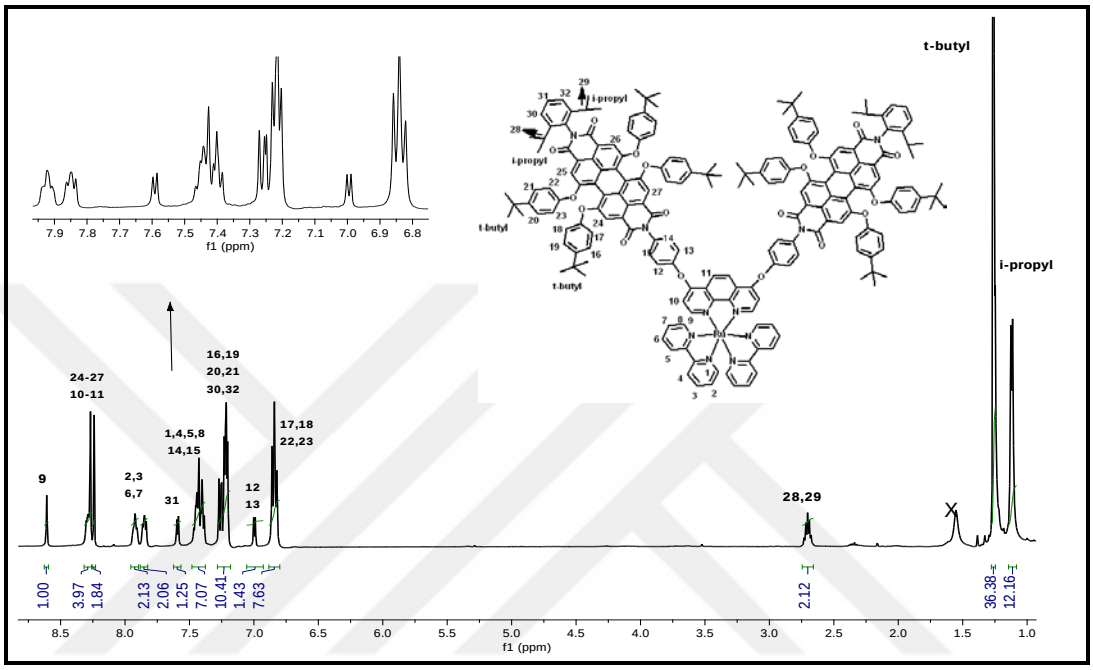

Figure 5.62: ^{1}H NMR spectrum of 23.

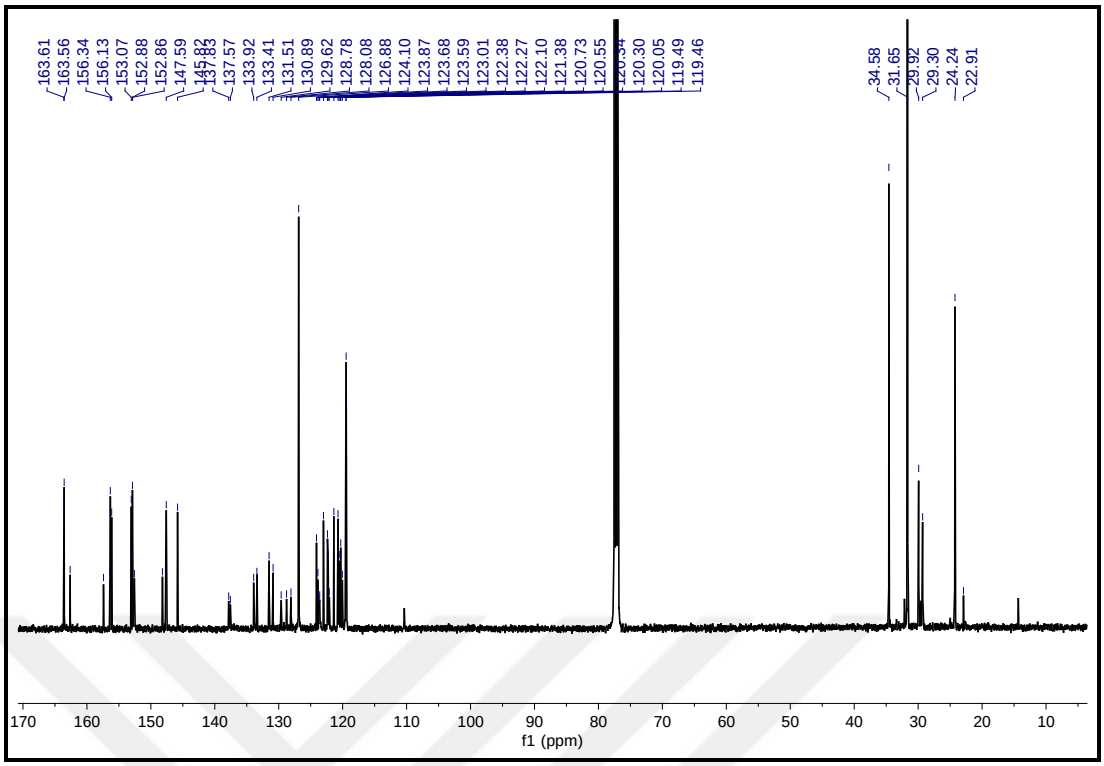

Figure 5.63: ^{13}C NMR spectrum of 23.

5.1.6.2.Synthesis and characterization of bis(perylenediimide) iridium(III) complex (24)

The synthesis of bis(perylenediimide) iridium(III) complex (**24**) was done by following the same method as synthesis of **23**. This is also a novel iridium complex bearing two perylene moieties in its core.

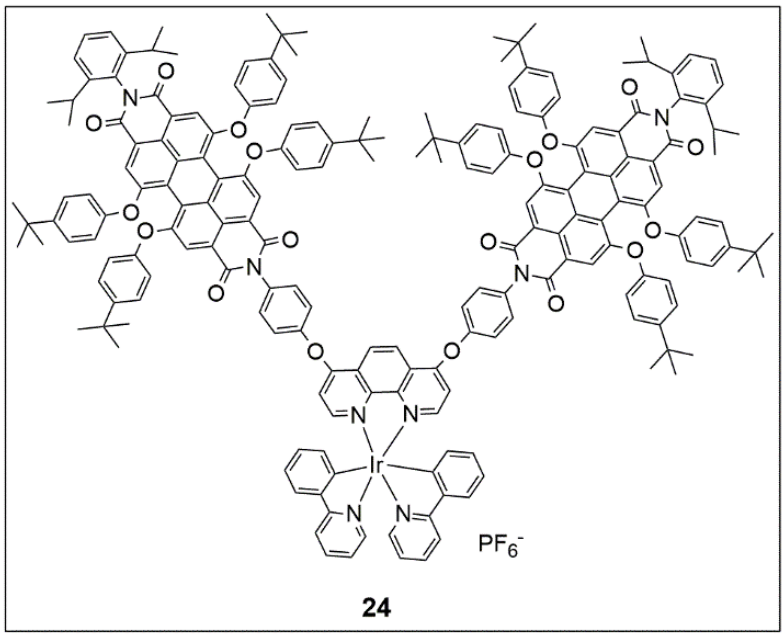

Figure 5.64: Molecular structure of 24.

The mass spectrum of the compound, clearly supports the molecular ion peak at 3148.77 that belongs to 3147 $[M\text{-}PF_6+H]^+$ (Figure 5.65). Also, in the FT-IR spectrum all necessary stretches are given in Figure 5.66. Especially the aliphatic peaks and C=O stretch supports the molecular structure as well.

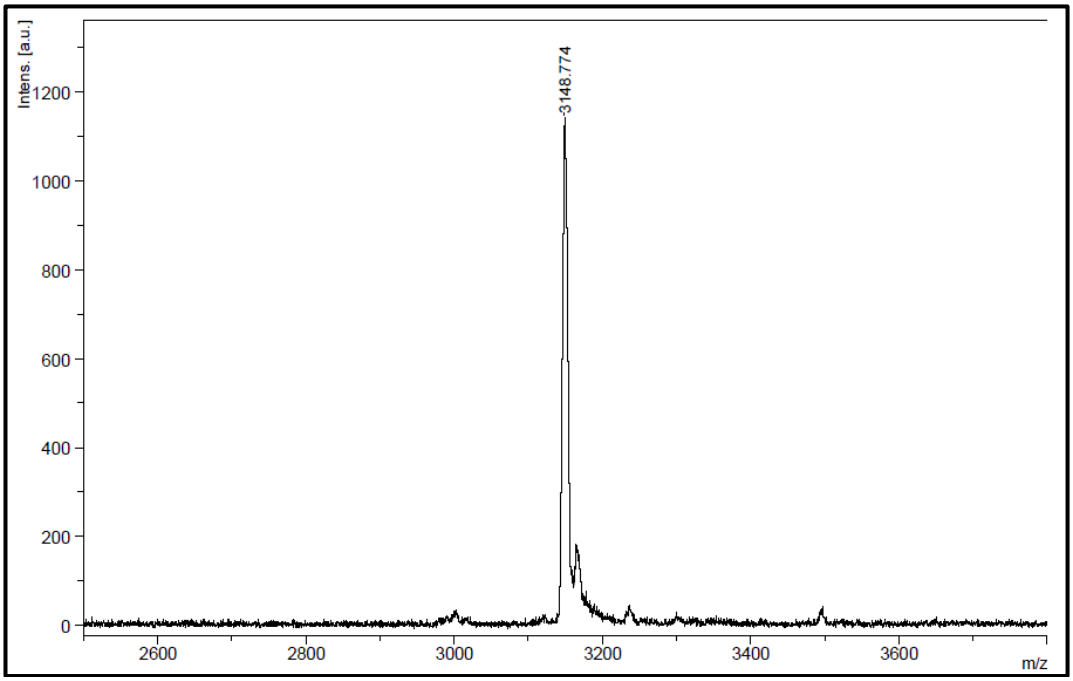

Figure 5.65: Mass spectrum of compound 24.

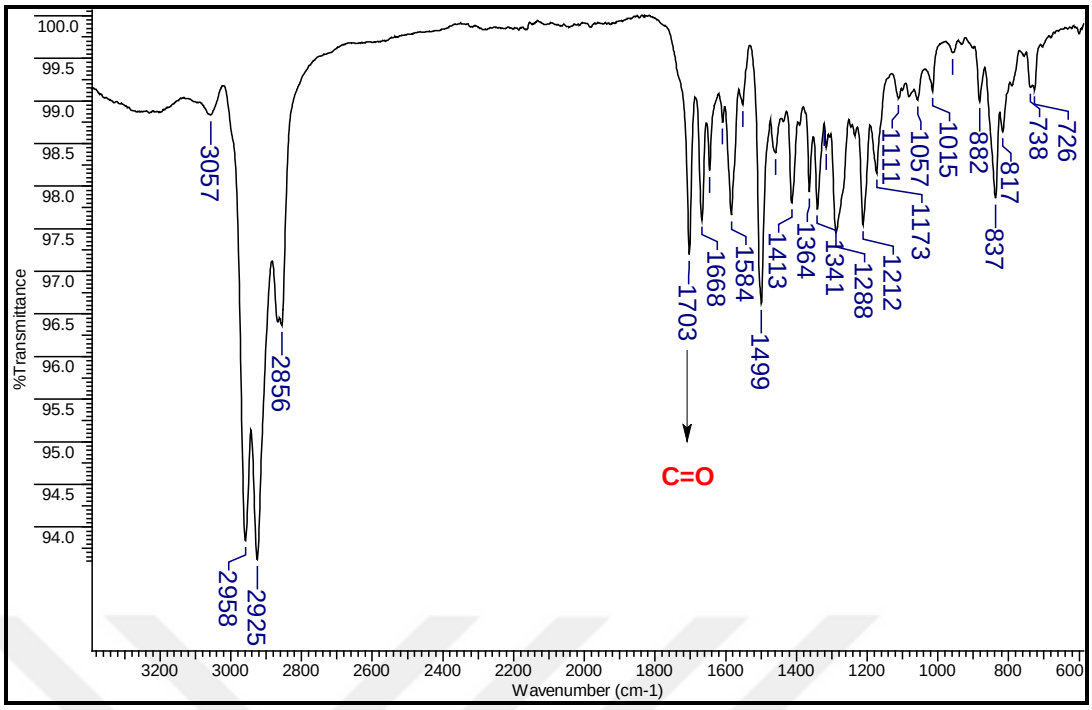

Figure 5.66: The FT-IR spectrum of compound 24.

The ^{1}H and ^{13}C NMR spectra of **24** are given in Figure 5.67 and 4.68. In the ^{1}H NMR spectrum of the compound, all the necessary protons are numbered and illustrated in the Figure 5.67. Aromatic protons of phenanthroline core come at lowest field. Other aromatic protons of the complex come between 8.25-6.75 ppm. Aliphatic protons of the *i*-propyl groups resonate at 2.7 ppm as septet whereas the methyl protons of the compound come between 1.27-1.11 ppm. Moreover, ^{13}C NMR of the spectrum supports the molecular structure. Aromatic carbons appear between 168-110 ppm while the aliphatic carbons resonate between 35-24 ppm (Figure 5.68).

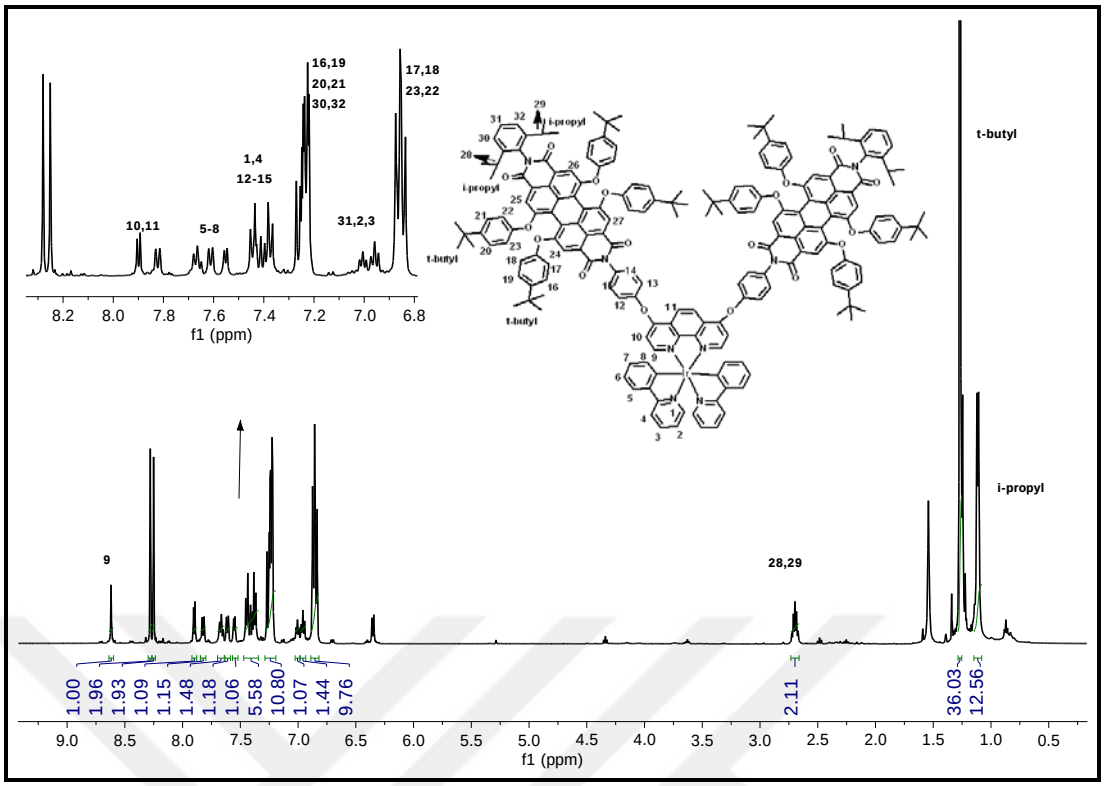

Figure 5.67: ^{1}H NMR spectrum of 24.

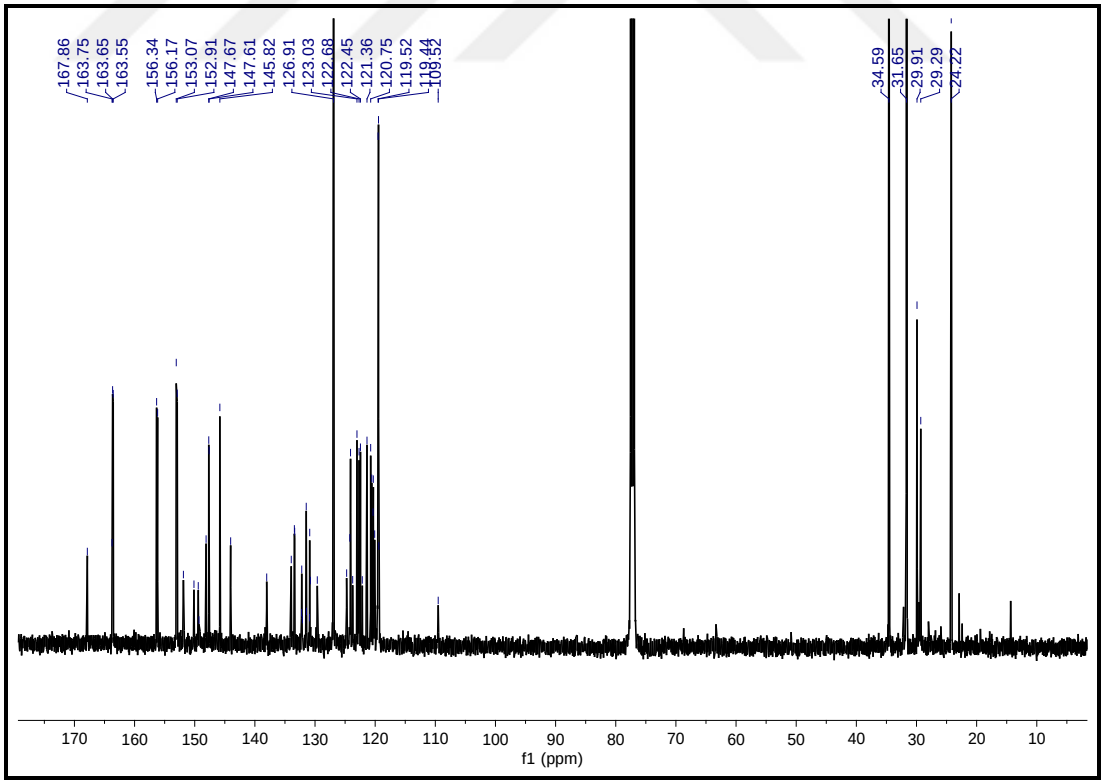

Figure 5.68: ^{13}C NMR spectrum of 24.

5.1.7. Synthesis and Characterization of Ruthenium and Iridium BODIPY Metal Complexes

5.1.7.1.Synthesis and characterization of BODIPY ruthenium(II) complex (25)

For the synthesis of the novel BODIPY ruthenium(II) complex (**25**) the nucleophilic substitution reaction was performed in the presence of K_2CO_3 in acetonitrile medium.

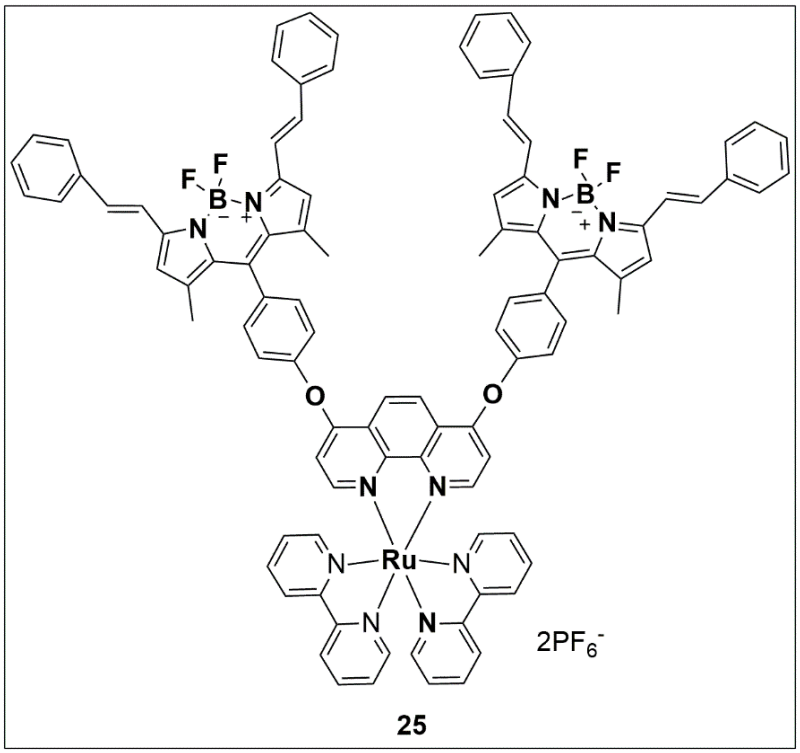

25

Figure 5.69: Molecular structure of 25.

According to the mass spectrum given in Figure 5.70, 1622 belongs to the molecular ion peak of 1622.35 $[M\text{-}2PF_6]^+$. Additionally, in the FT-IR spectrum of the compound **25**, all necessary aliphatic and other peaks are depicted in detail (Figure 5.71).

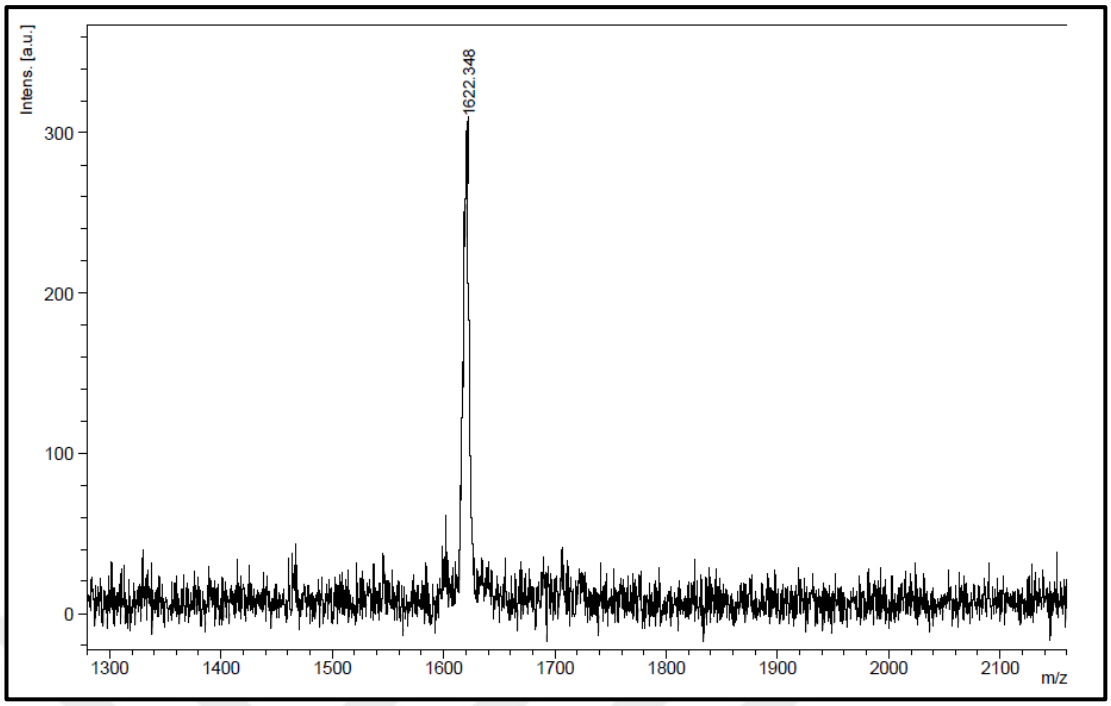

Figure 5.70: Mass spectrum of 25.

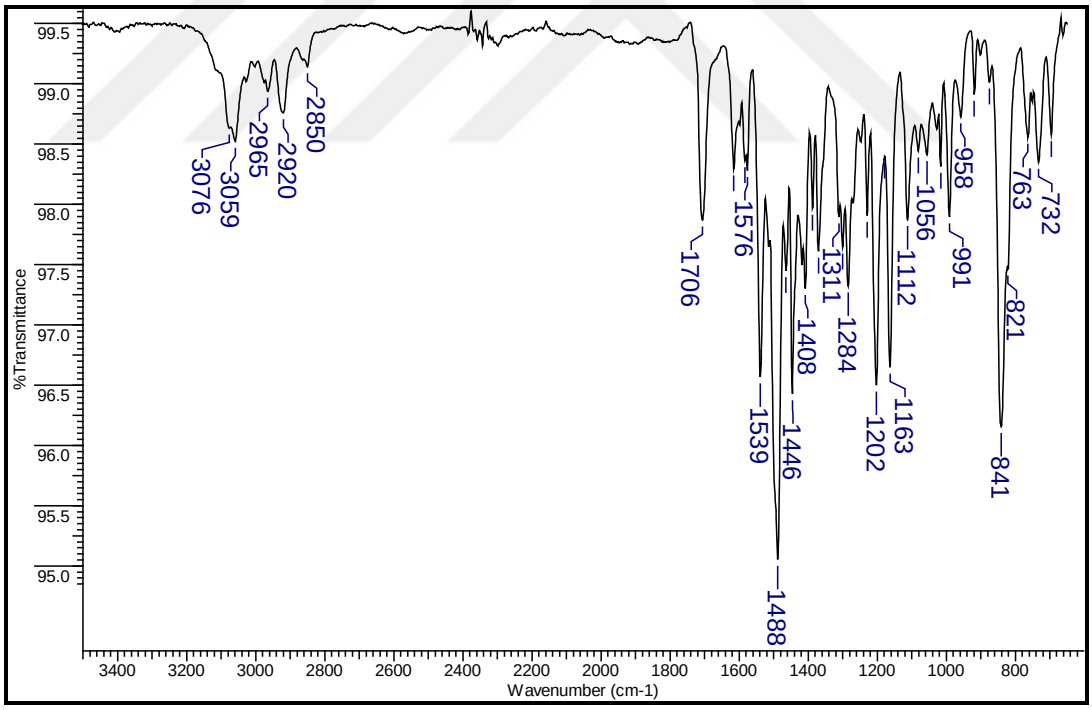

Figure 5.71: FT-IR Spectrum of 25.

^{1}H and ^{13}C NMR spectra of complex **25** are given in Figure 5.72 and 5.73, respectively. In the ^{1}H NMR spectrum of the compound, the aromatic protons appear between 8.3-6.9 ppm in the low field region (Figure 5.72). The specific protons of

phenanthroline core come at 8.8 ppm. Aromatic protons of BODIPY core come at 6.9 ppm as singlet. In the ^{13}C NMR spectrum of **25** aromatic carbons resonate between 174-110 ppm. Also, the methyl carbons of the BODIPY core are shown at 15.2 and 14.4 ppm (Figure 5.73).

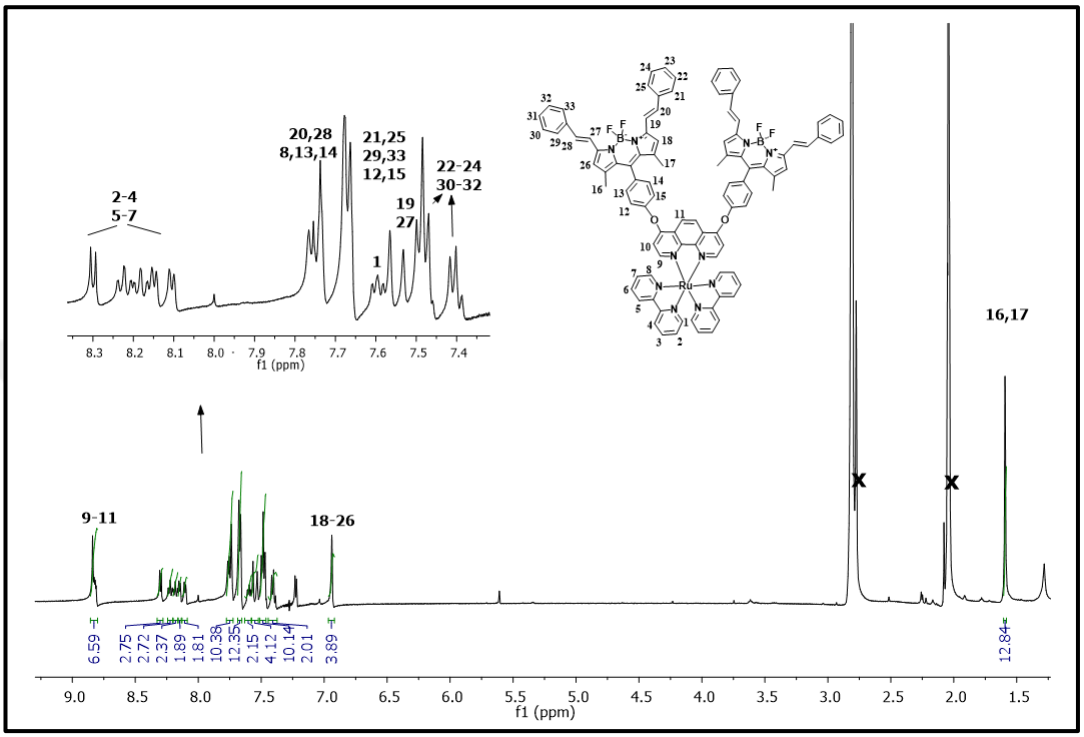

Figure 5.72: ^{1}H-NMR spectrum of 25.

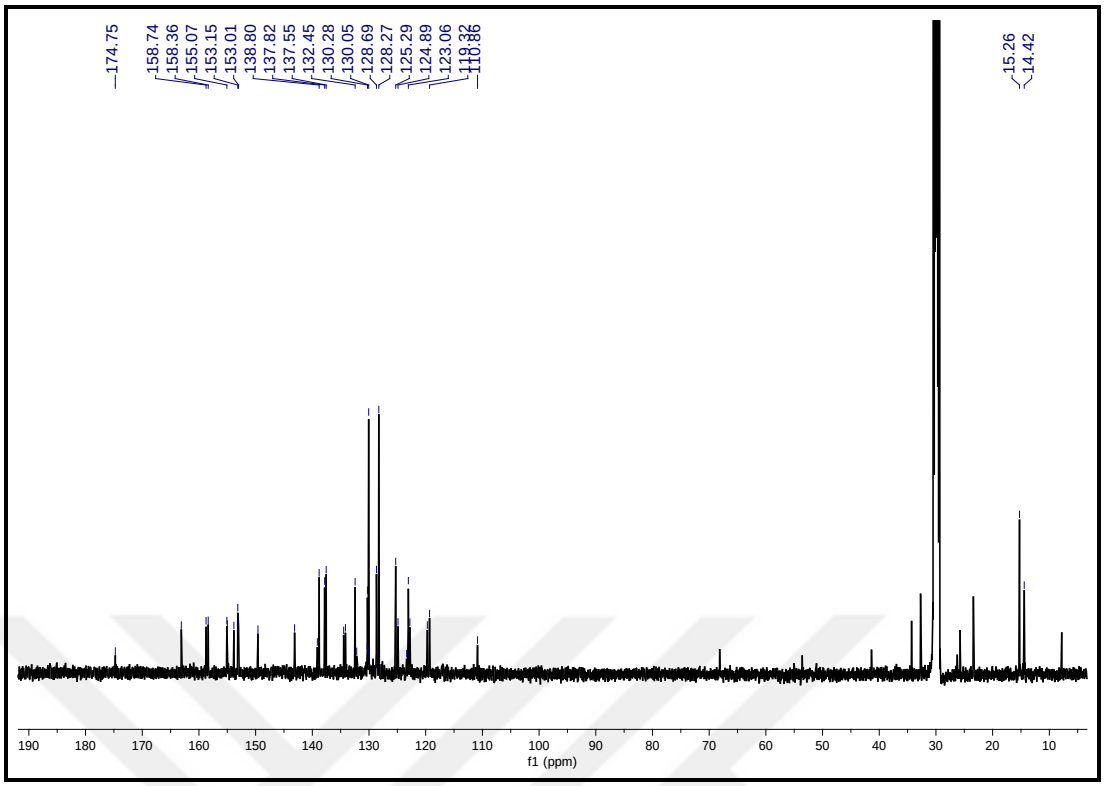

Figure 5.73: ^{13}C-NMR spectrum of 25.

5.1.7.2.Synthesis and characterization of BODIPY idirium(III) complex (26)

The synthesis of BODIPY iridium(III) complex (**26**) was performed by following the same procedure of synthesis of complex **25**.

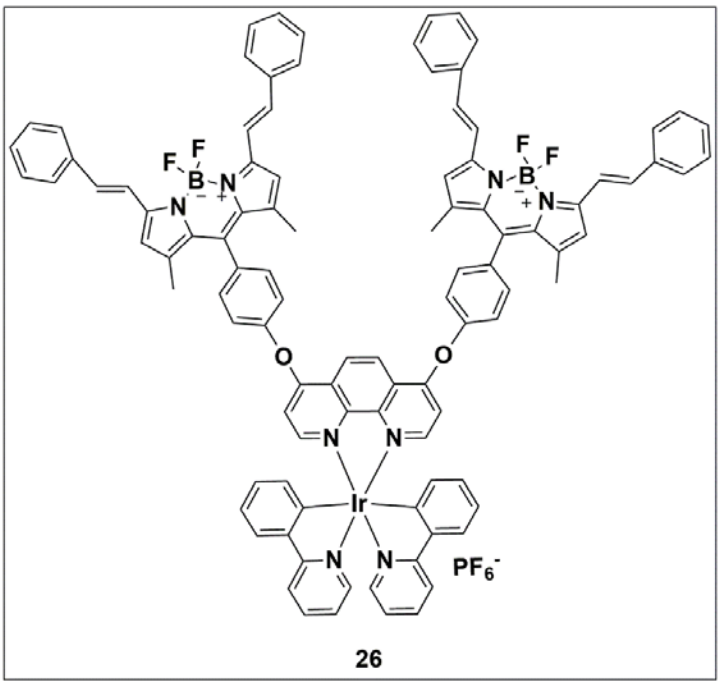

Figure 5.74: Molecular structure of 26.

In the mass spectrum given in Figure 5.75, the molecular ion peak 1709.14 represents $[M\text{-}PF_6]^+$. In addition to mass spectrum, in the FT-IR spectrum of **26**, all necessary peaks support the molecular structure (Figure 5.76).

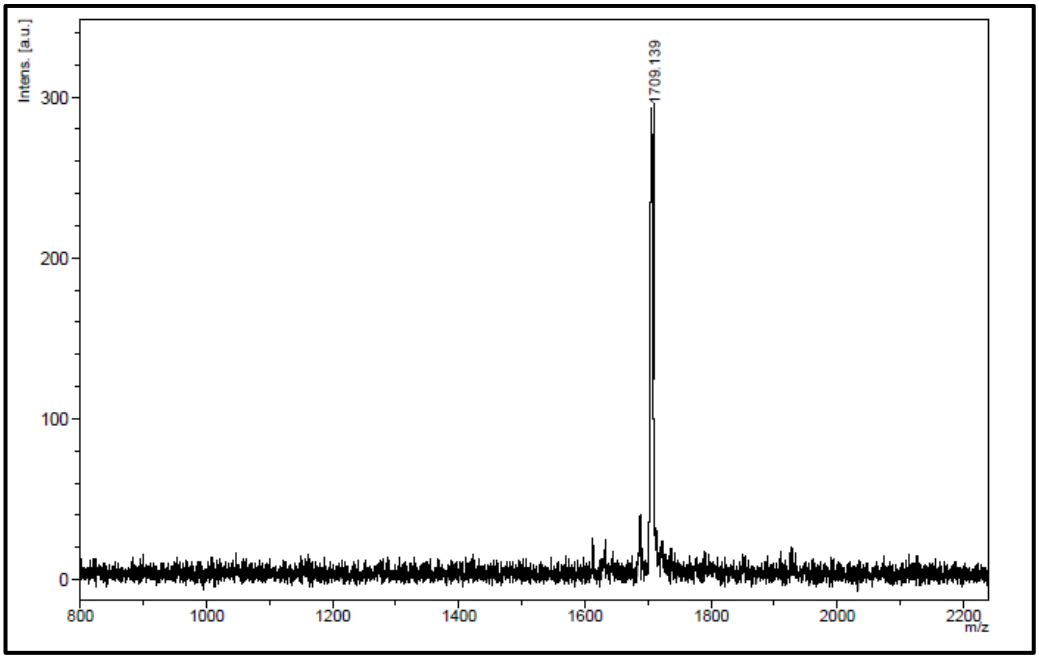

Figure 5.75: Mass spectrum of 26.

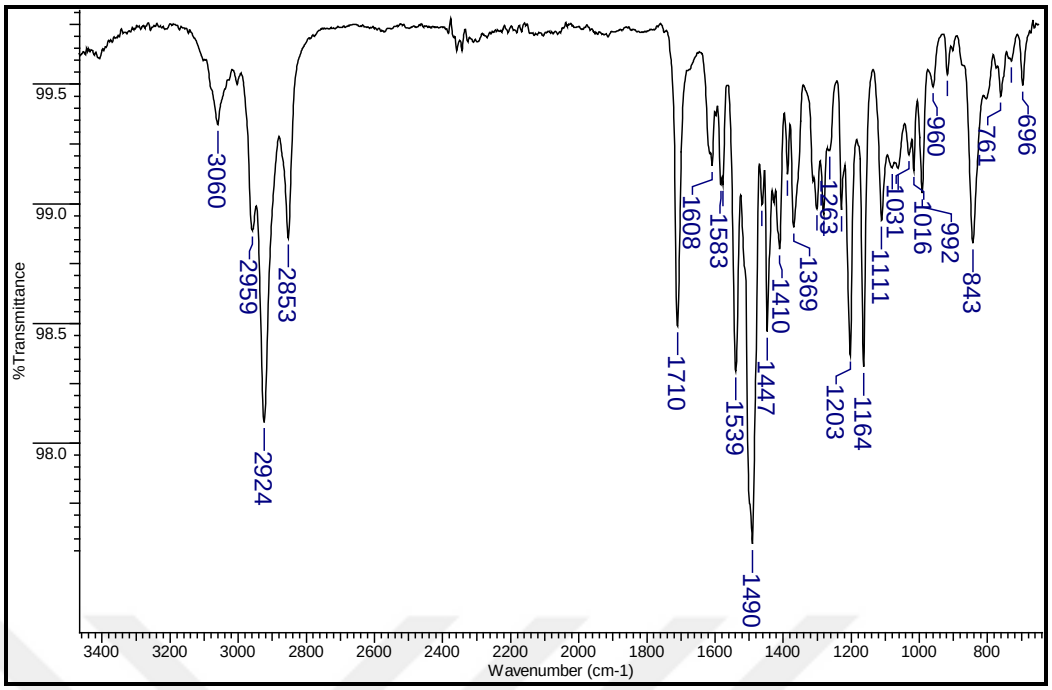

Figure 5.76: FT-IR Spectrum of 26.

The NMR spectra of complex **26** are given in Figure 5.77 and 4.58, respectively. The aromatic protons appear between 8.8-6.4 ppm in the ^{1}H NMR spectrum of the compound (Figure 5.77). Aromatic protons of phenanthroline core appear at the lowest field of the spectrum (8.83-8.24 ppm). Also, the methyl carbons of the BODIPY core are given at 1.62 ppm as singlet (Figure 5.77). In the ^{13}C NMR spectrum of **26** aromatic carbons resonate between 168-110 ppm and the methyl carbons of the BODIPY core are shown at 15.3 ppm (Figure 5.78).

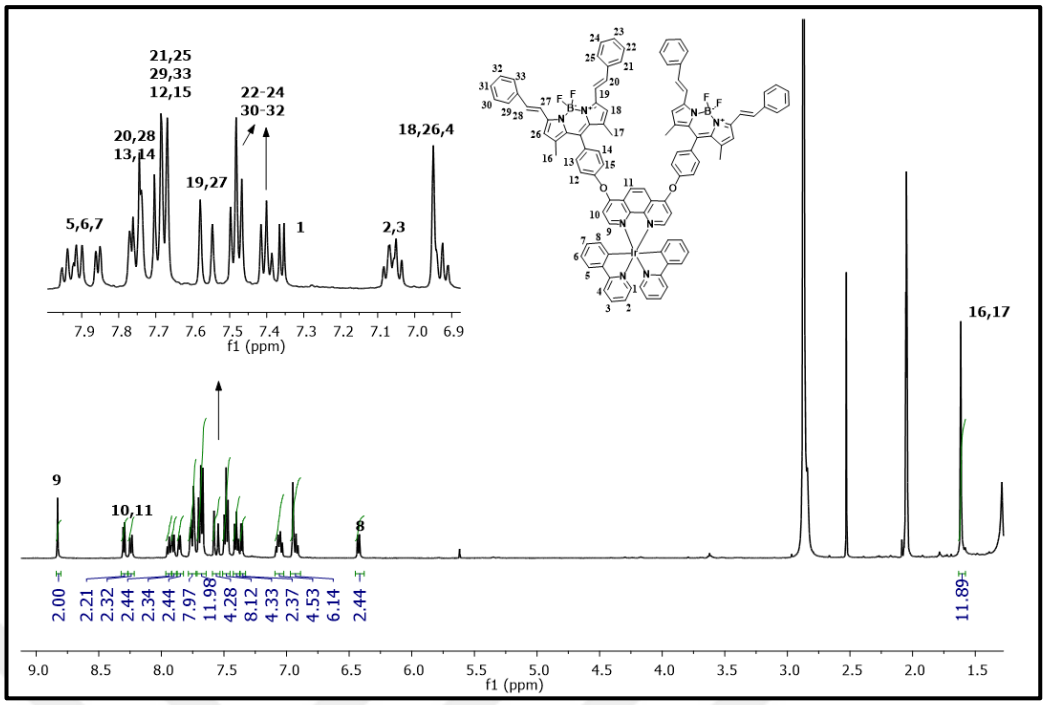

Figure 5.77: ^{1}H-NMR spectrum of 26.

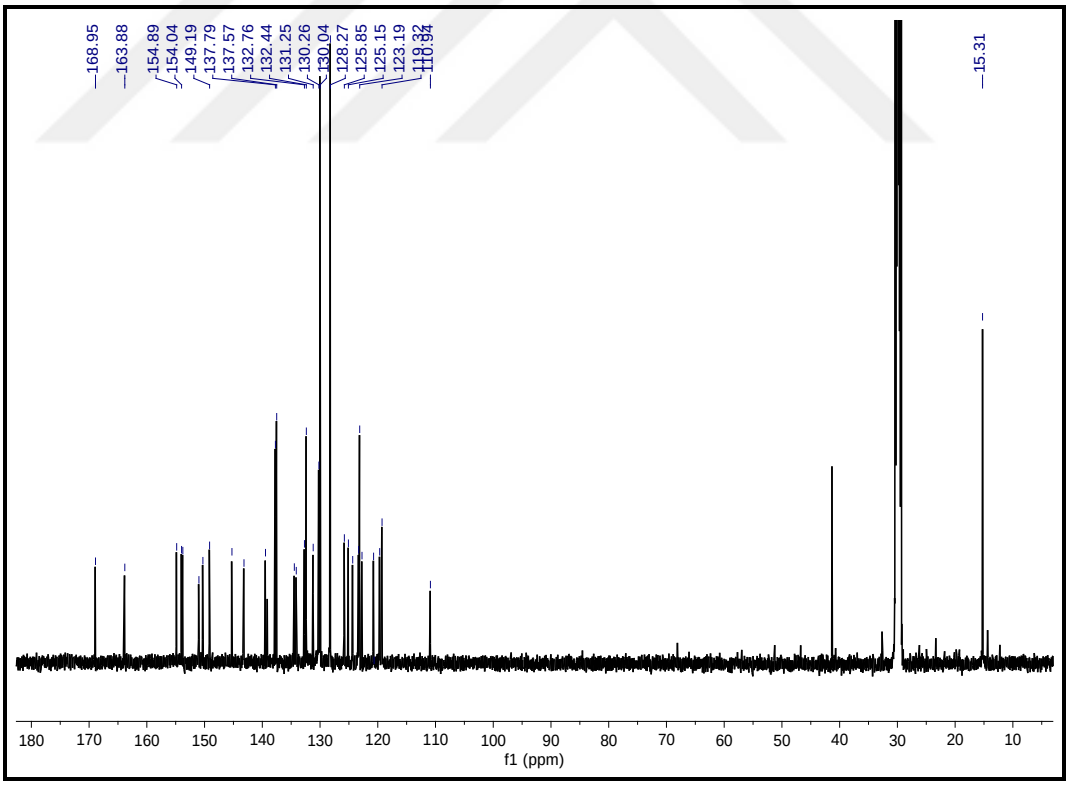

Figure 5.78: ^{13}C-NMR spectrum of 26.

5.1.8. Synthesis and characterization of benzimidazole-fused perylene ruthenium(II) complex (27)

The synthesis of benzimidazole-fused perylene ruthenium(II) complex (**27**) was performed in quinoline under argon atmosphere. The novel compound was characterized by mass, FT-IR and NMR spectrometry.

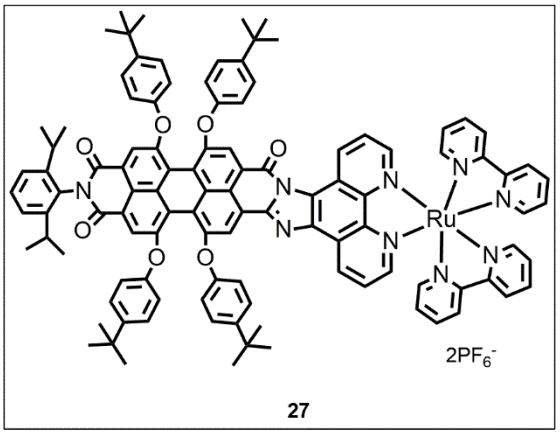

Figure 5.79: Molecular structure of 27.

According to the mass spectrum given in Figure 5.80, the molecular ion peak of the compound is seen at 1732.99 $[M\text{-}2PF_6]^+$. Other main peak, 1749, could be resulted from a fluorine atom addition to the molecule in the spectrum ($[M\text{-}2PF_6\text{+F-}2H]^+$). In the FT-IR spectrum of the complex **27**, all peaks are relevant and consistent with the structure (Figure 5.81). The disappearance of the anhydride C=O stretch at around 1770 cm^{-1} and the lack of NH_2 peak support the imidazole formation of the molecule clearly.

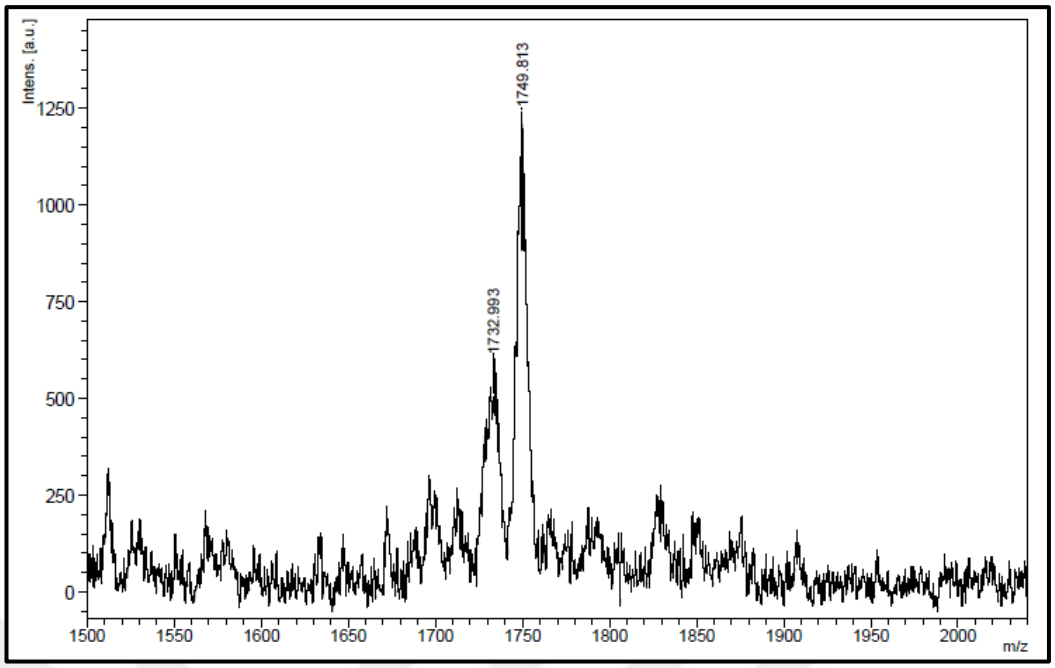

Figure 5.80: Mass spectrum of compound 27.

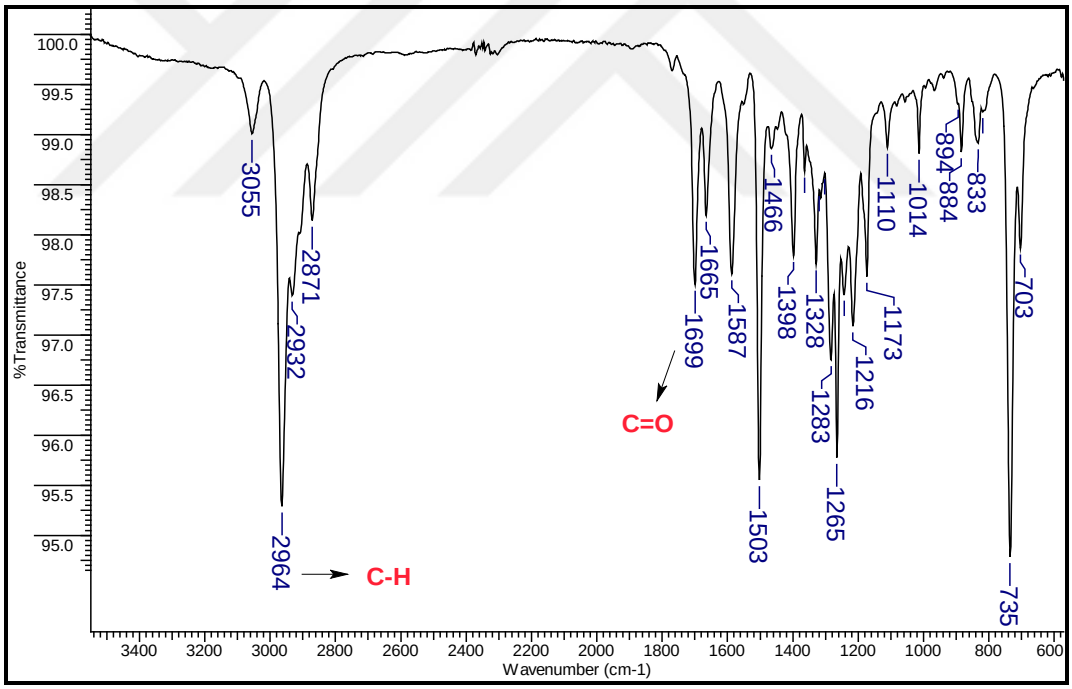

Figure 5.81: FT-IR spectrum of compound 27.

In the ^{1}H NMR of the spectrum aromatic peaks appear between 9.03-6.83 ppm (Figure 5.82). The specific protons are labelled in the spectrum, respectively. In Figure 5.83, ^{13}C NMR spectrum confirms all necessary carbon peaks of **27**. Aromatic carbons resonate between 163-114 ppm while aliphatic ones resonate between 52 and 7 ppm.

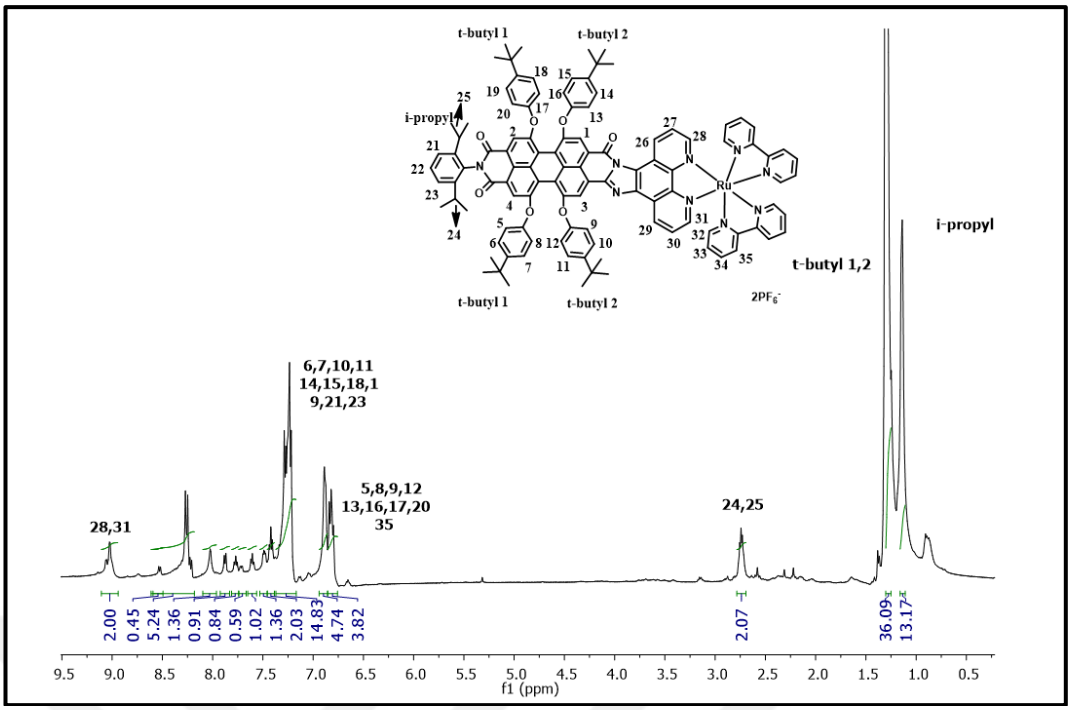

Figure 5.82: ^{1}H NMR spectrum of 27.

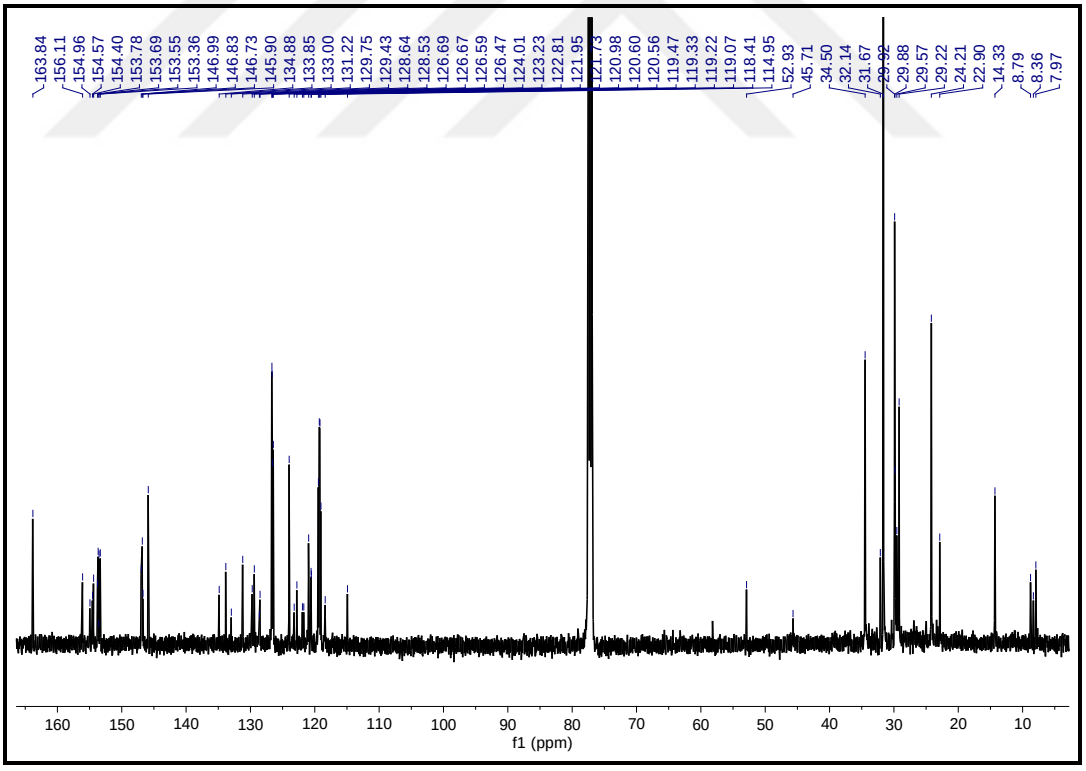

Figure 5.83: ^{13}C NMR spectrum of 27.

5.2. Photophysical Studies

5.2.1. Photophysical Studies of bis(perylenediimide) ruthenium(II) (23) and iridium (III) complex (24)

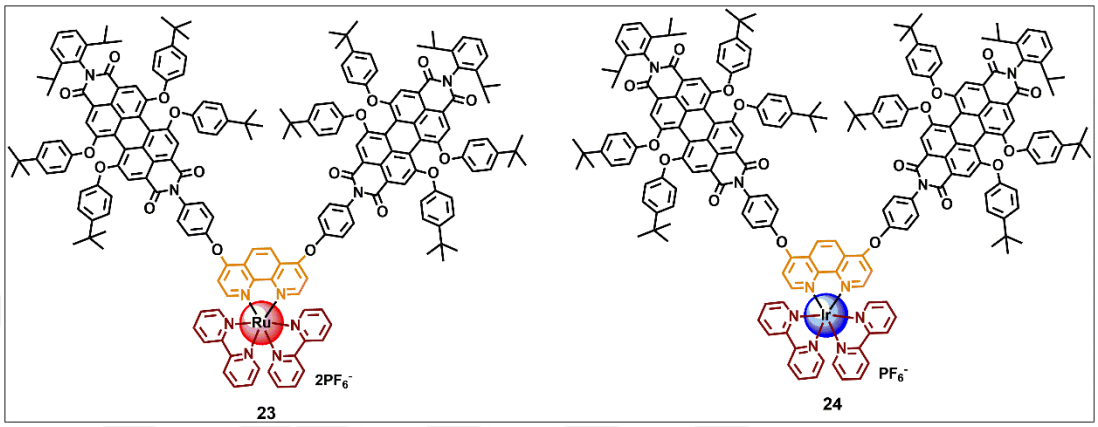

Figure 5.84: Molecular structures of 23 and 24.

Spectral characterization of **23** and **24** was performed with excitation, absorption and emission spectra at room temperature in dimethylsulphoxide (DMSO). The fluorescence emission, excitation and UV-vis absorption spectra of **23** and **24** are demonstrated in Figure 5.85. The emission behaviour of the compounds were investigated in (Table 5.5). In table 5.5, absorption maxima with molar extinction coefficients are shown. The spectra of **23** and **24** possess a equivalent profile bearing almost same maxima characteristics as expected. Ruthenium complex **23** have four maxima at 260, 285, 450 and 580 nm while iridium complex **24** bear three maxima observed at 265, 448 and 581 nm. Specific π- π* transition of PDI and MLCT transitions that has an expected overlap came between 440 and 590 nm. Also, the ground state absorption spectra of **23** and **24** were also studied at different concentrations (Figure 5.86). The emission behaviour of **23** and **24** were almost same, and the emission maxima were found at 615 and 616 nm. The excitation spectra were similar with related absorption spectra for both of the compounds. The absorption and excitation spectra were mirror image of the fluorescence emission spectra. The Stoke's shift was as 33 nm for **23** and 35 nm for **24** and. The fluorescence lifetimes (τ_F) of **23** and **24** was recorded in DMSO using the time correlated single photon counting

(TCSPC) technique in DMSO. The lifetimes were measured as 1.04, 5.65 ns for **23** and 2.81 ns for **24**. The absorption and emission characteristics of **23** and **24** are appropriate for application in *vivo* and deeper penetration in tissue [89], [90].

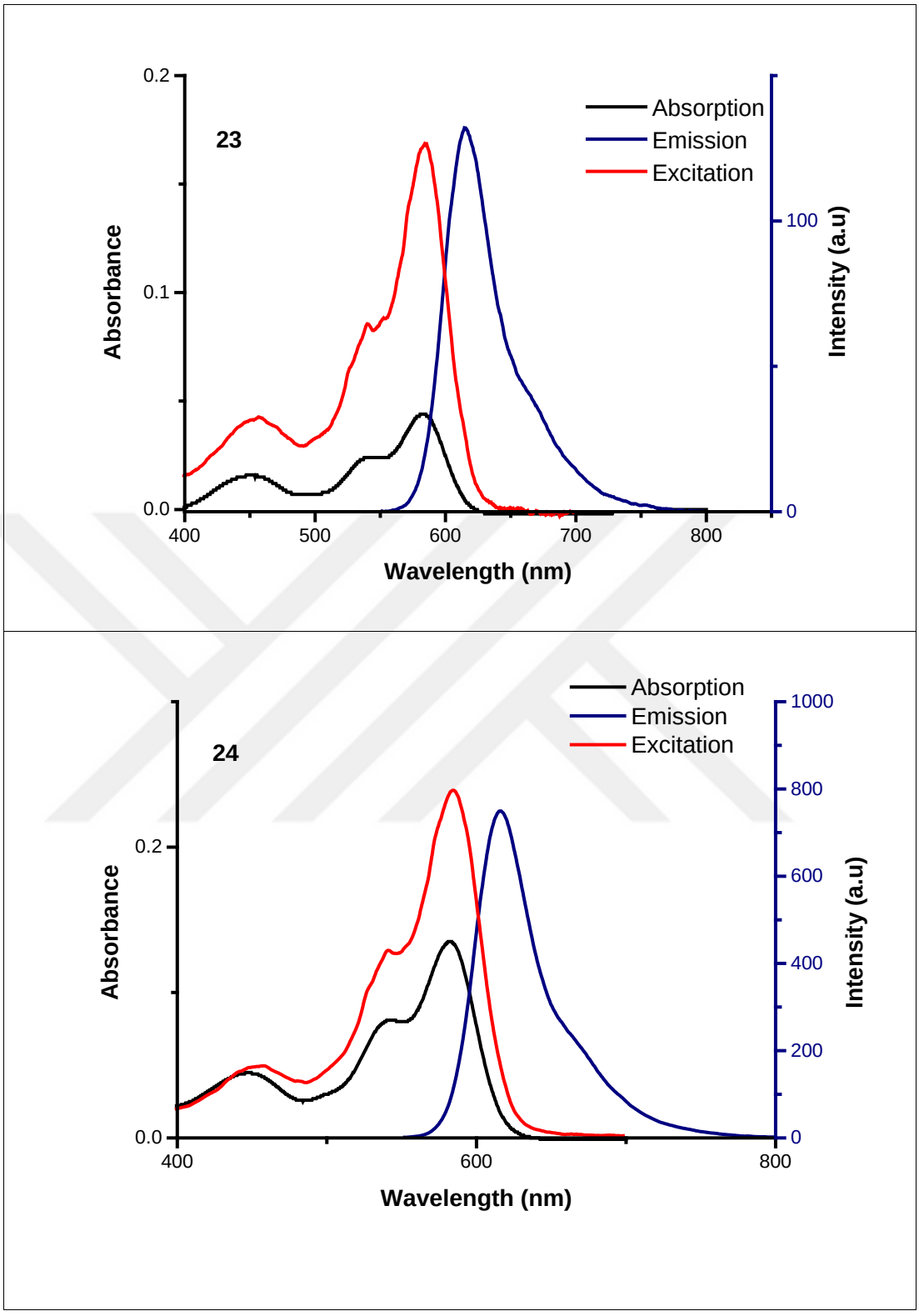

Figure 5.85: UV-vis, fluorescence emission and excitation spectra of 23 and 24 in DMSO (2.0 µM).

Table 5.5: Photophysical properties of 23 and 24 [a].

Compound	λ_{ab}, nm (Log ε^{b})	λ_{em}, nm	τ_F (ns)[c]
23	264 (8.12), 290 (8.16), 451 (8.35), 582 (8.46)	615	1.04 (23.6 %) 5.65 (76.4 %) (CHISQ = 0.9366626)
24	265 (8.12), 448 (8.35), 581 (8.46)	616	2.81 (CHISQ=2.167815)

[a]Dimethylsulphoxide [b]Molar extinction coefficients [c] Lifetime

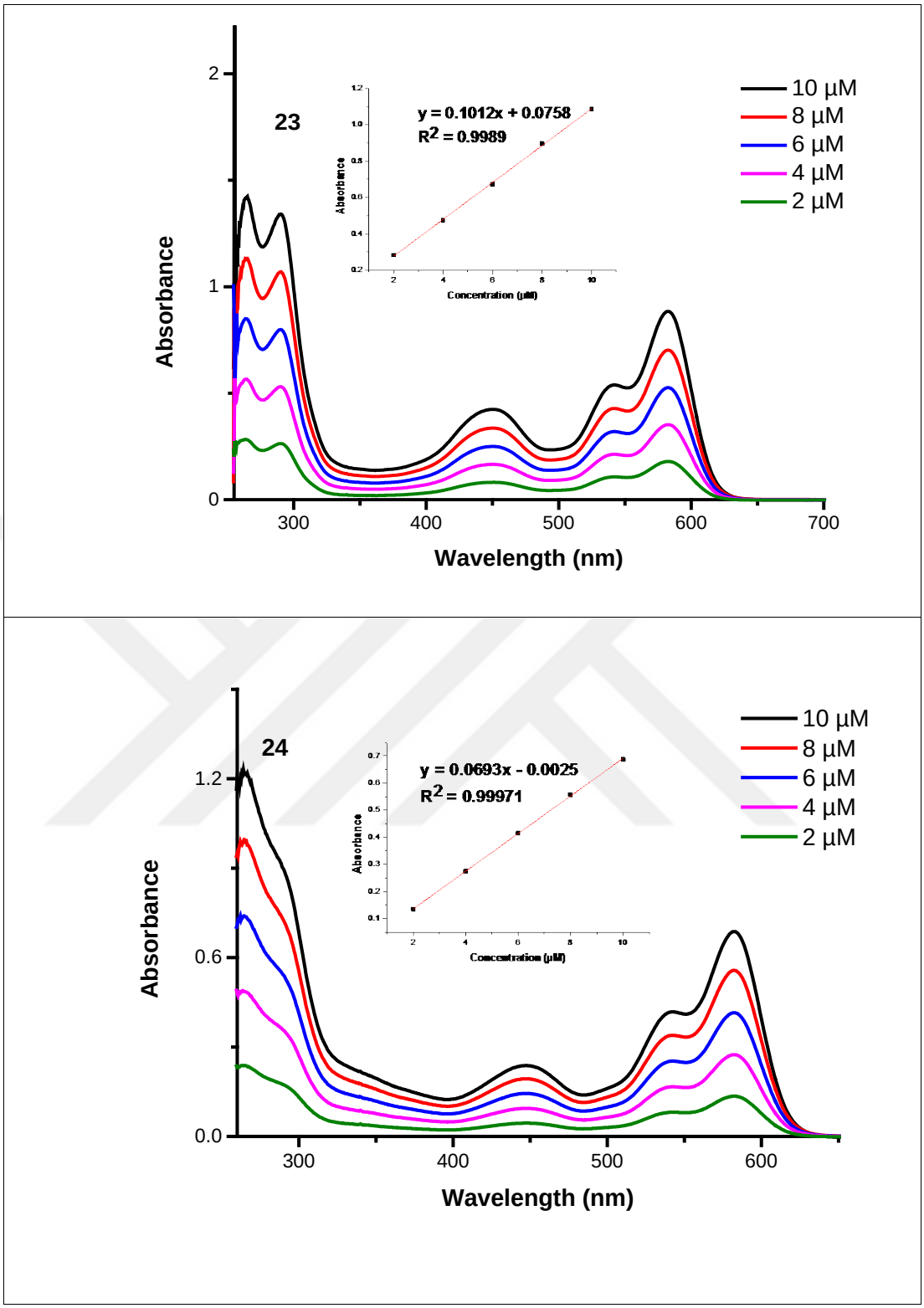

Figure 5.86: UV-vis spectra of 23 and 24 in DMSO at different concentrations between $2x10^{-6}$ M and 10^{-5} M.

5.2.2. Photophysical Studies of BODIPY ruthenium(II) (25) and iridium(III) complex (26)

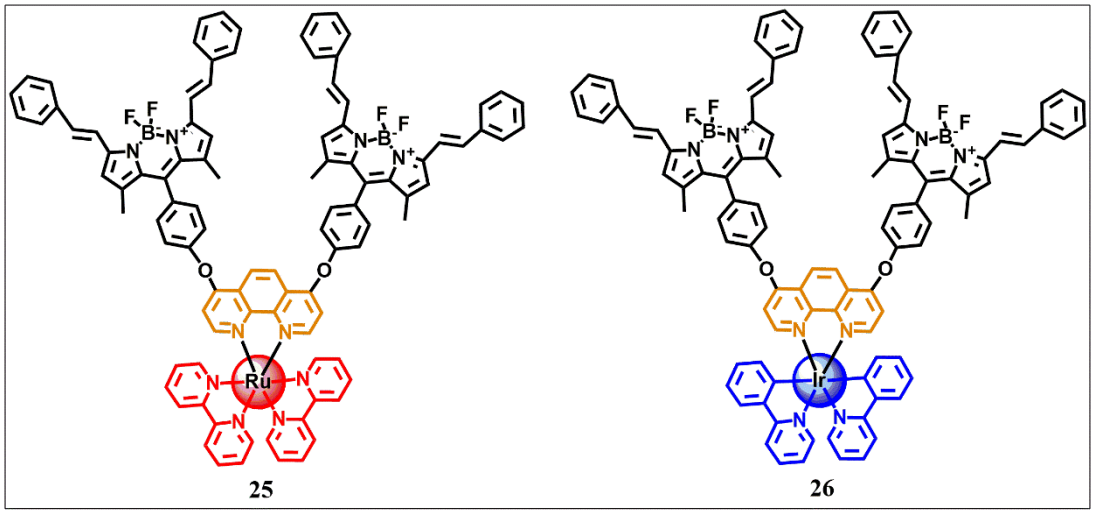

Figure 5.87: Molecular structures of 25 and 26.

Photophysical study of **25** and **26** were performed with absorption, emission and excitation spectra in DMSO at room temperature. The UV-vis absorption and fluorescence emission spectra of both novel molecules are shown in Figure 5.88. The characteristic absorption bands of **25** and **26** were detected at 629 nm, that belongs to the S_0-S_1 transition [91]. The complexes also exhibited two main bands at 350, 575 nm. The fluorescence emission spectra of the molecules recorded in DMSO at room temperature and the outcome are shown in Table 5.6. The emission analyses of **25** and **26** shown a similar profile having a maximum at 642 nm. Additionally, the excitation spectra of compounds were recorded in DMSO. For both of the compounds, excitation/absorption spectra and fluorescence emission spectra are mirror images (Figure 5.88). The Stokes shifts are founds as 11 nm and 12 nm for **25** and **26**, respectively.

Using the time correlated single photon counting (TCSPC) technique, the fluorescence lifetimes (tF) of **25** and **26** were studied in DMSO. The lifetimes were found as 4.72 and 4.70 ns for **25** and **26**.

The ground state absorption spectra of **25** and **26** were recorded in various concentrations in order to calculate molar extinction coefficient (ε) (Figure 5.89). The value of **25** was observed as 19.71×10^4 $M^{-1}cm^{-1}$, while the values of **26** is 19.49×10^4

$M^{-1}cm^{-1}$. Since high molar extinction coefficient of the PS is important, the value of **25** and **26** are higher when compared to literature examples [92], [93].

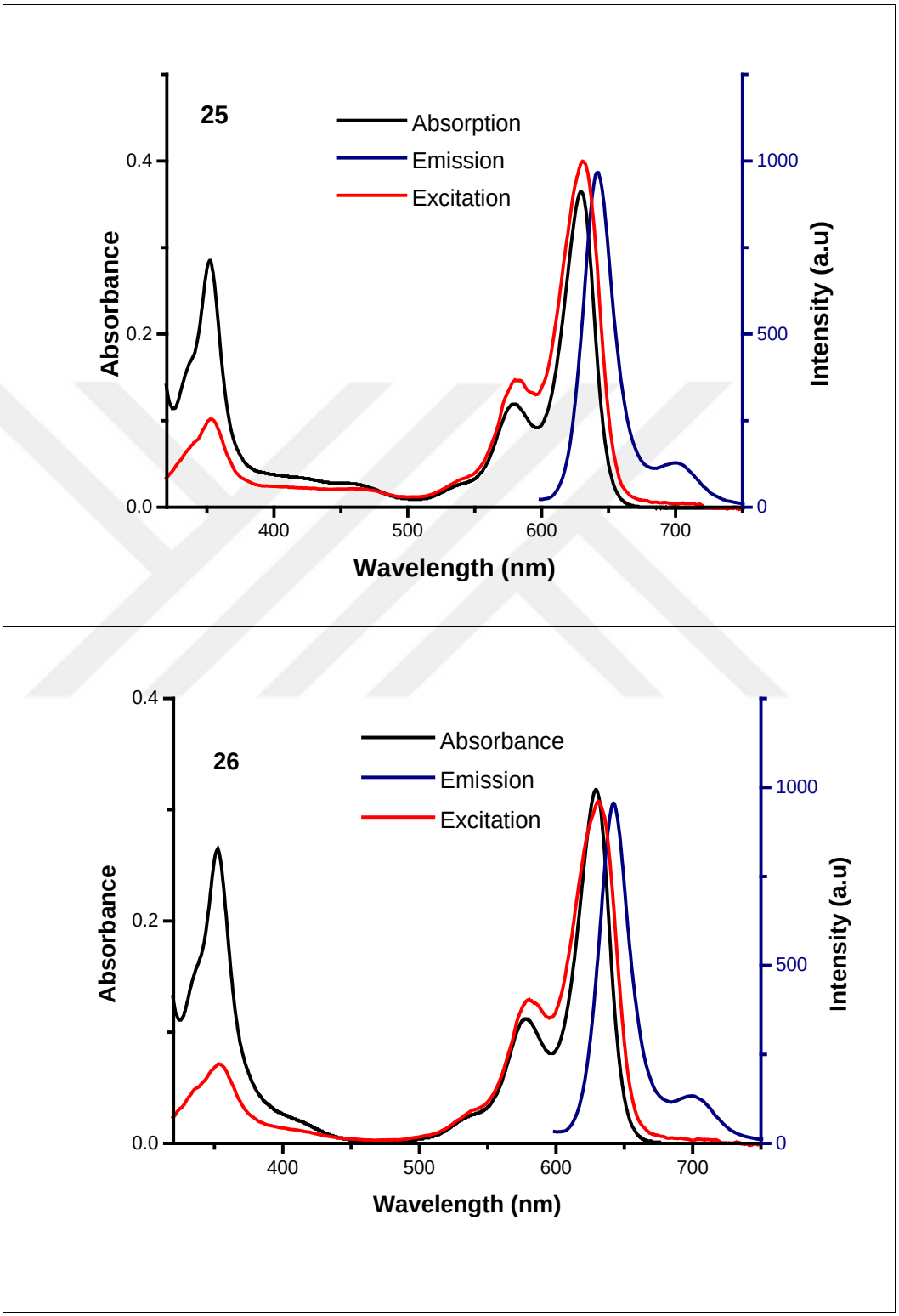

Figure 5.88: UV-vis, fluorescence emission and excitation spectra of 25 (0.5 μM) and 26 (0.5 μM) in DMSO.

Table 5.6: Photophysical properties of 25 and 26[a].

Compound	**λ_{ab}, nm (ε^{b}, 10^4 $M^{-1}cm^{-1}$)**	**λ_{em}, nm**	**τ_F (ns)[c]**
25	352, 579, 629 (19.71)	642	4.72 (CHISQ=1.28079)
26	352, 577, 629 (19.49)	642	4.70)

[a] Dimethylsulphoxide. [b] Molar extinction coefficients. [c] Lifetime.

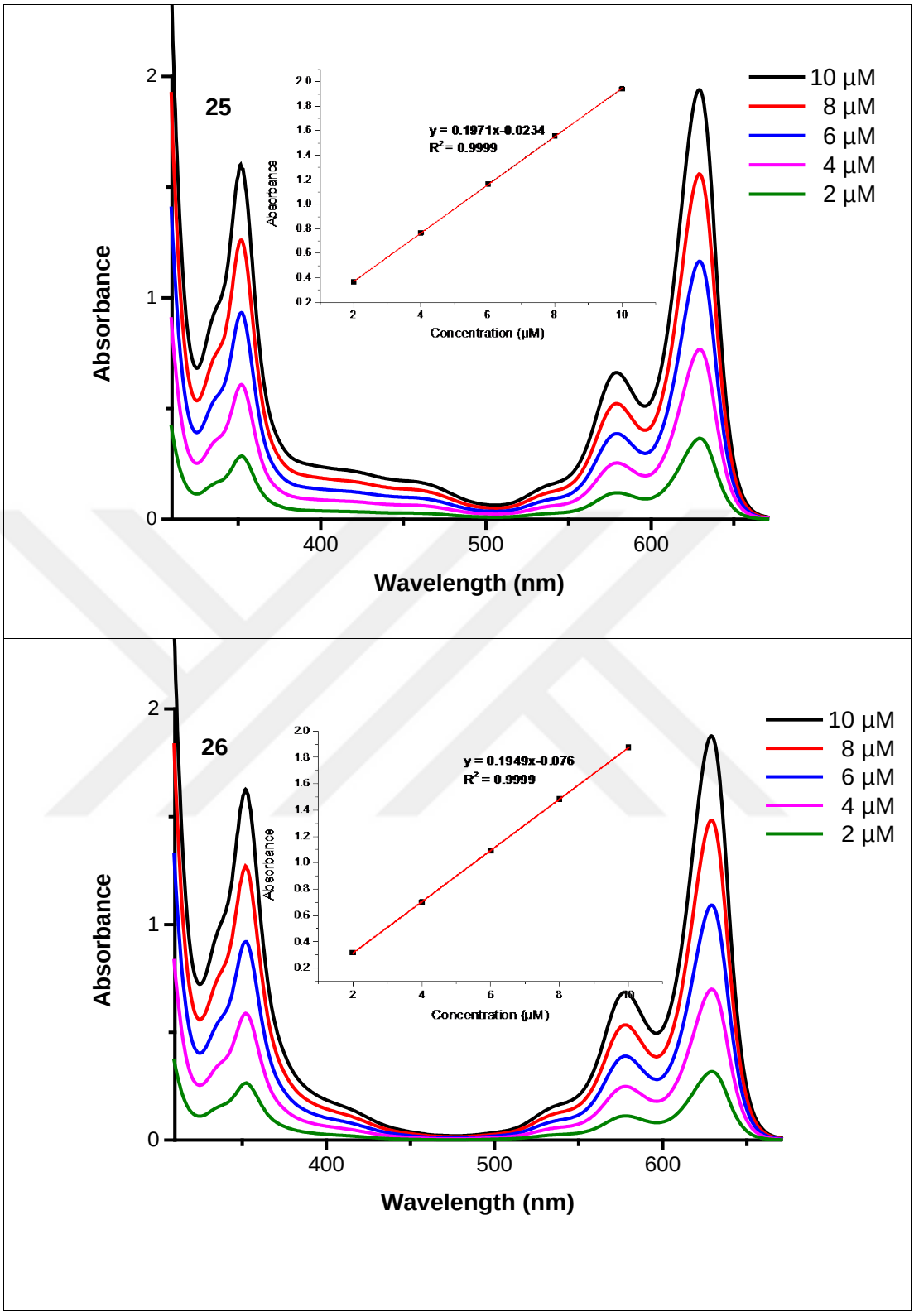

Figure 5.89: UV-vis spectra of 25 and 26 in DMSO at different concentrations between 2.5×10^{-6} M and 0.5×10^{-6} M.

5.2.3. Photophysical Studies of benzimidazole-fused perylene ruthenium(II) complex (27)

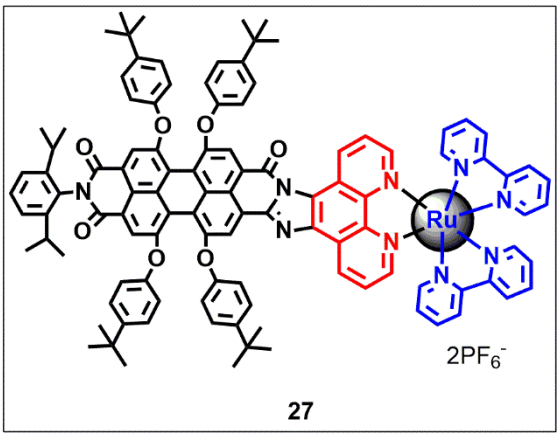

Figure 5.90: Molecular structure of 27.

Photophysical investigations of **27** was performed with absorption, excitation and emission spectra in dichloromethane (DCM) at room temperature. The UV-vis absorption, fluorescence emission and excitation spectra of **27** is depicted in Figure 5.91 and the emission properties of the complexes were recorded in DMSO at room temperature (Table 5.7). Absorption maxima of the compound **27** are depicted in Table 5.7 with molar extinction coefficients. The spectra of **27** has three maxima observed approximately at 277, 426, 548 nm and also a shoulder at 515 nm. When compared to compounds **23** and **24**, the absorption maxima of the benzimidazole bridged complex **27** showed a blue shift in the spectrum. Additionally, the ground state absorption spectra of **27** was also recorded at different concentrations (Figure 5.92). The emission maxima of **27** was found as 596 nm and the absorption and spectra excitation were mirror image of its fluorescence emission spectra. The fluorescence lifetime (τ_F) of **27** was found using the time correlated single photon counting (TCSPC) technique in DCM and it was found to be 6.85 ns (Table 5.7).

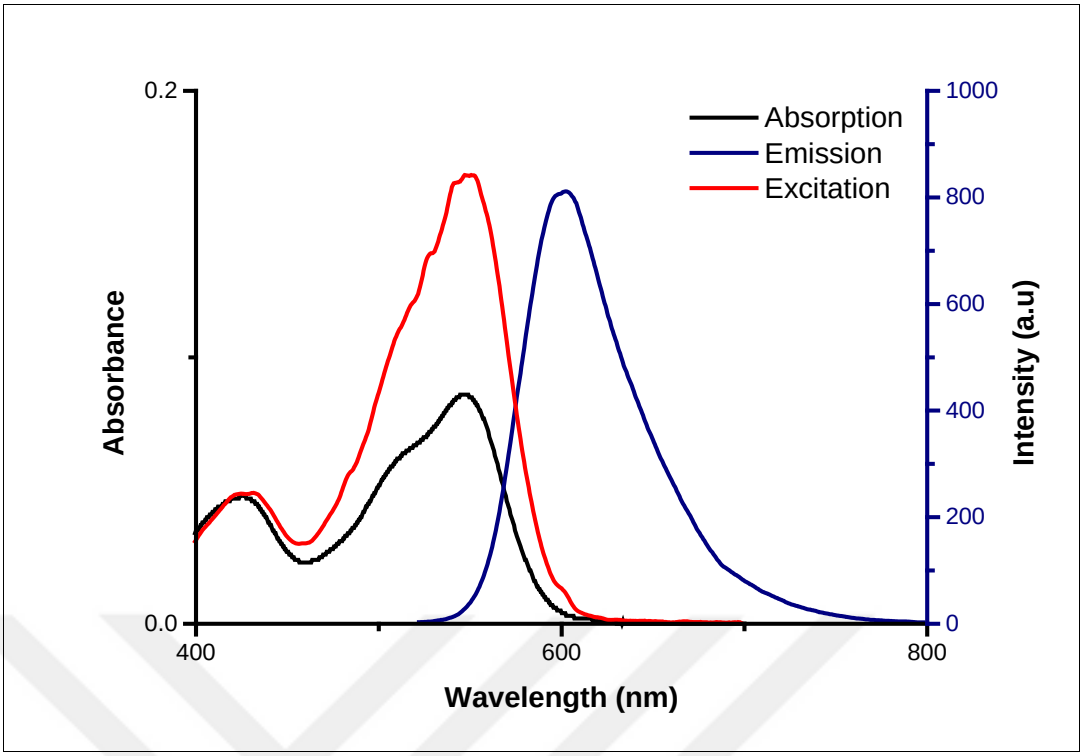

Figure 5.91: UV-vis, fluorescence emission and excitation spectra of 27 in DCM (2 μM).

Table 5.7: Photophysical properties of 27[a].

Compound	**λ_{ab}, nm (Log ε^{b})**	**λ_{em}, nm**	**τ_F (ns)[c]**
27	277 (8.14), 426 (8.33), 548 (8.44)	600	6.85 (CHISQ = 1.120579)

[a] dichloromethane [b] Molar extinction coefficients [c] Lifetime

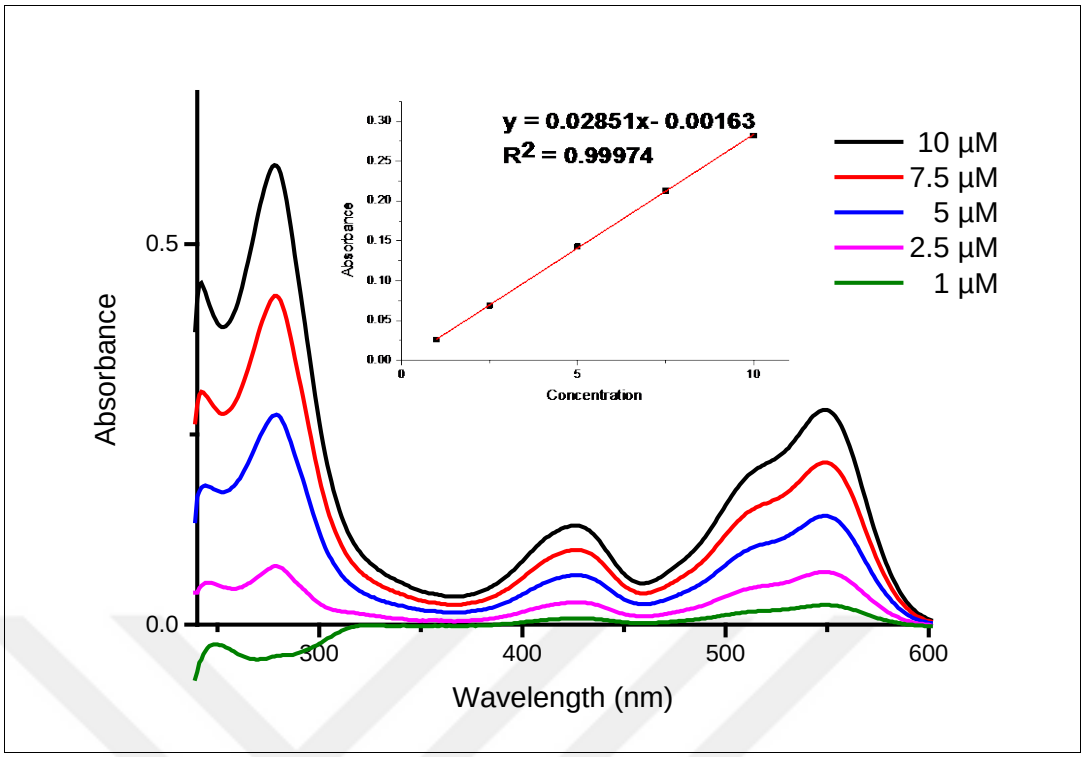

Figure 5.92: UV-vis spectra of 27 in DCM at different concentrations between $1x10^{-6}$ M and 10^{-5} M.

5.3. Photochemical Studies

5.3.1. Singlet oxygen generation study of bis(perylenediimide) ruthenium(II) complex (23)

5.3.1.1.Singlet oxygen measurements

The type II PDT mechanism includes energy transfer from triplet state of the photosensitizers to molecular oxygen in order to produce singlet oxygen ($^1O_2$) that harm biomolecules to initiate cell death [94]. In order to apply PDT at the molecular level, examining the generation of $^1O_2$ is highly critical. In this thesis, singlet oxygen production potential of novel bis(perylenediimide) ruthenium (II) complex (**23**) was investigated in DMSO with diphenylisobenzofuran (DBPF), singlet oxygen trap molecule. Compound **23** (2.0 µM) and DPBF (35.0 µM) was held for 20 min in the dark to remove possible inputs to the absorbance signal of DPBF from dark reactions.

As a reactions in the dark, absorption band of DPBF at 414 nm did not exhibit any change. The solution of the **23** and DPBF was treated with red light (λ= 632 nm, 2.5 mW /cm^2) over a time period 0 to 24.0 min. The gradual photo-induced generation of singlet oxygen of **23** decrease was observed as absorption intensity of DPBF (Figure 5.93). The change in absorption of the trap molecule at 414 nm versus irradiation time graph was plotted using the obtained data for **23** (Figure 5.94). Singlet oxygen determination of the reference molecule, methylene blue, was also carried out under the same conditions (Fig. 4.94). Singlet oxygen quantum yield (Φ_Δ) of the **23** and the free ligand **20** were found according to the literature [95]. According to the final results, the singlet oxygen quantum yield of **23** (Φ_Δ=0.30) is thirty times higher than the ligand **20** (Φ_Δ=0.01). Heavy atom effect, a common way of increasing the intersystem crossing (ISC) ability of the chromophore, may be accepted as the reason of the significant increase of the Φ_Δ [96]. According to the results, singlet oxygen generation showed good efficiency compared with the previous examples having ruthenium(II) or ruthenium perylene photosensitisers [30], [60]. The photostability of compound **23** is also significant and desirable upon repetitive excitation in PDT studies. Compound **23** without DPBF were kept under light for 20 min and there observed no change was in the absorption band of compound in the red region of the spectrum (Figure 5.95). It is clear that, this complex is stable under the singlet oxygen study conditions.

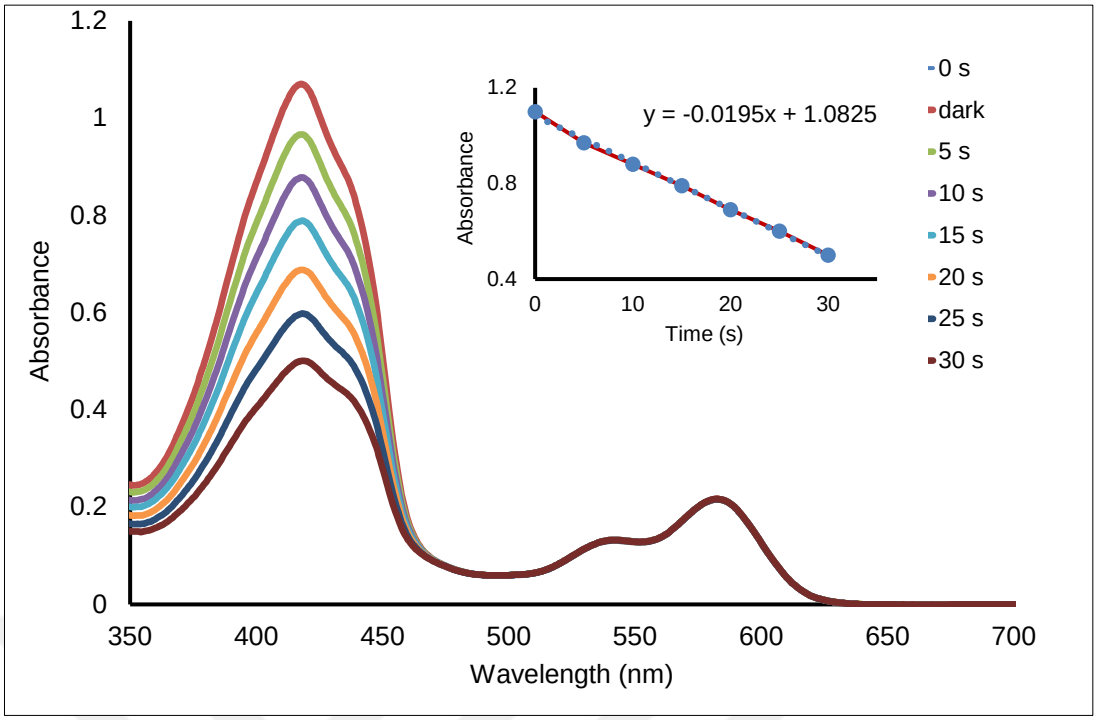

Figure 5.93: Decrease in absorbance spectrum of DPBF (35.0 µM) in the presence of 23 (2.0 µM) in DMSO.

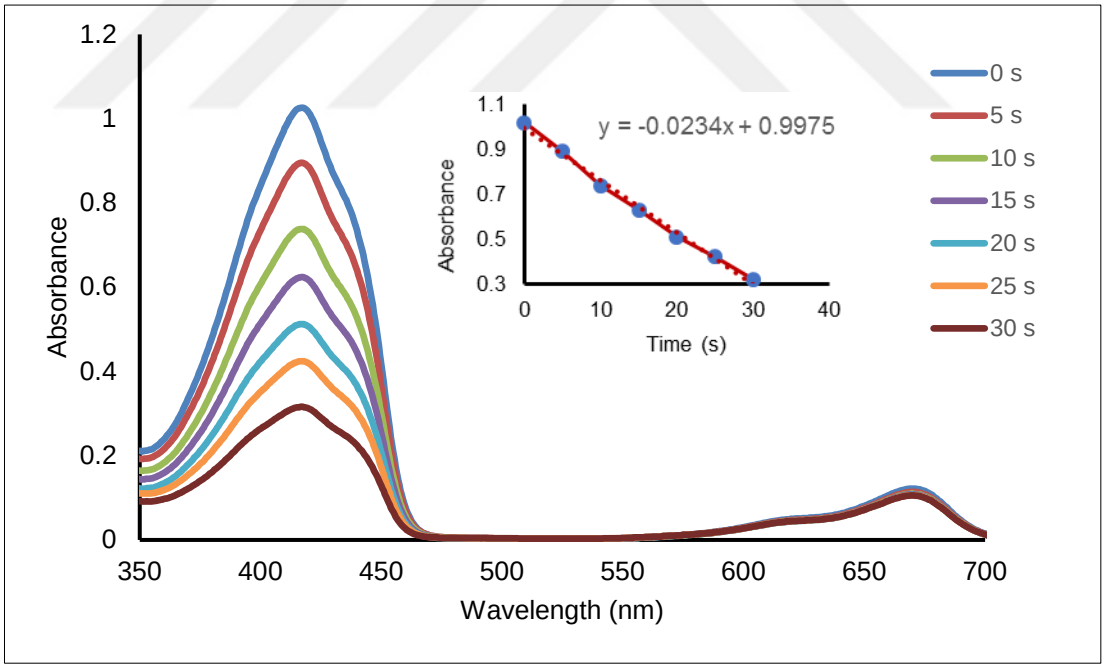

Figure 5.94: Decrease in absorbance spectrum of methylene blue in DMSO.

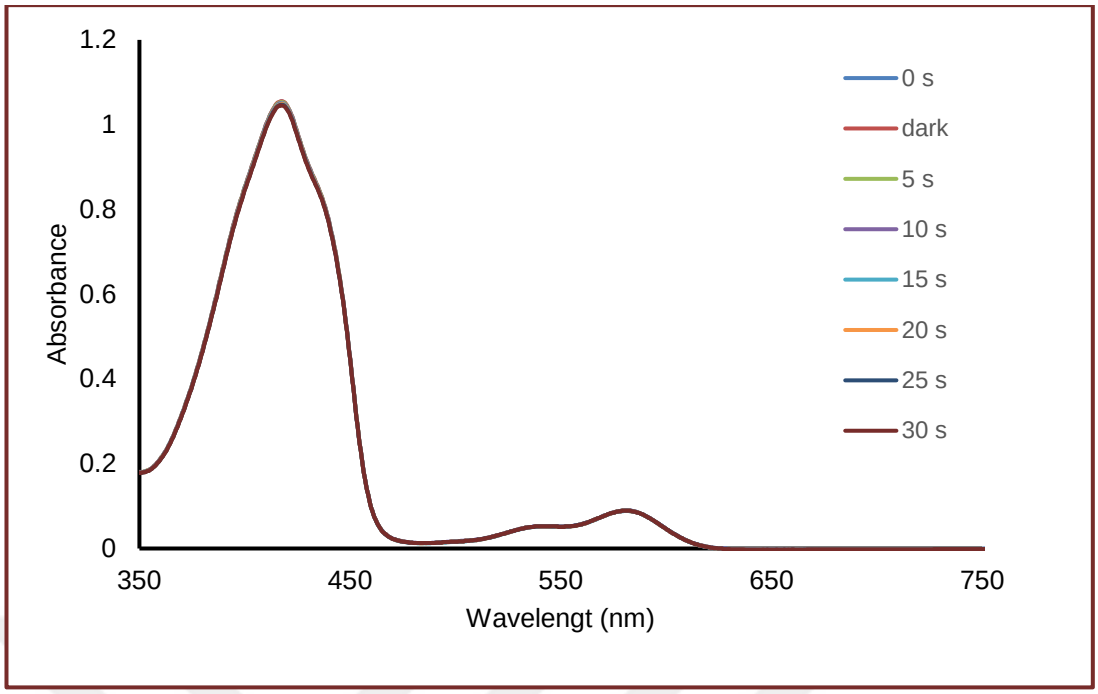

Figure 5.95: Decrease in absorbance spectrum of DPBF (35.0 µM) in the presence of 20 (2.0 µM) in DMSO.

5.3.1.2.*In vitro* photodynamic therapy

Beside the photophysical investigations of the compound, we studied the photodynamic therapy efficacy of **23** as well. In the PDT studies for treatment of cancer, *in vitro* and/or *in vivo* studies of ruthenium derivatives are widely used [59], [66]. In this part, for controlling the efficacy of **23** in PDT human chronic myeloid leukemia cell line, K562 was used. Increasing concentrations of **23** were used while incubating cells either under red light (λ= 632 nm, 2.5 mW /cm^2) or in dark for 5 h. Then, MTT assay was used to determine the cell viabilities. The results showed that complex **23** significantly reduces cell viabilities only under red light irradiation (Fig. 4.96). The singlet oxygen generation capability of **23** using red light was depicted in Figure 5.96. Apoptosis, well-regulated cell death mechanism, can be initiated by singlet oxygen [97]. In Figure 5.96, it is clear that, complex **23** cannot start cell death in dark. The success of light-excited **23** in the initiating cell death can be proved by the inhibitory concentration 50 (IC_{50}) value, which is below 5.0 µM.

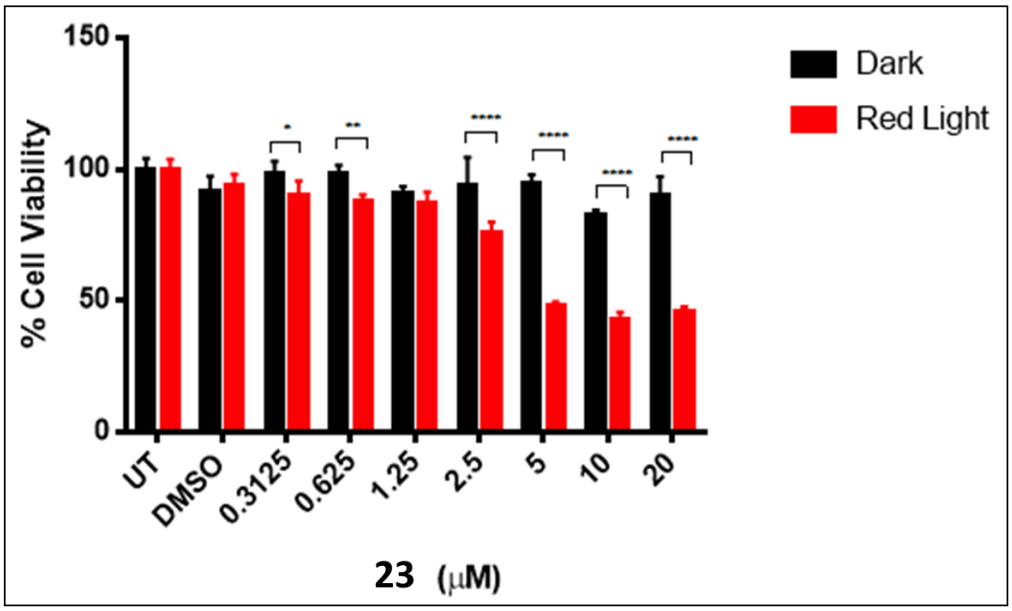

Figure 5.96: *In vitro* photodynamic therapy efficacy. *p<0.05; **p<0.01; ****p<0.0001.

In order to further study the capacity of **23** during cell death process under red light, Trypan Blue was used. It is a common dye that generally applied in cell culture and it cannot survive in living cells but it turns the nonviable cells into blue [98]. After the treatment of cells with Trypan Blue with or without **23** and using light or in dark, the blue colour was only observed in **23**-treated cells under red light. There exists several problems of the ruthenium complexes in PDT studies like high IC_{50} value [99] unwanted incubation time of dye [100] and treatment under lower wavelengths forbidding tissue penetration deeply [101]. Therefore, this study is significant for defeating these difficulties with having low cytotoxicity of **23** in dark relatively low IC_{50} value (<5 μM), short incubation time (5 h) and using light that facilitates the deep tissue penetration (Figure 5.97). However, additional *in vivo* studies are required to prove the efficiency of **23** in clinics.

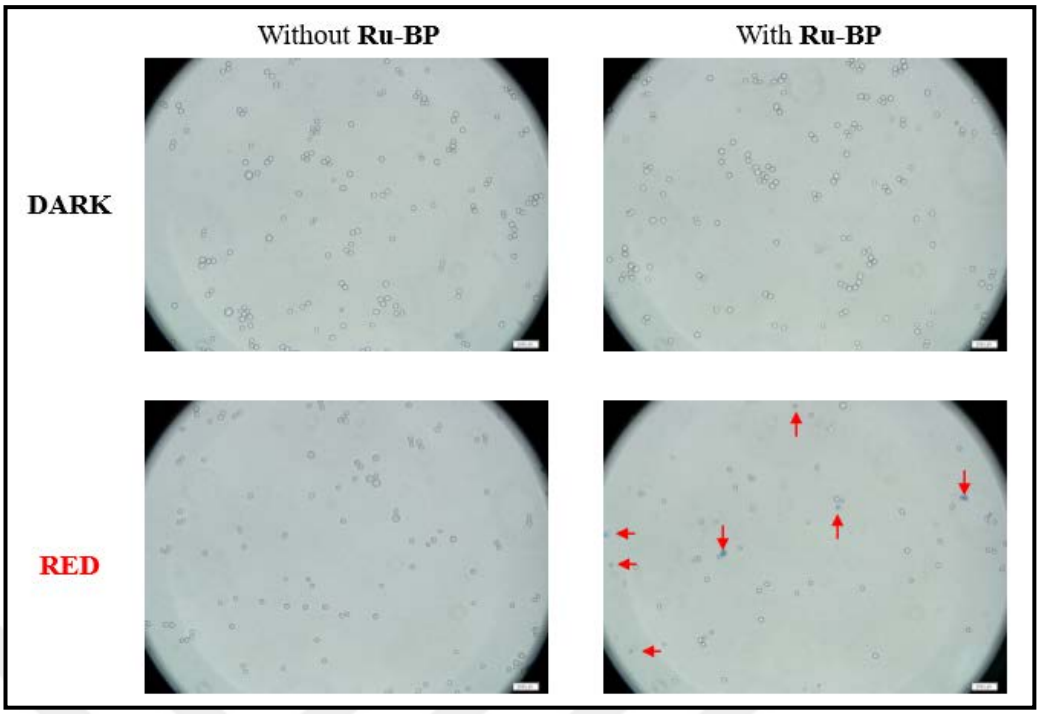

Figure 5.97: Trypan Blue staining of 23-treated or –untreated cells in dark or under red light. Red arrows point the blue-coloured cells. Scale: 200 µm.

5.3.2. Singlet Oxygen Generation Study of BODIPY ruthenium(II) (25) and iridium(III) complex (26)

5.3.2.1.Singlet oxygen measurements

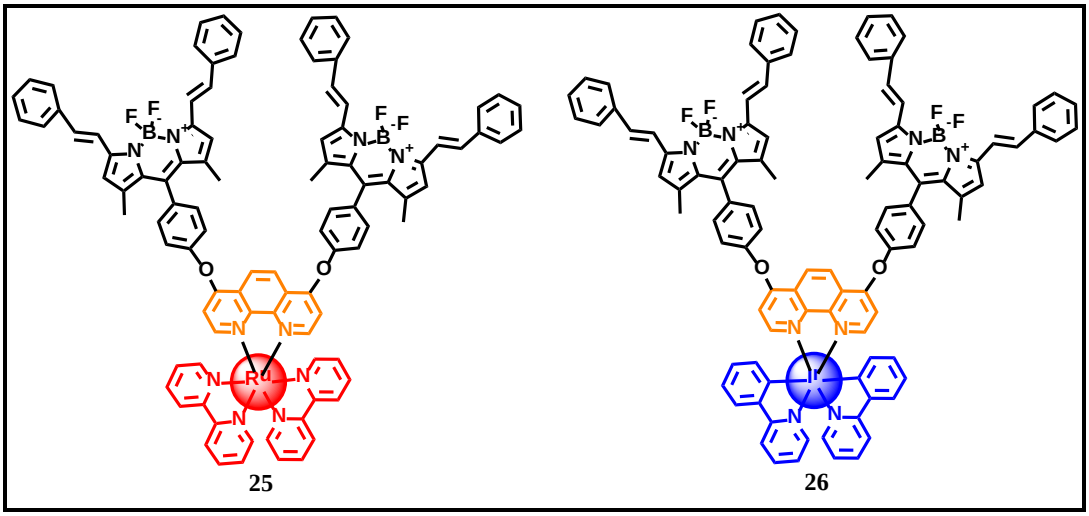

Figure 5.98: Molecular structures of 25 and 26.

As in the previous part, for measuring the relative singlet oxygen quantum yields of **25** and **26**, 1,3-diphenylisobenzofuran (DPBF) was used as the singlet oxygen trap

molecule and methylene blue as a reference sensitizer (φ_Δ=0.52 in DMSO. Firstly, each of the solutions including photosensitiser and DPBF was held for 30 min in the dark for removing possible input to the absorption of DPBF from dark reactions. For all candidates, the absorption value of trap molecule at 414 nm did not change. The solution containing DPBF (35.0 μM) and **25** (0.5 μM) was irradiated with red light (λ= 632 nm, 2.5 mW cm^{-2}) over 2.33 min. After treatment of **25** in DMSO, $^3O_2$ was sensitized to $^1O_2$, the characteristic absorption of DPBF at 414 nm decreased due to the decomposition by the singlet oxygen. Singlet oxygen production capacity of methylene blue (2.0 μM) and **26** (0.5 μM) were recorded with the same conditions. The change in absorption of DPBF versus irradiation time graph was plotted using the data of **25** and **26** (Figure 5.99).

Singlet oxygen quantum yields (φ_Δ) were found as 0.06 for **26** and 0.20 for **25**. $^1O_2$ generation ability of **26** is weaker (6%) which may be resulted from essential properties of the PS like the triplet excited state life and light absorbing capacity [102]. Ruthenium BODIPY complex **25** exhibited a well singlet oxygen generation performance. The noticeable φ_Δ may be resulted from heavy atom effect which also causes the rise of the intersystem crossing (ISC) and the spin−orbital coupling (SOC) rate that increase generation of $^1O_2$ [103].

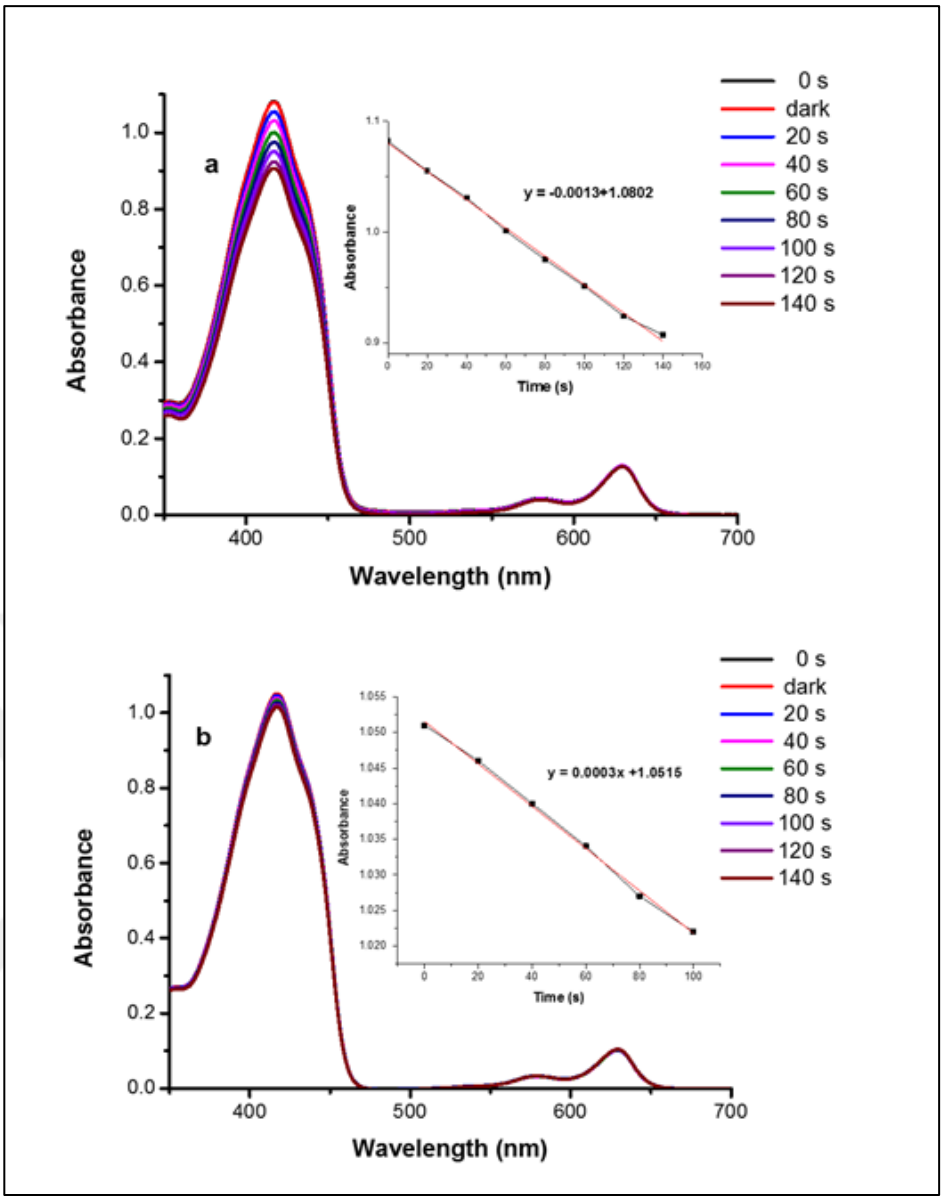

Figure 5.99: Decrease in absorbance of DPBF (35.0 μM) at 414 nm with time in DMSO in the presence of (a) 25 (0.5 μM) and (b) 26 (0.5 μM).

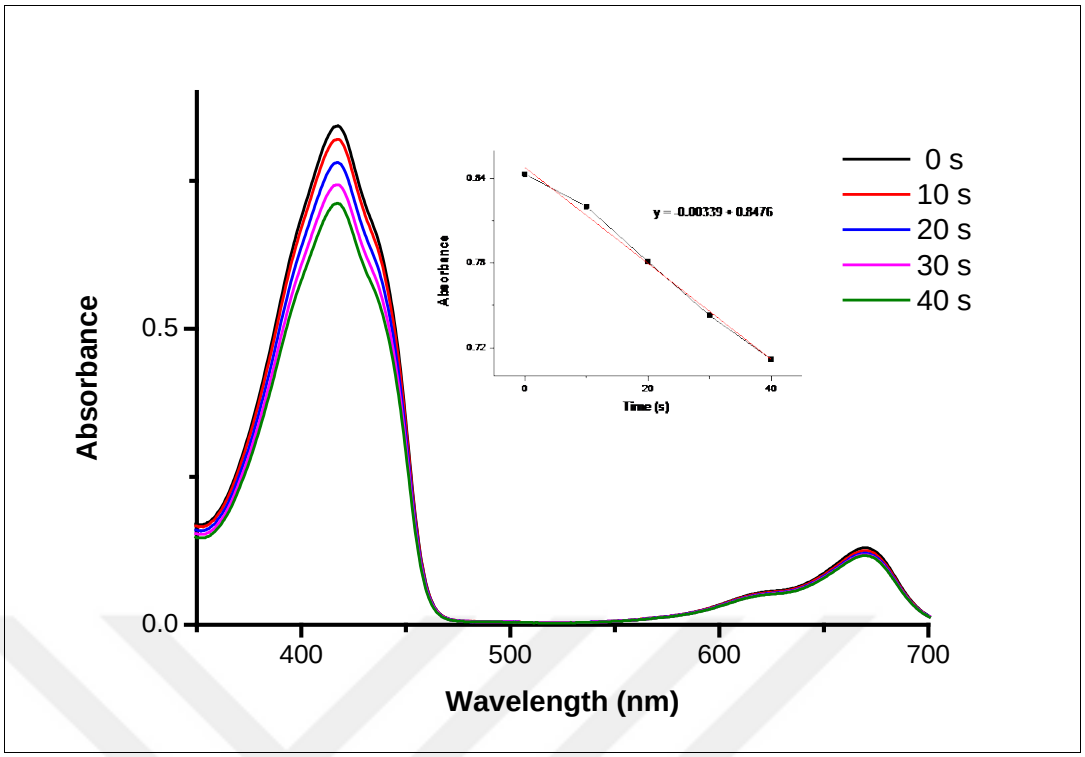

Figure 5.100: Decrease in absorbance of DPBF in the presence of methylene blue in DMSO.

5.3.2.2.*In vitro* photodynamic therapy

In vitro photodynamic therapy potentials of **25** (**Ru-BD**) and **26** (**Ir-BD**) were tried on human cancer cells. In this step, in order to test novel compounds on different tissue-like models human cervical cancer cell line, HeLa, and human chronic myeloid leukemia cell line, K562, were used. In the treatment of cells, increasing concentrations (1.5–25.0 μM) of **25** and **26** and DMSO were used. Over 5 hours, the cells were kept in the dark and under red light (λ= 632 nm, 2.5 mW /cm^2), then MTT assay was used to investigate cell viabilities. According to the findings, both **25** and **26** reduce cell viabilities under red light but not in the dark for both cells, HeLa (Figure 5.101) and K562 (Figure 5.102). The cell death potential of ruthenium complex **25** was much more than **26**. For both cell lines, the inhibitory concentration 50 (IC_{50}) of **25** was below 5.0 μM, although maximum amount of **26** was needed to initiate significant cell death. This consequence is proved by the singlet oxygen measurements (Figure 5.99).

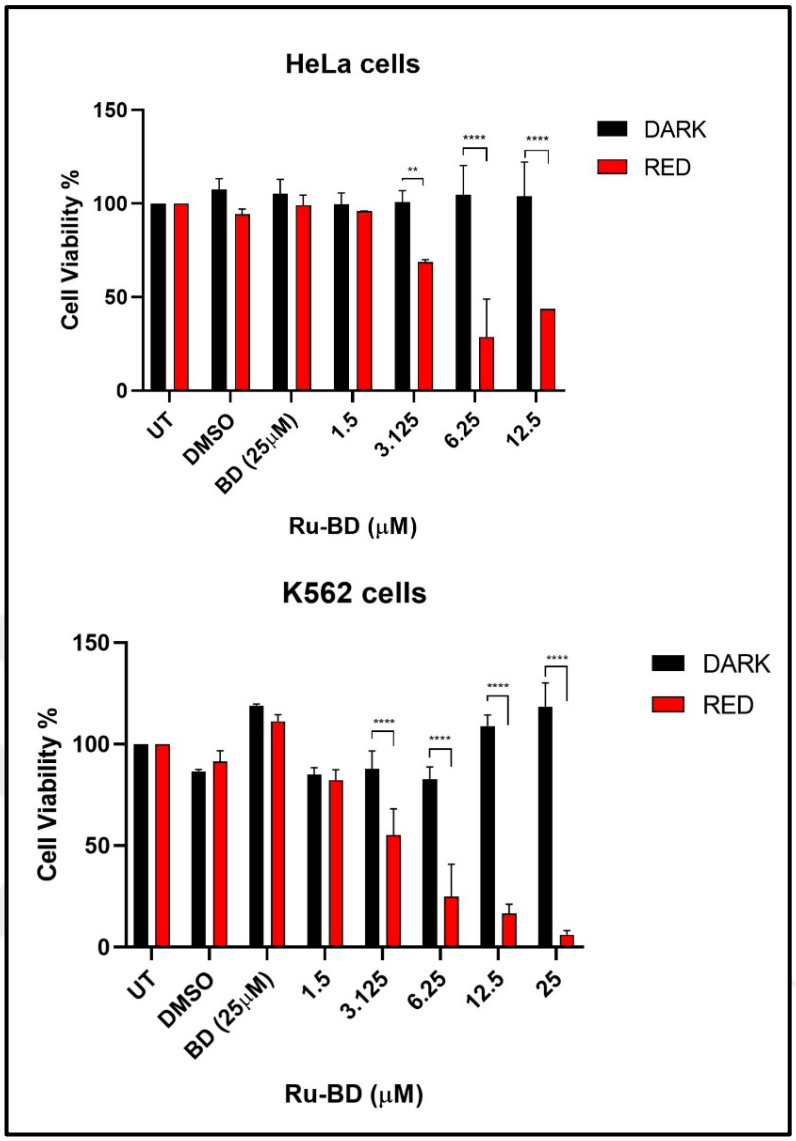

Figure 5.101: Effect of 25 on viabilities of HeLa and K562 cells in the dark and under the red light. **p<0.01; ****p<0.0001

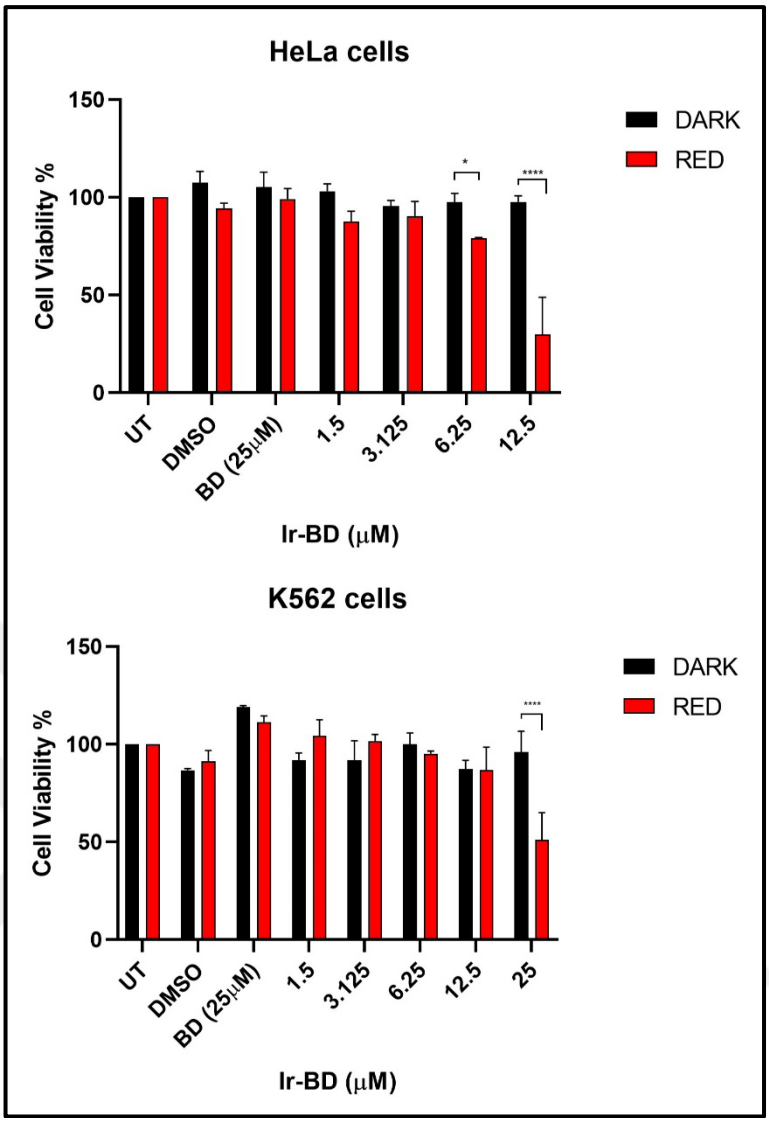

Figure 5.102: Effect of 26 on viabilities of HeLa and K562 cells in the dark and under the red light. *p<0.05; ****p<0.0001

In order to test the potential of the molecules, **25** (**Ru-BD**) and **26** (**Ir-BD**)**,** *in vitro*, Trypan Blue staining was used again. In this part, Trypan Blue was used to apply on HeLa cells after treatment with DMSO, **25** and **26** under red light and dark and a light microscope was used to take images. The blue color, an indicator of nonviable cells, was only seen in **25**- or **26**-treated cells with red light but not in dark according to the findings (Figure 5.103). As mentioned before, iridium and ruthenium complexes have some difficulties in PDT studies such as high IC_{50} value and long incubation time of photosensitizer [104], [105]. These novel complexes are unique examples that overcome these problems in PDT applications.

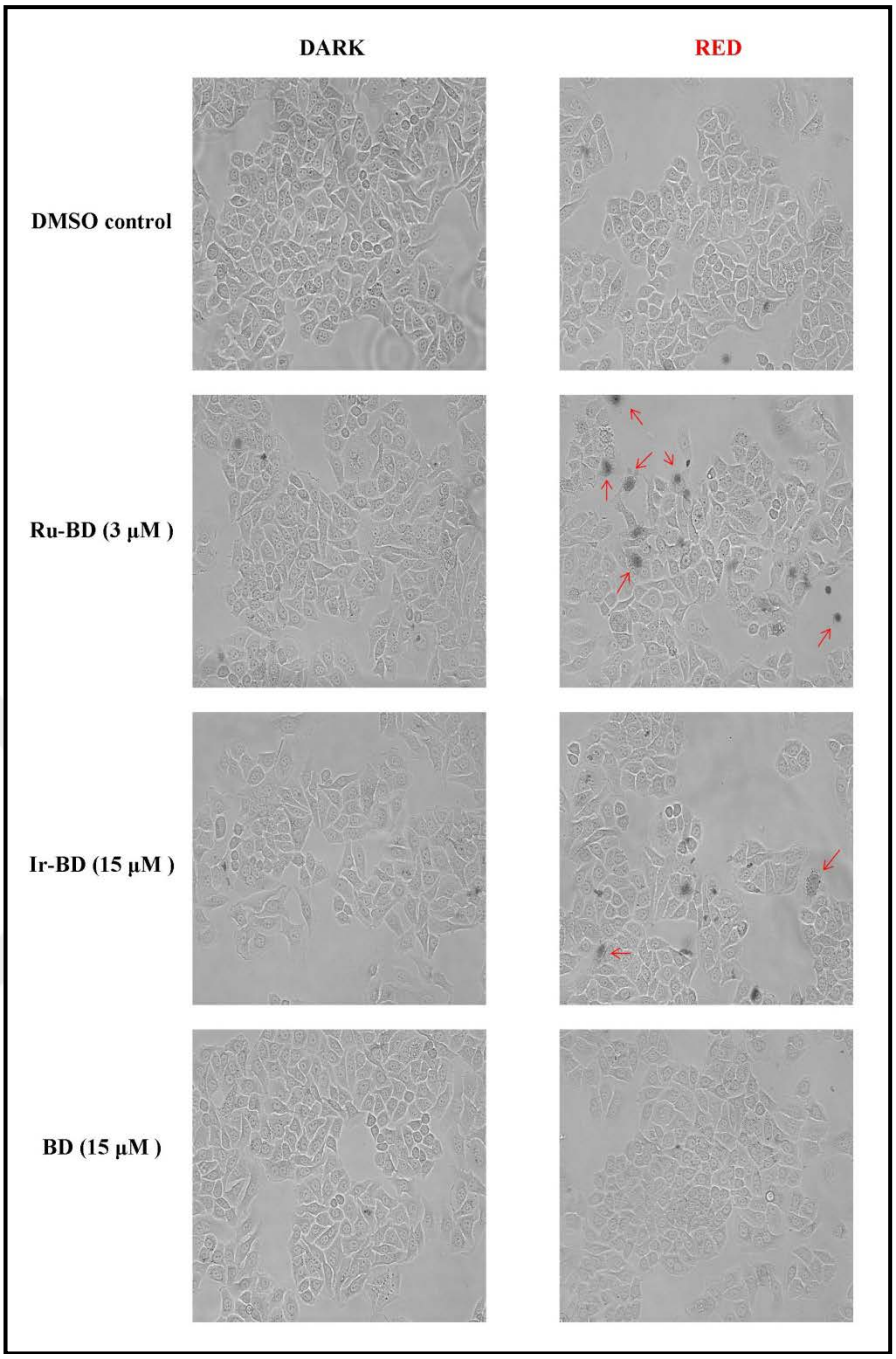

Figure 5.103: Trypan Blue staining of HeLa cells. Red arrows point the Trypan Blue-stained cells. Trypan Blue-stained cells are shown black in the figure.

Apoptosis, a common cell-regulated cell death mechanism, can be activated by intracellular or extracellular singlet oxygen. For further investigations, in order to quench the cell-free fluorescence and to get the signal from intracellular parts Trypan Blue used again [106]. Although the fluorescence intensity of the complexes were remarkable, the complexes was illustrated to penetrate into cells (Figure 5.104). To sum up, according to the *in vitro* PDT studies, the compounds are successful to

promote cell death in HeLa cells with red irradiation, and also these novel complexes are promising candidates for *in vitro* and/or *in vivo* PDT research.

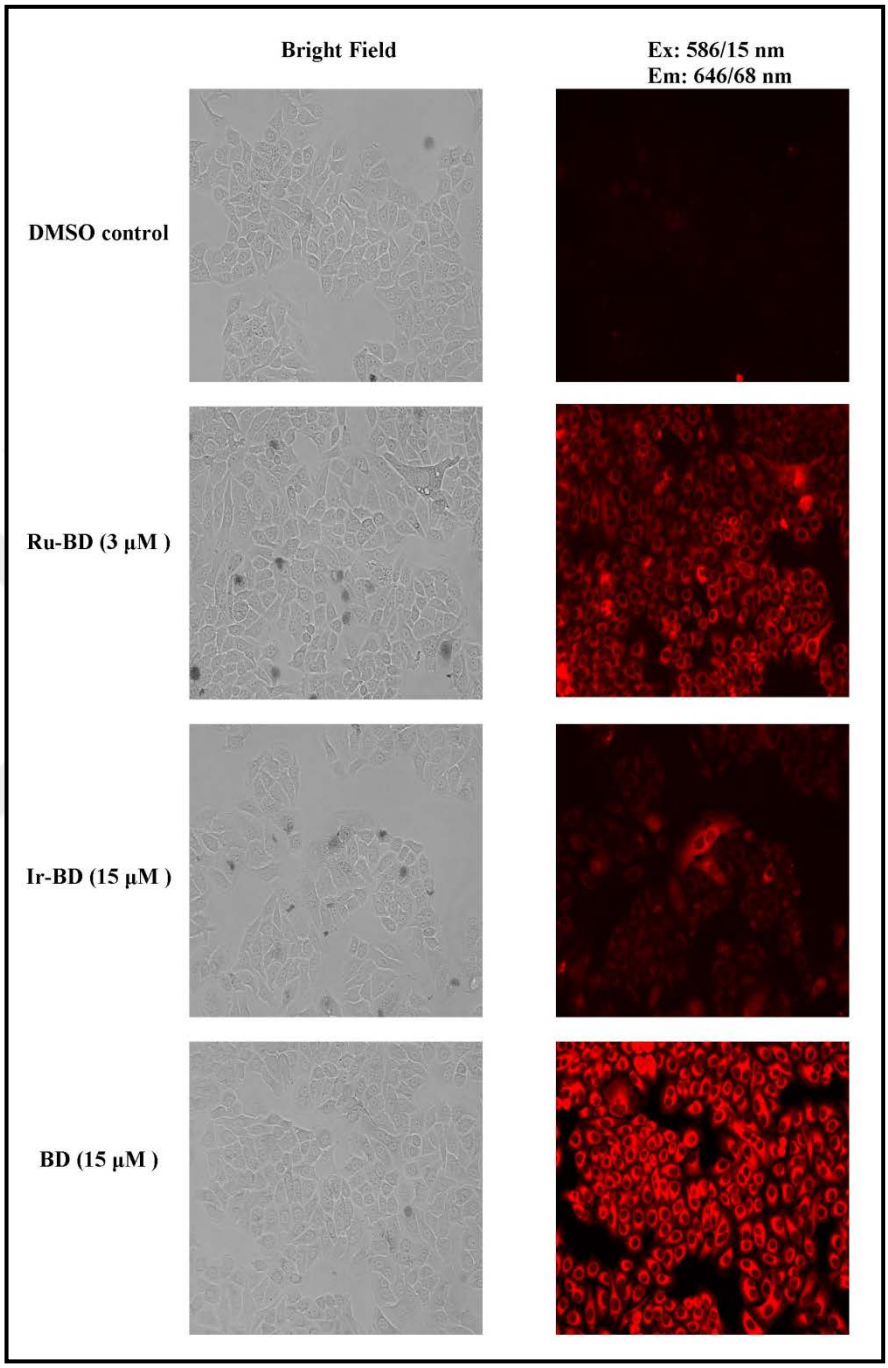

Figure 5.104: Internalization of complexes by HeLa cells.

6. CONCLUSION

In this thesis, the design and synthesis of novel perylene and BODIPY iridium(III) and ruthenium(II) metal complexes were achieved. Three of them were also investigated for photooxygenation purposes. The chemical characterizations of compounds were carried out by MALDI-TOF, FT-IR, ^{1}H and ^{13}C-NMR, UV-vis spectroscopy analyses.

In the first part of the work, we synthesized perylene bearing ruthenium and iridium metal complexes (**23** and **24**). The novel **23** and **24** compounds having two PDI core in a iridium(III) and ruthenium(II) complex which can be presented as a first phenanthroline ruthenium metal complex with bis(perylenediimide) substitution. The photochemical and photophysical properties of the compounds were recorded with fluorescence and absorption spectroscopies. The complexes exhibited favourable photophysical properties in the red region with good molar extinction coefficient. Among these compounds, the photosensitiser behaviour of ruthenium(II) perylene complex (**23**) was investigated. The final complex **23** showed notable photodynamic therapy potential *in vitro*. Additionally, the survival of human chronic myeloid cells, K562, was decreased by **23** significantly with red led but not in dark. This ruthenium photosensitiser (**23**) is also a considerable nominee to study *in vivo* PDT therapy owing to its low IC_{50} value, low toxicity in dark, possible longer tissue penetration and short incubation time.

In the second part of the thesis, the syntheses of novel BODIPY bearing ruthenium(II) (**25**) and iridium(III) (**26**) photosensitisers were exhibited and characterized chemically. The UV-vis absorptions of the molecules were measured in the red region of the spectrum. The capacity of singlet oxygen generation of the final complexes **25** and **26** were calculated by chemical method. To study *in vitro* PDT efficacy of the novel organic-metal complexes, chronic myeloid leukemia and cervical cancer cells were chosen. Both compounds (**25** and **26**) promoted the cell death upon red led irradiation. However, it is clear from the data that the addition of ruthenium to the main core drastically increases the photosensitizer behavior of the molecules, while iridium possesses lower potency as in the singlet oxygen measurements of the complexes. This part of the thesis also supports a new insight into the designing and developing photodynamic therapy candidates *in vivo* for related future works.

In the final step, the synthesis of new benzimidazole-fused perylene ruthenium (III) complex (**27**) was investigated. This molecule has an unique high π-conjugation which may be used in many applications.

REFERENCES

[1] Barbieri A., Bandini E., Monti F., Praveen V. K., Armaroli N., (2016), "The Rise of Near-Infrared Emitters: Organic Dyes, Porphyrinoids, and Transition Metal Complexes", Topics in Current Chemistry, 347, 47.

[2] Cai Y., Si W., Huang W., Chen P., Shao J., Dong X., (2018), "Organic Dye Based Nanoparticles for Cancer Phototheranostics", Small, 14, 1704247.

[3] Li C., Wonneberger H., (2012), "Perylene Imides for Organic Photovoltaics: Yesterday, Today, and Tomorrow", Advanced Materials, 24, 613–636.

[4] Huang C., Barlow S., Marder S. R., (2011), "Perylene-3,4,9,10-tetracarboxylic Acid Diimides: Synthesis, Physical Properties, and Use in Organic Electronics", Journal of Organic Chemistry, 76, 2386–2407.

[5] Ahrens M. J., Fuller M. J., Wasielewski M. R., (2003), "Cyanated Perylene-3,4-dicarboximides and Perylene-3,4:9,10-bis(dicarboximide): Facile Chromophoric Oxidants for Organic Photonics and Electronics", Chemistry of Materials, 15, 2684–2686.

[6] Zhan X., Tan Z. A., Domercq B., An Z., Zhang X., Barlow S., Li Y., Zhu D., Kippelen B., Marder S. R., (2007), "A High-Mobility Electron-Transport Polymer with Broad Absorption and Its Use in Field-Effect Transistors and All-Polymer Solar Cells", Journal of American Chemical Society, 129, 7246–7247.

[7] Law K. Y., (1993), "Organic photoconductive materials: recent trends and developments", Chemical Reviews, 93, 449–486.

[8] Sadrai M., Bird G. R., (1984), "A new laser dye with potential for high stability and a broad band of lasing action: Perylene-3,4,9,10-tetracarboxylic acid-bis-N,N′(2′,6′ xylidyl)diimide", Optics Communications, 51, 62–64.

[9] Ford W. E., Kamat P. V., (1987), "Photochemistry of 3,4,9,10-perylenetetracarboxylic dianhydride dyes. 3. Singlet and triplet excited-state properties of the bis(2,5-di-tert-butylphenyl)imide derivative", Journal of Physical Chemistry, 91, 6373–6380.

[10] Schmidt-Mende L., Fechtenkötter A., Müllen K., Moons E., Friend R. H., MacKenzie J. D., (2001), "Self-organized discotic liquid crystals for high-efficiency organic photovoltaics", Science, 293, 1119–1122.

[11] Wang H., Peng B., Wei W., (2008), "Solar cells based on perylene bisimide derivatives", Progress in Chemistry, 20, 1751–1760.

[12] Abdel-Shafi A. A., Worrall D. R., Ershov A. Y., (2004), "Photosensitized generation of singlet oxygen from ruthenium(ii) and osmium(ii) bipyridyl complexes", Dalton Transactions, 103, 30–36.

[13] Santos E. R. D., Pina J., Venâncio, Serpa C., Martinho J. M. G., Carlos R. M., (2016), "Photoinduced energy and electron-Transfer reactions by polypyridine ruthenium(II) complexes containing a derivatized perylene diimide", Journal of Physical Chemistry C, 120, 22831–22843.

[14] Brancini G. T. P., Rodrigues G. B., Rambaldi M. S. L., Izumi C., Yatsuda A. P., Wainwright M., Rosa J. C., Braga G. U. L., (2016), "The effects of photodynamic treatment with new methylene blue N on the Candida albicans proteome", Photochemical and Photobiological Sciences, 15, 1503–1513.

[15] Würtner F, Stepanenko V, Chen Z, Saha-Möller C. R., Kocher N, Stalke D., (2004), "Preparation and characterization of regioisomerically pure 1,7-disubstituted perylene bisimide dyes", Journal of Organic Chemistry, 69, 7933-9.

[16] Kozma E., Catellani M., (2013), "Perylene diismides based materials for organic solar cells", Dyes and Pigments, 98, 160-179.

[17] Yukinori N., Takahisa, M., (1981), "Synthesis and Reactions of Perylenecarboxylic Acid Derivatives. VIII. Synthesis of N-Alkyl-3,4:9,10-Perylenetetracarboxylic Monoanhydride Monoimide", Bulletin of the Chemical Society of Japan, 54 (4), 1191-1194.

[18] Dubey R. K., Westerveld N., Sudhölter E. J. R., Grozemab F. C., Jager, W. F., (2016), "Novel derivatives of 1,6,7,12-tetrachloroperylene-3,4,9,10-tetracarboxylic acid: synthesis, electrochemical and optical properties", Organic Chemistry Frontiers, 3, 1481.

[19] Wu J., He D., Zhang L., Liu Y., Mo X., Lin J., Zhang H. J., (2017), "Direct Synthesis of Large-Scale Ortho-Iodinated Perylene Diimides: Key Precursors for Functional Dyes", Organic Letters, 19, 5438−5441.

[20] Dincalp H., Kızılok S., İcli S., (2014), "Targeted Singlet Oxygen Generation Using Different DNA-Interacting Perylene Diimide Type Photosensitizers", Journal of Fluorescence, 24, 917–924.

[21] Luo Z., Wu F., Zhang T., Zeng., Xiao Y., Liu T., Zhong C., Lu X., Zhu L., Yang S., Yang C., (2019), "Designing a Perylene Diimide/Fullerene Hybrid as Effective ElectronTransporting Material in Inverted Perovskite Solar Cells withEnhanced Efficiency and Stability", Angewandte Chemie International Edition, 58, 1–7.

[22] Treibs A., Kreuzer F. H., Liebigs J., (1968), "meso-Substituierte Dipyrrolylmethane und-methene", Annalen der Chemie., 718, 208.

[23] Beer G., Rurack K., Daub J., (2001), "Chiral discrimination with a fluorescent boron–dipyrromethene dye", Chemical Communications, 1138-1139.

[24] Haugland R. P., (2002), “Handbook of Fluorescent Probes and Research Products”, 9th Edition, Molecular Probes Inc.

[25] McCusker C., Carroll B., Rotello V. M., (2005), “Cationic polyhedral oligomeric silsesquioxane (POSS) units as carriers for drug delivery processes”, Chemical Communications, 996-998.

[26] Lammi R. K., Amboise A., Balasubramanian T., Wagner R. W., Bocian D. F., Holten D., Lindsey S., (2000), “Structural Control of Photoinduced Energy Transfer between Adjacent and Distant Sites in Multiporphyrin Arrays”, Journal of American Chemical Society, 122, 7579-7591.

[27] Chen T., Boyer J. H., Trudell M. L., (1997), “Synthesis of 2,6-diethyl-3-methacroyloxymethyl-1,5,7,8-tetramethylpyrromethene-BF2 for the preparation of new solid-state laser dyes”, Heteroatom Chemistry, 8, 51-54.

[28] Hattori S., Ohkubo K., Urano Y., Sunahara H., Nagano T., Wada Y., Tkchanko N. V., Lemmetyinen H., Fukuzumi S., (2005), “Charge Separation in a Nonfluorescent Donor−Acceptor Dyad Derived from Boron Dipyrromethene Dye, Leading to Photocurrent Generation”, Journal of Physical Chemistry B, 109, 15368-15375.

[29] Ulrich G., Ziessel R., Harriman A., (2008), “The chemistry of fluorescent bodipy dyes: versatility unsurpassed”, Angewandte Chemie International Edition, 47, 1184-1201.

[30] Dost Z., Atilgan S., Akkaya E. U., (2006), “Distyryl-boradiazaindacenes: facile synthesis of novel near IR emitting fluorophores”, Tetrahedron, 62, 8484-8488.

[31] Loudet A., Burgess K., (2007), “BODIPY dyes and their derivatives: syntheses and spectroscopic properties”, Chemical Reviews, 107, 4891-4932.

[32] Kamkaew A., Lim S. H., Lee H. B., Kiew L. V., Chung L. Y., Burgess K., (2013), “BODIPY dyes in photodynamic therapy”, Chemical Society Reviews, 42, 77-88.

[33] Yogo T., Urano Y., Ishitsuka Y., Maniwa F., Nagano T., (2005), “Highly efficient and photostable photosensitizer based on BODIPY chromophore”, Journal of American Chemical Society, 127, 12162-12163.

[34] [Frimannsson D. O., Grossi M., Murtagh J., Paradisi F., O'Shea D. F., (2010), “Light induced antimicrobial properties of a brominated boron difluoride (BF2) chelated tetraarylazadipyrromethene photosensitizer”, Journal of Medicinal Chemistry, 53, 7337-7343.

[35] Jina Y., Lva M., Taoa Y., Xub S., Hea J., Zhanga J., Zhao W., (2019), “A water-soluble BODIPY-basedfluorescent probe for rapid and selectivedetection of hypochlorous acid in living cells”, Spectrochimica Acta Part A: Molecular and Biomolecular Spectroscopy, 219, 569–575.

[36] Lia Z., Liub Y., Houa X., Xua Z., Liua C., Zhanga F., Xie Z., (2019), "The crystal structures, spectrometric, photodynamic properties andbioimaging ofβ-βlinked Bodipy oligomers", Journal of Luminescence, 212, 306–314.

[37] Guptaa G., Cherukommub S., Srinivasb G., Leea S. W., Munc S. H., Jungc J., Nageshb N., Lee, C. Y. (2018), "BODIPY-based Ru(II) and Ir(III) organometallic complexes of avobenzone, a sunscreen material: Potent anticancer agents", Journal of Inorganic Biochemistry, 189, 17–29.

[38] Eçik E. T., Kazan H. H., Sengul İ. F., Kandemir H., Coşut B., (2019), "Meso-piperidine linked bodipys: Synthesis, fluorescent properties and biological evaluation", Journal of Luminescence, 205, 258–264.

[39] Hartinger C. G., Dyson P. J., (2009), "Bioorganometallic chemistry-from teaching paradigms to medicinal applications", Chemical Society Reviews, 38, 391–401.

[40] Huang T., Yu Q., Liu S., Huang W., Zhao Q., (2018), "Phosphorescent iridium(III) complexes: a versatile tool for biosensing and photodynamic therapy", Dalton Transactions, 47, 7628.

[41] Hu T., He L., Duan L., Qiu Y., (2012), "Solid-state light-emitting electrochemical cells based on ionic iridium(III) complexes", Journal of Materials Chemistry, 22, 4206.

[42] Schneider G. E., (2013), "Ionic Transition Metal Complexes Containing Iridium(III) for Lighting Applications", Doctoral Thesis, University of Basel.

[43] McKenzie L. K., Bryant H. E., Weinstein J. A., (2019), "Transition metal complexes as photosensitisers in one- and two-photon photodynamic therapy", Coordination Chemistry Reviews, 379, 2–29.

[44] Akbayeva D., Gonsalvi L., Oberhauser W., Peruzzini M., Vizza F., Brugeller P., Romerosa A., Sava G., Bergamo A., (2003), "Synthesis, catalytic properties and biological activity of new water soluble ruthenium cyclopentadienyl PTA complexes [(C5R5)RuCl(PTA)2] (R = H, Me; PTA = 1,3,5-triaza-7-phosphaadamantane)", Chemical Communications, 264-265.

[45] Yang Y., Liao G., Fu C., (2018), "Recent Advances on Octahedral Polypyridyl Ruthenium(II) Complexes as Antimicrobial Agents", Polymers, 10, 650.

[46] Motswainyana W. M., Ajibade, P. A., (2015), "Anticancer Activities of Mononuclear Ruthenium(II) Coordination Complexes Advances in Chemistry", 859730.

[47] Liu J., Zhang C., Rees T. W., Ke L., Ji L., Chao H., (2018), "Harnessing ruthenium(II) as photodynamic agents: Encouraging advances in cancer therapy", Coordination Chemistry Reviews, 363, 17–28.

[48] Schulze M., Steffen A., Würthner F., (2015), “Near-IR Phosphorescent Ruthenium(II) and Iridium(III) Perylene Bisimide Metal Complexes”, Angewandte Chemie International Edition, 54, 1570 –1573.

[49] Wang J., Lu Y., McGoldrick N., Zhang C., Yang W., Zhaob J., Draper S. M., (2016), “Dual phosphorescent dinuclear transition metal complexes, and their application as triplet photosensitizers for TTA upconversion and photodynamic therapy”, Journal of Materials Chemistry C, 4, 6131.

[50] Wang J., Lu Y., McCarthy W., Conway-Kenny R., Twamley B., Zhao J., Draper S. M., (2018), “Novel ruthenium and iridium complexes of N-substituted carbazole as triplet photosensitisers”, Chemical Communications, 54, 1073.

[51] Stringera T., Alejandra M., Quinteroa S., Wiesnerb L., Smithc G. S., Nordlander E., (2019), “Evaluation of PTA-derived ruthenium(II) and iridium(III) quinoline complexes against chloroquine-sensitive and resistant strains of the Plasmodium falciparum malaria parasite”, Journal of Inorganic Biochemistry, 191, 164–173.

[52] Pierroz V., Joshi T., Leonidova A., Mari C., Schur J., Ott I., Spiccia L., Ferrari S., Gasser G., (2012), “Molecular and Cellular Characterization of the Biological Effects of Ruthenium(II) Complexes Incorporating 2 Pyridyl-2-pyrimidine-4- carboxylic Acid”, Journal of American Chemical Society, 134, 20376−20387.

[53] McKenzie L. K., Sazanovich I. V., Baggaley E., Bonneau M., Guerchais V., Williams J. A. G., Weinstein J. A., Bryant H. E., (2017), “Metal Complexes for Two-Photon Photodynamic Therapy: A Cyclometallated Iridium Complex Induces Two-Photon Photosensitization of Cancer Cells under Near-IR Light”, Chemistry: A European Journal, 23, 234–238.

[54] Hopper C., (2000), “Photodynamic therapy: a clinical reality in the treatment of cancer”, The Lancet Oncology, 1, 212.

[55] Konan Y. N., Gurny R., Alle´mann E., (2002), “State of the art in the delivery of photosensitizers for photodynamic therapy”, Journal of Photochemistry and Photobiology B: Biology, 66, 89.

[56] Puolakkainen P., (1992), “Photodynamic Therapy of Gastrointestinal Tumors: A Review Second Department of Surgery”, Digestive Diseases, 10, 53-60.

[57] Palumbo G., (2007), “Photodynamic therapy and cancer: a brief sightseeing tour”, Expert Opinion on Drug Delivery, 4, 131-148.

[58] Zhao J., Wu W., Sun J., Guo S., (2013), “Triplet photosensitizers: from molecular design to applications”, Chemical Society Reviews, 42, 5323-5351.

[59] Kaspler P., Lazic S., Forward S., Arenas Y., Mandela A., Lilge L., (2016), “A ruthenium(II) based photosensitizer and transferrin complexes enhance photo-

physical properties, cell uptake, and photodynamic therapy safety and efficacy", Photochemical and Photobiological Sciences, 15, 481–495.

[60] Sava G., Zorzet S., Perissin L., Mestroni G., Zassinovich G., Bontempi A., (1987), "Coordination metal complexes of Rh(I), Ir(I) and Ru(II): recent advances on antimetastatic activity on solid mouse tumors", Inorganica Chimica Acta, 137, 69−71.

[61] Kue C. S., Ng S. Y., Voon S. H., Kamkaew A., Chung L. Y., Kiewe L. V., Lee H. B., (2018), "Recent strategies to improve boron dipyrromethene (BODIPY) for photodynamic cancer therapy: an updated review", Photochemical and Photobiological Sciences, 17, 1691–1708.

[62] Santos E. R., Pina J., Venâncio T., Serpa C., Martinho J. M. G., Carlos R. M., (2016), "Photoinduced Energy and Electron-Transfer Reactions by Polypyridine Ruthenium(II) Complexes Containing a Derivatized Perylene Diimide", Journal of Physical Chemistry C, 120, 22831−22843.

[63] Ulrich G., Ziessel R., Harriman A., (2008), "The chemistry of fluorescent bodipy dyes: versatility unsurpassed", Angewandte Chemie International Edition, 47, 1184–1201.

[64] Lukyanets E. A., (1998), "NIR Photosensitisers in photodynamic therapy", Near-Infrared Dyes for High Technology Applications, 307-324.

[65] Dubey R. K., Niemi M., Kaunisto K., Stranius K., Efimov A., Tkachenko N. V., Lemmetyinen H., (2013), "Excited-State Interaction of Red and Green Perylene Diimides with Luminescent Ru(II) Polypyridine Complex", Inorganic Chemistry, 52, 9761−9773.

[66] Maia P. J. S., Aguiar I., Velloso M. S., Zhang D., Santos E. R., Oliveira J. R., Junqueira J. C., Selke M., Carlos R. M., (2018), "Singlet oxygen production by a polypyridine ruthenium (II) complex with a perylene monoimide derivative: A strategy for photodynamic inactivation of Candida albicans", Journal of Photochemistry and Photobiology A, 353, 536–545.

[67] Kodama K., Kobayashi A., Hirose T., (2013), "Synthesis and spectral properties of ruthenium(II) complexes based on 2,2′-bipyridines modified by a perylene chromophore", Tetrahedron Letters, 54, 5514–5517.

[68] Lu X. H., Shi S., Yao J. L., Gao X., Huang H. L., Yao T. M., (2014), "Two structurally analogous ruthenium complexes as naked-eye and reversible molecular "light switch" for G-quadruplex DNA", Journal of Inorganic Biochemistry, 140, 64–71.

[69] Graf G. I., Hastreiter D., Silva L. E., Rebelo R. A., (2002), " The synthesis of aromatic diazatricycles from phenylenediamine-bis(methylene Meldrum's acid) derivatives", Tetrahedron, 58, 9095–9100.

[70] Molock F., Boykin D. W., (1983), “The synthesis of pyridoquinolines with dialkylaminopropylamine side chains”, Journal of Heterocyclic Chemistry, 20, 681-686.

[71] Nakabayashi Y., Watanabe T., Nakao T., Yamauchi O., (2004), “Interactions of mixed ligand ruthenium(II) complexes containing an amino acid and 1,10-phenanthroline with DNA”, Inorganica Chimica Acta, 357, 2553.

[72] Lowry M. S., Hudson W. R., Pascal R. A., Bernhard S., (2004), “Accelerated Luminophore Discovery through Combinatorial Synthesis”, Journal of American Chemical Society, 126, 14129-135.

[73] Chen W. Q. S., Sun X., Liu Y., Zhu D., (2006), “Suzuki coupling reaction of 1,6,7,12-tetRabromoperylene bisimide”, Organic Letters, 8, 867-870.

[74] Hill Z. B., Rodovsky D. B., Legera J. M., Bartholomew G. P, (2008), “Synthesis and utilization of perylene-based n-type small molecules in light-emitting electrochemical cells”, Chemical Communications, 6594-96.

[75] Quante H., Schlichting P., Rohr U., Geerts, Y., Müllen K., (1996), “Novel Perylene-containing Polymers", Macromolecular chemistry and physics, 197, 4029-44.

[76] Wescott L. D., Mattern D. L., (2003), “Donoredeacceptor molecules incorporating a nonadecyl-swallowtailed perylenediimide acceptor”, Journal of Organic Chemistry, 68, 10058-66.

[77] Guo H., Jing Y., Yuan X., Ji S., Zhao J., Lib X., Kanc Y., (2011), “Highly selective fluorescent OFF–ON thiol probes based on dyads of BODIPY and potent intramolecular electron sink 2,4-dinitrobenzenesulfonyl subunits”, Organic&Biomolecular Chemistry, 9, 3844.

[78] Adarsh N., Shanmugasundaram M., Avirah R. R., Ramaiah D., (2012), “Aza-BODIPY Derivatives: Enhanced Quantum Yields of Triplet Excited States and the Generation of Singlet Oxygen and Their Role as Facile Sustainable Photooxygenation Catalysts”, Chemistry European Journal, 18, 12655-62.

[79] Adarsh N., Avirah R. R., Ramaiah D., (2010), “Tuning photosensitized singlet oxygen generation efficiency of novel aza-BODIPY dyes”, Organic Letters, 12, 5720-5723.

[80] Bruker, SADABS, Bruker AXS Inc., Madison, Wisconsin, USA, 2005.

[81] Bruker APEX2 (Version 2011.4-1) Bruker AXS Inc., Madison, Wisconsin, USA, 2008.

[82] Sheldrick G. M., SHELXS97, Programs for crystal structure solution.

[83] Spek A. L., (2003), “Single-crystal structure validation with the program PLATON”, Journal of Applied Crystallography, 36, 7-13.

[84] Macrae C. F., Edgington P. R., McCabe P., Pidcock E., Shields G. P., Taylor R., Towler M., Streek J., (2006), "Mercury: visualization and analysis of crystal structures", Journal of Applied Crystallography, 39, 453-457.

[85] Brandenburg K., (2006), DIAMOND 3.1 for Windows. Crystal Impact GbR, Bonn, Germany.

[86] Aksakal N. E., Chumakov Y., Yuksel F., (2019), "Crystal Structures of Two Perylenediimides: A Study of Bay-Substitution", Journal of Chemical Crystallography, 49, 72-79.

[87] Aksakal N. E., Ecik E. T., Kazan H. H., Ciftci G. Y., Yuksel F., (2019), "Novel ruthenium(II) and iridium(III) BODIPY dyes:insights into their application in photodynamic therapy in vitro", Photochemical and Photobiological Sciences, 18, 2012-2022.

[88] Aksakal N. E., Kazan H. H., Ecik E. T., Yuksel F., (2018), "A novel photosensitizer based on a ruthenium(II) phenanthroline bis(perylenediimide) dyad: synthesis, generation of singlet oxygen and in vitro photodynamic therapy", New Journal of Chemistry, 2018, 42, 17538-17545.

[89] Bonnett R., (2000), "Chemical Aspects of Photodynamic therapy", Gordon & Breach.

[90] Ethirajan M., Chen Y., Joshi P., Pandey R. K., (2011), "The role of porphyrin chemistry in tumor imaging and photodynamic therapy", Chemical Society Reviews, 40, 340–362.

[91] Ulrich G., Ziessel R., Harriman A., (2008), "Die vielseitige Chemie von Bodipy-Fluoreszenzfarbstoffen", Angewandte Chemie, 120, 1202–1219.

[92] Wang T., Hou Y., Chen Y., Li K., Cheng X., Zhou Q., Wang X., (2015), "Two novel BODIPY–Ru(II) arene dyads enabling effective photo-inactivation against cancer cells", Dalton Transactions, 44, 12726.

[93] Kue C. S., Ng S. Y., Voon S. H., Kamkaew A., Chung L. Y., Kiewe L. V.,c Lee H. B., (2018), "Recent strategies to improve boron dipyrromethene (BODIPY) for photodynamic cancer therapy: an updated review", Photochemical and Photobiological Sciences, 17, 1691.

[94] Lovell J. F., Liu T. W. B., Chen J., Zheng G., (2010), "Activatable Photosensitizers for Imaging and Therapy", Chemical Reviews, 110, 2839-57.

[95] Würthner F., (2004), "Perylene bisimide dyes as versatile building blocks for functional supramolecular architectures", Chemical Communications, 1564–1579.

[96] Zhao J., Wu W., Sun J., Guo S., (2013), "Triplet photosensitizers: from molecular design to applications", Chemical Society Reviews, 42, 5323-5351.

[97] Zheng L., Kuang S., Li G., Jin C., Ji L., Chao H., (2017), “A GSH-activatable ruthenium(II)-azo photosensitizer for two-photon photodynamic therapy”, Chemical Communications, 53, 1977-1980.

[98] Reithmuller M., Burger N., Bauer G., (2015), “Singlet oxygen treatment of tumor cells triggers extracellular singlet oxygen generation, catalase inactivation and reactivation of intercellular apoptosis-inducing signaling”, Redox Biology, 6, 157-168.

[99] Barekzi N., Laroussi M., Konesky G., Roman S., (2016), “ Effects of Low Temperature Plasmas on Cancer Cells”, Plasma Processes and Polymers, 13, 1189-1194.

[100] Qiu K., Wang J., Song C., Wang L., Zhu H., Huang H., Huang J., Wang H., Ji L., Chao L., (2017), “Crossfire for Two-Photon Photodynamic Therapy with Fluorinated Ruthenium (II) Photosensitizers”, ACS Applied Materials&Interfaces, 9, 18482-18492.

[101] Huang H., Zhang P., Yu B., Jin C., Ji L., Chao H., (2015), “Synthesis, characterization and biological evaluation of mixed-ligand ruthenium(II) complexes for photodynamic therapy”, Dalton Transactions, 44, 17335-17345.

[102] Majumdar P., Yuan X., Li S., Guennic B. L., Ma J., Zhang C., Jacqueminde D., Zhao J., (2014), “Cyclometalated Ir(III) complexes with styryl-BODIPY ligands showing near IR absorption/emission: preparation, study of photophysical properties and application as photodynamic/luminescence imaging materials”, Journal of Materials Chemistry B, 2014, 2, 2838–2854.

[103] Higgins S. H. L., Brewer K. J., (2012), “Designing Red-Light-Activated Multifunctional Agents for the Photodynamic Therapy”, Angewandte Chemie International Edition, 51, 11420–11422.

[104] Santos E. R., Pina J., Venâncio T., Serpa C., Martinho J. M. G., Carlos R. M., (2016), “Photoinduced Energy and Electron-Transfer Reactions by Polypyridine Ruthenium(II) Complexes Containing a Derivatized Perylene Diimide”, Journal of Pysical Chemistry C, 120, 22831−2284.

[105] Wang J. G., Shang Y. L., (2013), “Synthesis and photophysical and electrochemical properties of three novel Ru(II) complexes”, Materials Research Innovations, 17, 58-61.

[106] Zhang P., Silva G. M., Deatherage C., Burd C., DiMaio D., (2018), “Cell-Penetrating Peptide Mediates Intracellular Membrane Passage of Human Papillomavirus L2 Protein to Trigger Retrograde Trafficking”, Cell, 174, 1465–1476.

BIOGRAPHY

Nuray Esra Aksakal was born on January 21th, 1987 in Kastamonu, Turkey. She was graduated from Gebze Anatolian High School, then she started her chemistry education at Middle East Technical University in Ankara. In 2011, she received her B.S degree. Same year she started master program in organic chemistry in METU, then she received her M.Sc degree in 2013. During her master education she studied in Tubitak and Roketsan research projects. In 2013, she started as a PhD student in Graduate School of Natural and Applied Sciences in Gebze Technical University. In 2015, she was accepted a research assistant in inorganic chemistry at GTU.

APPENDICES

Appendix A: Publications

Aksakal N. E., Chumakov Y., Yuksel F., (2019), “Crystal Structures of Two Perylenediimides: A Study of Bay-Substitution”, Journal of Chemical Crystallography, 49, 72-79.

Aksakal N. E., Ecik E. T., Kazan H. H., Ciftci G. Y., Yuksel F., (2019), “Novel ruthenium(II) and iridium(III) BODIPY dyes:insights into their application in photodynamic therapy in vitro”, Photochemical and Photobiological Sciences, **18**, 2012-2022.

Aksakal N. E., Kazan H. H., Ecik E. T., Yuksel F., (2018), “A novel photosensitizer based on a ruthenium(II) phenanthroline bis(perylenediimide) dyad: synthesis, generation of singlet oxygen and in vitro photodynamic therapy”, New Journal of Chemistry, 2018, 42, 17538-17545.